DC Plasma Spraying, Fundamentals

8

Abbreviations

APS	Atmospheric Plasma Spraying
CAPS	Controlled Atmosphere Plasma Spraying
CARS	Coherent Anti-Stokes Raman spectroscopy
CBL	Cold Boundary Layer
CFD	Computational Fluid Dynamics
CVD	Chemical Vapor Deposition
DC	Direct Current
D-Gun	Detonation Gun
eV	Electron Volt
HVOF	High-Velocity Oxygen Flame
i.d.	internal diameter
ISPC	International Symposium on Plasma Chemistry
ITSC	International Thermal Spray Conference
LDA	Laser Doppler Anemometry
LTE	Local Thermodynamic Equilibrium
NLTE	Non-equilibrium
NTSC	National Thermal Spray Conference
PSD	Particle Size Distribution
PTA	Plasma Transferred Arc
PVD	Physical Vapor Deposition
RF-ICP	Radio Frequency Inductively Coupled Plasma
slm	standard liter per minute
TS	Thermal Spray
TTPR	Triple Torch Plasma Reactor
ULPPS	Ultra-Low-Pressure Plasma Spraying
UTSC	United Thermal Spray Conference
VPS	Vacuum Plasma Spraying

8.1 Introduction

Materials have been developed for exceptional functional performance in specific applications, such as a number of specialty steels or super alloys. The increasing demand for combined functional requirements, such as high temperature resistance to corrosivec atmospheres in addition to abrasive wear resistance, and the ease of machining to the final form at a competitive cost, has led to the ever-increasing demand for coatings. According to [Fauchais et al. (2014)], the motivation for coating structural parts can be summarized by the following needs:

(a) improve functional performance by, for example, allowing higher-temperature exposure through the use of thermal-barrier coatings,
(b) improve component life by reducing wear due to abrasion, erosion, and corrosion,
(c) extend functional use by rebuilding the worn part to its original dimensions, thus avoiding the need for replacing the entire component, for example, a shaft or axle, and,
(d) reduce component cost by improving the functionality of a low-cost material with an expensive coating. In each of these uses of coating technologies, there should be no, or minimal, machining required of the coated part.

As discussed in Chap. 2, coating technologies can be roughly divided into deposition of thin films (thickness e <20 μm) and deposition of thick films (30 μm < e < several mm). Thin films offer excellent enhancement of surface properties. Physical Vapor Deposition (PVD) or Chemical Vapor Deposition (CVD) can provide surfaces with

M. I. Boulos et al. (ed.), *Thermal Spray Fundamentals*, https://doi.org/10.1007/978-3-030-70672-2_8

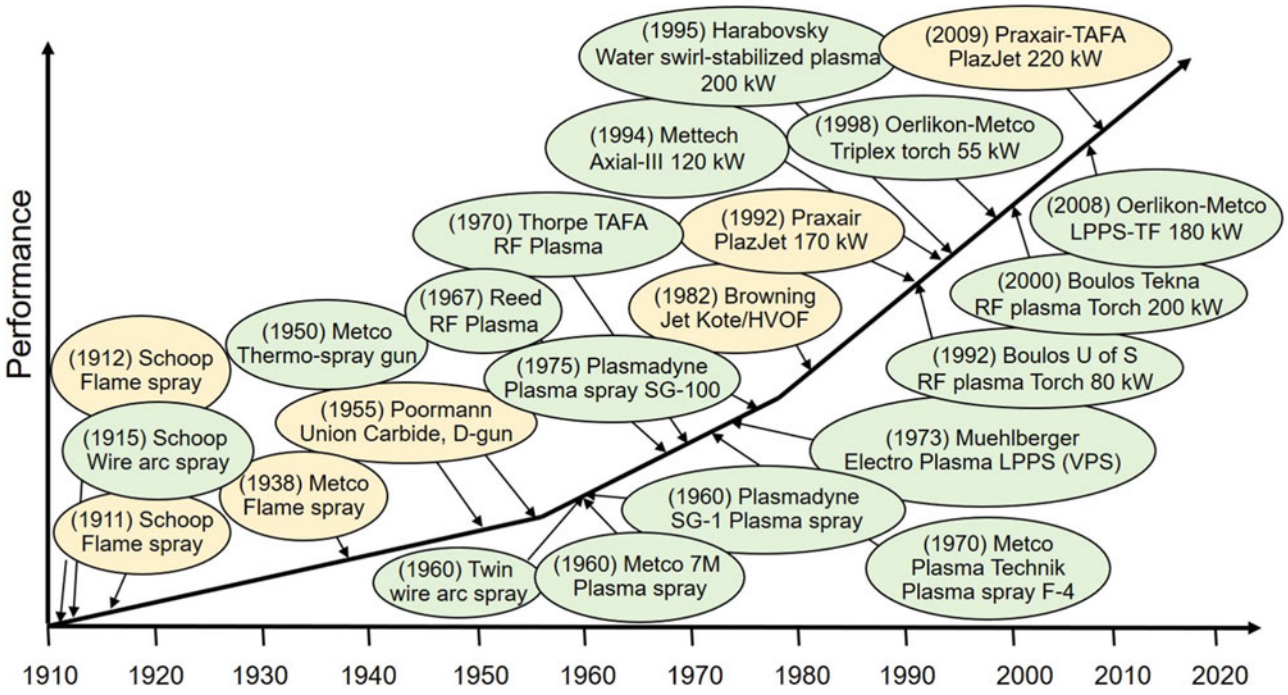

Fig. 8.1 Milestones in the development of the thermal spray industry, Yellow-combustion; Green-Plasma. [(Ang et al. (2013)]

unparalleled hardness or corrosion resistance. As most thin-film technologies require a reduced pressure environment, they are more expensive and impose a limit on the size and shape of the part to be coated. Thick films with e >30 μm are required when the functional performance depends on the layer thickness, for example, in thermal-barrier coatings, when strong erosion and corrosion conditions result in wear and the component life depends on the layer thickness, or when the original dimensions of the worn parts are being restored. Thick-film deposition methods include chemical/electro-chemical plating, brazing, weld overlays, and thermal spray. Each of these methods offers certain advantages and has certain limitations. In the following, only plasma spraying will be considered. It belongs to thermal-spray processes for which the definition is "Thermal spraying comprises a group of coating processes in which finely divided metallic or non-metallic materials are deposited in a molten or semi-molten condition to form a coating. The coating material may be in the form of powder, ceramic rod, wire or molten materials." Weld overlays could be included in this definition; however, from all the weld-coating processes, only Plasma Transferred Arc (PTA) deposition is usually included as a thermal-spray process. The coating material may be in the form of powders, ceramic rods, wires, or molten materials. In this chapter, only coatings resulting from powders will be discussed.

While thermal spray (TS) was developed in the beginning of the twentieth century, the technology was limited, for a long period, to essentially flame spraying. In the mid-1950s, the first plasma-spray torch was developed by Thermal Dynamics Corporation, followed by Metco and Plasmadyne, which developed the basis of the torch designs currently used in this field. Figure 8.1, based on data from [Ang et al. (2013)], illustrates the evolution of thermal-spray technology in terms of the turning points in plasma torch designs used in the thermal spray industry. In this figure, the yellow entries refer to combustion-based technologies, while the green ones refer to plasma-based technologies. Intense activities in this field over the past three to four decades has led to the development of a number of novel spray-coating devices/processes, such as the Water-stabilized plasma torch by [Hrabovsky (1997)], the RF Induction Coupled Plasma torch by [Boulos MI (1992)], the Axial III torch central powder injection DC plasma torch by [Northwest Mettech corp (1994)], and the triplex Torch and the Ultra Low-Pressure Plasma Spraying process (ULPPS) by [LPPS-TF, Oerlikon–Metco Cop. (2008)].

The driving force behind many of these developments has been the need to increase the temperature and gas velocity of the thermal-spray source beyond that offered by combustion-spraying technologies. They also aimed at better control on the chemical nature of the gases used, increased process

productivity, and improved economics. Compared to other thermal-spray technologies, the use of DC plasma sources has been central to such developments since they are at the high end of the temperature vs velocity diagram, as shown in Fig. 8.2.

The principal components of a DC plasma-spray system/process are illustrated in Fig. 8.3. Central to this system is the DC plasma torch generating a high-temperature, high-velocity plasma stream in which the coating material is injected in the form of either a fine powder using an appropriate carrier gas or a liquid as in the case of solution or suspension plasma spraying. The system also consists of an electrical, current-controlled, power supply, gas supply, powder, or liquid/suspension feeder and a closed-loop cooling water circuit. The auxiliary equipment necessary for the operation of the system include a manual or robotic torch controller, substrate support, environmental control of the ambient air, and general instrumentation and control systems.

This chapter deals essentially with the fundamentals of the DC plasma-spraying technology, highlighting the principal concepts of DC plasma torch design. This is followed by a discussion on gas and particle dynamics under plasma-spraying conditions including a brief review of mathematical models developed for the simulation of the plasma-spray process. In order to keep a balance between the size of the different chapters of this book and for ease of referencing, a review of the different DC plasma-spray processes is presented separately, in Chap. 9. These include Atmospheric Plasma Spraying (APS), Controlled Atmosphere Plasma Spraying (CAPS), Vacuum Plasma Spraying (VPS), and the relatively novel process of Ultra-Low-Pressure Plasma Spraying (ULPPS). A detailed discussion of powder/wire or cord preparation, substrate preparation, coating formation, and characterization are covered in Part III of this book, while process integration, industrial applications, and process economics are covered in Part IV.

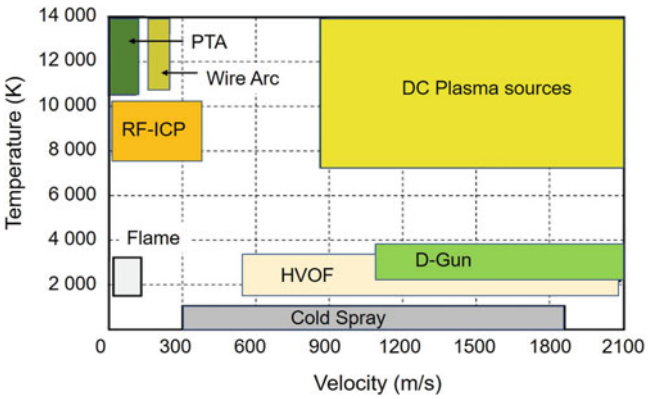

Fig. 8.2 Gas temperatures vs velocity mapping associated with different thermal-spray processes

8.2 Basic Concepts

Electric arcs generate high-temperature plasma through resistive energy dissipation when the current flows through the gas at sufficiently high temperatures to have an appreciable degree of ionization and high electrical conductivities. For most plasma-forming gases, the required temperatures at atmospheric pressure are above 8000 K [Boulos et al. (1994)]. By definition, in a thermal arc, the thermodynamic state of the plasma generally approaches Local Thermodynamic Equilibrium (LTE), which includes kinetic and chemical equilibrium, except for the arc fringes or close to a cooled wall. Such arcs, known as high-intensity arcs, typically require currents above 100 A and pressures in excess of 10 kPa. At lower pressures, electron and heavy particle temperatures are significantly different, as shown in Fig. 8.4. [Pfender (1978)].

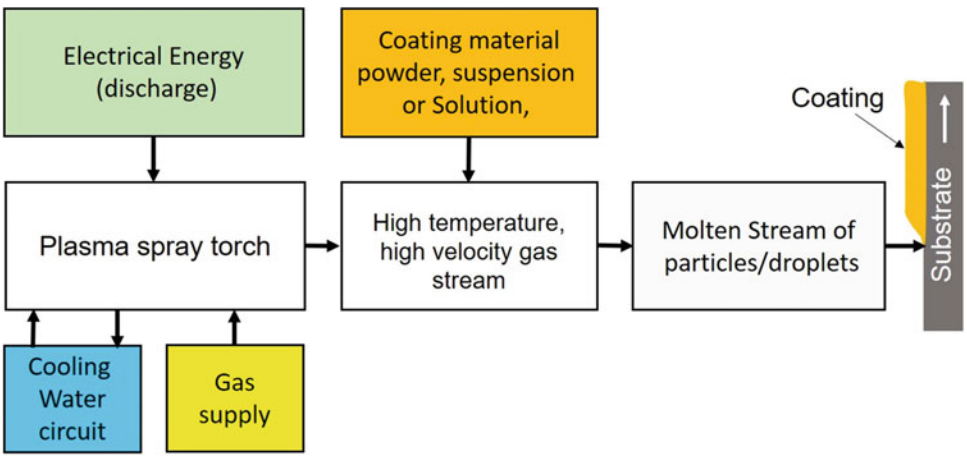

Fig. 8.3 Block diagram of a conventional DC plasma spray system

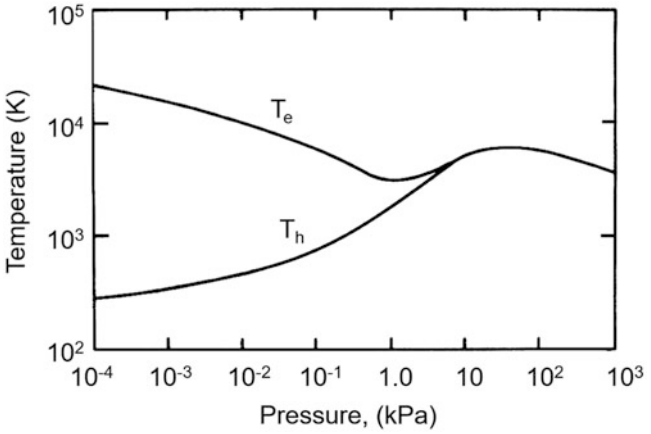

Fig. 8.4 Behavior of electron temperature (T_e) and heavy particles temperature (T_h) in an arc plasma. [(Pfender 1978)]

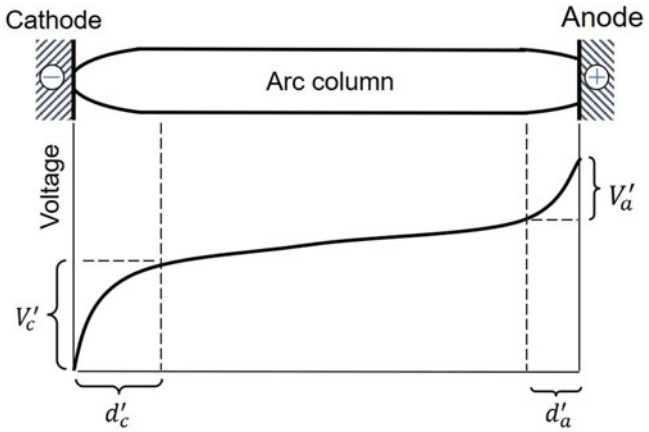

Fig. 8.5 Typical potential distributions along an arc

An electric arc struck between two electrodes is schematically represented in Fig. 8.5. There are three principal features that distinguish an arc from other discharge modes. For the sake of simplicity, the following discussion will be restricted to steady-state (DC) arcs

- ***Relatively high current densities***, in excess of 10^6 A/m^2. The situation is even more pronounced at the electrodes. Particular to the cathode, arcs may attach to the electrodes in the form of tiny spots in which current densities can be as high as 10^{10} A/m^2. The associated heat-flux densities are of the order of 10^9 to 10^{11} W/m^2, values requiring special precautions to protect the mechanical integrity of the electrodes.

- ***Low cathode fall***. As indicated in Fig. 8.5, the potential distribution in an electric arc changes rapidly in front of the electrodes, forming the so-called cathode and anode fall. The cathode fall is of particular interest; it assumes values of around 10 V in contrast to the typical cathode falls in glow discharges, which usually exceed 100 V. This relatively low cathode fall is a consequence of the more efficient electron-emission mechanisms at the cathode compared with those prevailing in glow discharges. It should be pointed out that the thicknesses d_c' and d_a' of the electrode regions in Fig. 8.5 are enlarged, particularly if high-pressure arcs are considered. Also, V_c' does not, in general, represent the true cathode fall. The actual cathode fall, V_c, corresponding to the electron space charge region may be several volts less than V_c'.

- ***High luminosity of the arc column***. This criterion provides a useful distinction between an arc and other discharge modes, provided the pressure is sufficiently high ($p \geq 1$ kPa).

An electric arc can be divided into three regions, the cathode region, the arc column, and the anode region.

8.2.1 Cathode

The cathode must supply electrons to the arc. In plasma torch designs used for plasma spraying, electrons are supplied through thermionic emission from a hot cathode material. The thermionic emission current can be described by the Richardson–Dushman equation relating the emission to the cathode temperature T_c and work function ϕ_w.

$$j = AT_c^2 \; exp\,(-e\,\phi_w / k\,T_c) \qquad (8.1)$$

Where, A is an empirical constant, which is about 6×10^5 A/m^2 K^2 for the majority of the cathode materials, e is the electronic charge, and k is the Boltzmann constant. The work function for most materials is around or above 4.0 eV; however, some oxides have work function values of between 2.5 and 3 eV. To obtain a current density of approximately 10^8 A/m^2, as required by the arc, the cathode temperature will have to be about 4500 K for a cathode material with a work function of 4.5 eV (e.g., for tungsten), but only about 2700 K for a material with a work function of 2.5 eV. Since tungsten has a very high melting point (4500 K) and, therefore structural stability, it is widely used as torch cathode. It is commonly used, however, alloyed with 1 or 2% by weight of a material with a lower work function. The consequence is a significantly reduced cathode operating temperature and longer cathode life. Examples of such materials are ThO_2, La_2O_3, or LaB_6. Cathodes based on tungsten cannot be used with oxidizing gases because the formation of volatile tungsten oxides, at temperatures already below 2000 K, will result in rapid cathode erosion. For operation with oxidizing gases, button-type electrodes are used where the thermionic emission material is inserted in the form of a button into a water-cooled copper holder. The button typically consists of

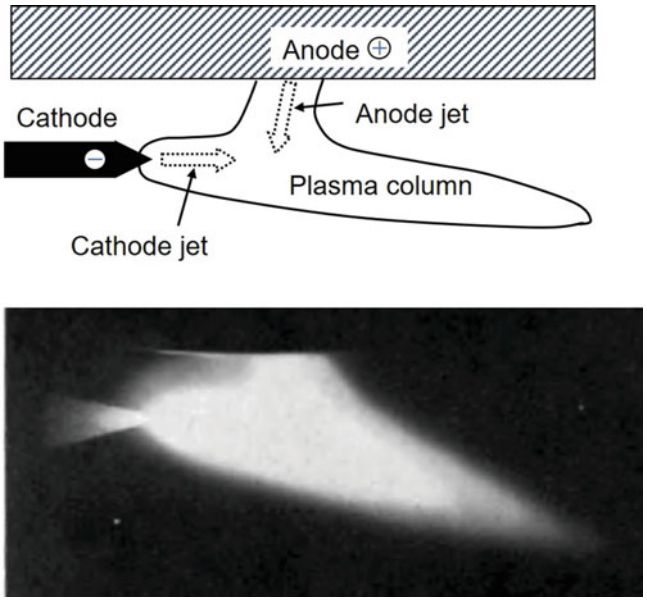

Fig. 8.6 Interaction of cathode and anode plasma jets. [Pfender (1978)]

hafnium or zirconium, and the surface of the material is molten. However, the pressure exerted by the arc due to the ion flux to the cathode and due to the magnetic forces resulting from the self-magnetic field and the change in current density in front of the cathode will keep the molten material in place [Peters et al. (2005)].

The self-magnetic field generates a higher pressure inside the arc than the pressure surrounding the arc, and this pressure differential is proportional to the arc current density. The arc is usually constricted in front of the cathode because of the heat loss from the plasma to the solid material. As a consequence, the pressure close to the cathode is higher than it is farther downstream, resulting in a flow away from the cathode, the cathode jet [Maecker (1955)], as illustrated in Fig. 8.6. The superposition of the cathode jet to the axial gas flow used in a plasma-spray torch results in the increased convective cooling of the arc in the vicinity of the cathode, leading to even stronger constriction. The resulting flow velocities can reach several 100 m/s. The highest temperatures in the arc are observed in front of the cathode, reaching values between 20,000 and 30,000 K depending on the current density and the fluid dynamics of the flow in the cathode region.

8.2.2 Arc Column

The arc column characteristics are determined by the energy dissipation per unit length, that is, by the arc current, the plasma gas flow and composition, and the arc channel diameter. The arc column can be described by the conservation equations for mass, momentum, and energy. In principle, Joule heat dissipation, expressed by the product of current density and electrical field strength, is balanced by the heat addition to the plasma gas and the heat losses to the surroundings. If the heat losses to the surroundings increase, the power dissipation has to increase. Since the plasma torches operate with a constant current, higher electric-field strengths and arc voltages will compensate for the increased heat loss. Increased heat losses are the result of:

- reduced nozzle diameter,
- higher total plasma gas flow rates, and,
- increased thermal conductivities and specific heats of the plasma gases.

As shown in Chap. 3, the thermal conductivities and specific heats increase from argon to nitrogen and helium (depending on the temperature range) to hydrogen. Accordingly, the column-field strengths and arc voltages are increasing from argon arcs to helium and nitrogen arcs to hydrogen arcs, with pure hydrogen arcs typically having four times the arc voltage of an argon arc for similar conditions. However, it must once again be emphasized that to operate the hydrogen arc in a plasma torch, significantly higher volumetric flow rates will be required, with considerably higher voltages as the result. The arc diameter will decrease with increasing energy loss rates.

The species present in the arc column are molecules, atoms, ions, and electrons, and for gas mixtures, there will be multiple types of atoms and ions. The strong radial temperature and density gradients result in strong diffusion fluxes, and the diffusion coefficients are quite different for the different species. The consequence is a "demixing" effect where lighter species have higher concentrations in the arc fringes than predicted according to an equilibrium temperature [Murphy (1996) and Snyder et al. (1995)]. These effects must be taken into account in particular when heat transfer rates are estimated from plasmas consisting of gas mixtures. The result is that heat transfer rates in the fringes of the arc or arc jet can be higher than expected if diffusion is not taken into account. While electrons would diffuse at very high rates, their diffusion rate is limited by the electric fields generated when electron densities are different from ion densities. Therefore, electrons diffuse only in conjunction with an ion with the ambipolar diffusion rate, which is approximately twice the ion diffusion rate [Fincke et al. (1993a, b)]. Furthermore, any mixture containing helium is unlikely to contain any helium ions because of the high ionization energy of helium compared to all other gases. The consequence is that there is no ambipolar diffusion of He ions and lower He concentrations are found in the arc fringes [Fincke et al. (1993a, b)].

While immense progress has been made with the modeling of the arc column in plasma torches [Mariaux et al. (2001), Baudry et al. (2005), Dussoubs (1998), Trelles

et al. (2006), Trelles (2007)], it still requires significant effort and computational time to use CFD codes as a design tool. However, an integral energy balance (integrated over the radial coordinate) can provide some information on the arc-heating process inside the torch with information, which can be easily obtained:

$$\dot{m}\,\frac{\Delta\overline{h}}{\Delta z} + Q_{cond} + Q_{rad} = I \times E \tag{8.2}$$

with $\dot{m}$ being the mass flow rate of the plasma gas, $\Delta\overline{h}$ the increase in enthalpy averaged over the cross-section per unit length Δz, and Q_{cond} and Q_{rad} the losses to the torch wall by heat conduction and radiation, and $I \times E$ the electric energy dissipated per unit length of the arc. Further integration over the entire arc length will give the energy balance for the torch

$$\dot{m}\,h_{ave} = \eta P_{el} = P_{el} - Q_{loss} \tag{8.3}$$

with h_{ave} the average enthalpy of the gas leaving the torch, η the torch gas heating efficiency, P_{el} the electric power input into the torch (current × voltage), and Q_{loss} the heat lost to the torch cooling water. The torch average enthalpy is defined as

$$h_{av} = 2\pi\,\frac{\int_o^R \rho v h r\,dr}{\dot{m}} \tag{8.4}$$

with ρ, v, and h the plasma mass density, velocity, and enthalpy at a given radial location at the torch exit, and R the channel radius. Sometimes the term "average temperature" is used, related to the average enthalpy

$$h_{av} = \int_{T_{ref}}^{T_{ave}} c_p\,dT \tag{8.5}$$

with T_{ref} the reference temperature for a zero value of the enthalpy and c_{p} the specific heat at constant pressure of the plasma gas. The average velocity is defined accordingly

$$v_{ave} = \frac{\dot{m}}{\rho(T_{ave})\,A} \tag{8.6}$$

with $\rho(T_{ave})$ the mass density of the plasma gas at the average temperature, and A the channel cross-sectional area. A torch energy balance easily allows determination of the average values of temperature and velocity, but one needs to keep in mind that the peak values for temperature and velocity can easily be twice the average value.

8.2.3 Anode

The anode usually consists of a water-cooled copper channel, sometimes lined with a tungsten or tungsten–copper sleeve, and numerous designs exist for tailoring the fluid dynamics within this channel. Nozzle designs can emphasize high gas velocities, high gas temperatures, narrower or wider temperature profiles, and different average arc lengths and consequently arc voltages and torch powers. Typical nozzle diameters are between 6 and 10 mm for arc currents between 300 and 1000 A. The effect of the diameter on the plasma temperature depends on the operating conditions, but in general, a temperature increase is noticed for smaller channel diameters, because the increased electric field strength resulting from the increased heat loss leads to increased local heating of the plasma gas. Because of the nonlinearly varying dependence of the enthalpy on the temperature (e.g., a strong increase with temperature in the ionization region 12,000–15,000 K), a strong increase in power dissipation will increase the enthalpy but only change the temperature by 1000–2000 K. The effect of the nozzle diameter on the plasma velocity is stronger, because the flow velocity is inversely proportional to the channel cross-section area, in addition to showing increases due to higher temperatures and lower plasma densities.

It should be noted, however, that the anode is a passive component, just collecting electrons to allow the current to flow from the solid conductors of the electrical circuit to the plasma. The difficulty is that a cold gas boundary layer exists between the plasma and the anode and that nonequilibrium conditions exist in this boundary layer, that is, higher electron temperatures than heavy particle temperatures, necessary for the current to flow across this boundary layer [Paik et al. (1993), Trelles et al. (2007a, b, c), Dimulescu et al. (1980) and Leveroni et al. (1987)]. The current flow is additionally strongly dependent on the electron-density gradients and can be expressed by [Dimulescu et al. (1980)].

$$j = \sigma\,E_x - \frac{\sigma}{e n_e}\,\frac{dp_e}{dx} \tag{8.7}$$

where j is the electron current density, σ the electrical conductivity, E_x the electric field normal to the anode surface, e the electronic charge, and n_{e} and p_{e} the electron number density and partial pressure, respectively. The strong partial pressure gradient in front of the cooled anode surface results in strong electron diffusion fluxes toward the surface, constituting the major component of the current flow.

The heat flux to the anode is strongly tied to the current flow [Pfender (1994), Jenista et al. (1997a, b)]:

$$q = j\phi_w + \left(\frac{5k}{2e}\right) j T_e - \kappa_h\,\frac{dT_h}{dx} - \kappa_e\,\frac{dT_e}{dx} + j_i(\varepsilon_i - \phi_w) \tag{8.8}$$

with ϕ_{w} the work function of the anode material, k the Boltzmann constant, κ_h and κ_e the heavy particle and electron

thermal conductivities, respectively, T_e and T_h the electron and heavy particle temperatures, respectively, j_i the ion current toward the anode, ε_i the ionization energy of the plasma gas atoms. The first term on the right-hand side is associated with energy release when the electrons carrying the current to the anode are incorporated into the crystal lattice (condensation energy); the second term is the thermal energy transported by the electrons; the third and fourth terms are the heavy particle and electron conduction terms, respectively; and the fifth term represents the energy released when an ion recombines with an electron at the anode surface. The first three terms are usually the dominant ones [Jenista et al. (1997a, b)].

The attachment of the arc at the anode surface may occur diffusely, as well as severely constricted (spot), and it is still not entirely clear under which conditions constriction will occur. Chemical reactions on the anode surface as, for example, encountered in arcs operated in atmospheric air or in other oxidizing fluids seem to favor a constricted anode root which, at the same time, may move more or less randomly over the anode surface with appreciable velocities. Anode evaporation is another mechanism, which leads, in general, to spot formation. In high-current arcs with relatively small electrode separation (a few centimeters), the diffuse anode attachment is directly associated with the cathode jet. The well-known bell shape of a free-burning high-intensity arc is a typical example. The intense cathode jet impinging on the anode surface pushes hot plasma against the anode, eliminating the need for ionization in the anode fall zone. By increasing the electrode gap under otherwise identical conditions, the influence of the cathode jet at the anode is diminished and, finally, at sufficiently large gaps, the arc forms a single or several spots at the anode surface. Further evidence that anode spot formation and cathode jet are intimately related is illustrated in Fig. 8.6., in which the axis of the cathode is parallel to the surface of a plane anode so that the cathode jet does not impinge on the anode. The deflected cathode jet provides evidence that there must be an appreciable constriction of the anode attachment. Any constriction of the current path leads to the previously described pumping action, which results in this case in an anode jet that causes the observed deflection of the cathode jet from the anode surface. The relative strength of the two jets determines the angle of deflection.

While most commercial plasma torches use anodes with cylindrical nozzle bores, anodes with Laval-type diverging nozzles exits have been used. This type of nozzle provides a somewhat more uniform velocity and temperature distribution at the nozzle exit and somewhat reduced turbulent cold gas entrainment, resulting in more uniform particle heating and acceleration [Roumilhac et al. (1990a, b), Rahman et al. (1998)].

8.2.4 Arc Stability

Arc stability has to be of central concern in plasma torch design. The arc plasma is easily influenced by asymmetric cooling or by effects of magnetic fields that can lead to arc extinction. The principal counter-acting effect promoting arc stability is an increase in heat loss due to steeper temperature gradients. However, arc voltage and power dissipation will increase. Steenbeck's minimum principle states that the arc will adjust its position such that the overall voltage drop will be minimum. That means the preferred arc position is that where the energy loss is minimized [Pfender (1978)]. An excellent review on the subject of electric arc fluctuations in DC plasma spray torches is given by [Rat et al. (2017)].

Arcs can be stabilized by a cylindrical wall (e.g., water-cooled metal tube surrounding the arc) forcing the arc to remain on the axis of the cylinder (wall stabilization), or it can be stabilized by a superimposed axial flow of a cold sheath gas, again increasing cooling when the arc moves off the axis (gas stabilization). Flow stabilization is particularly effective when a swirl (or vortex) flow is used because the vortex creates a low-pressure zone on the axis of the flow in which the low-density, high-temperature arc gases are confined, while the heavier cold gases are flowing along the external regions of the vortex. In plasma torches, one usually has a combination of wall and flow stabilization. The preferred position of the arc would be the one where the cathode-anode distance is the smallest. However, at this location, the cold gas velocity is usually the highest, resulting in strong cooling of the arc and higher arc voltages. Consequently, the arc attachment is usually found where the fluid dynamic condition brings the plasma close to the anode surface, either through recirculation eddies or through heating of the boundary layer flow [Sun and Heberlein (2005), Yang and Heberlein (2007)].

In plasma spraying, the most important instability is the anode attachment instability. As illustrated in Fig. 8.7, the arc root struck between the column and the anode surface is exposed to several forces, the dominant being the drag force, F_D, exerted by the cold gas flow in the boundary layer over the anode surface, and the electromagnetic force, F_m, which is a Lorentz force due to the self-induced magnetic field [Rat et al. (2017)]. Because of the stiffness of the arc root the cold boundary layer flow will go around, it is exerting a drag force on the arc root in the downstream direction. As a consequence, the arc root attachment is pushed downstream until the voltage between the column and the anode surface becomes sufficiently high for a local breakdown to occur at an upstream location (restrike) [Wutzke et al. (1968)]. Fig. 8.8 shows a schematic representation of a restriking arc and the associated voltage oscilloscope trace, indicating strong voltage oscillations giving rise

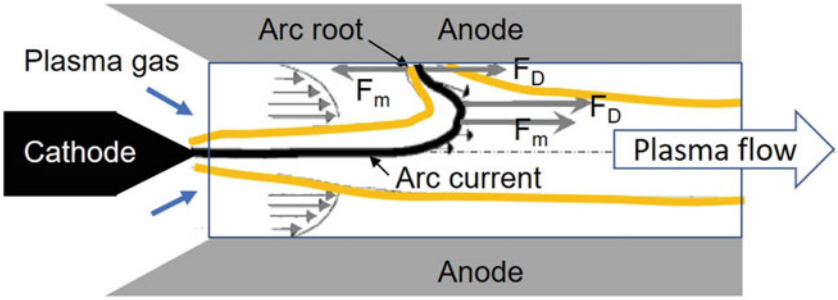

Fig. 8.7 Schematic representation of the main forces acting on the arc column and its root attachment. [Rat et al. (2017)]

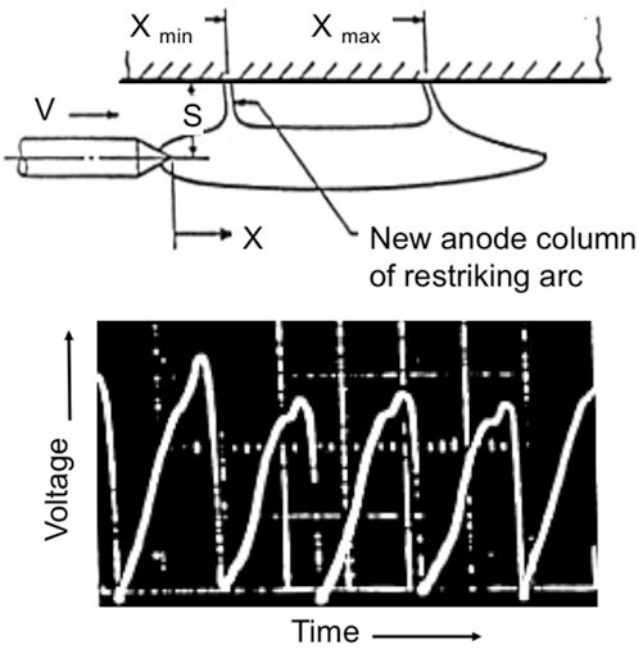

Fig. 8.8 Illustration of the restrike mode of operation of a plasma torch with an upstream connection forming between the arc column and the anode nozzle. The oscilloscope image shows the associated voltage trace. (Courtesy of Emil Pfender and Steven Wutzke)

to important fluctuations of the arc power. The effect of such fluctuations on particle heating and acceleration will be discussed later. Recent flow visualization experiments with a similar set-up of an anode with cold gas flow between the arc and parallel to the anode surface have demonstrated that the location of the restrike is determined by fluid dynamic instabilities.

[Paik et al. (1993)] demonstrated that the Steenbeck minimum principle is a useful criterion for predicting the position of the anode arc root in a plasma torch. Therefore, this criterion should provide useful guidelines for the design of plasma torches. Although their analysis is based on a two-dimensional model, the results are in qualitative agreement with experimental findings, which show that:

- the axial distance from the cathode tip to the stable arc-root position, x, increases with increase in the gas flow rate due to the stronger gas dynamic drag force,
- the axial distance x, decreases with increase in the arc current, due to the stronger magnetic body force,
- the arc attachment on the anode surface is closer to the cathode tip with reduction in the diameter of the arc channel,
- a more constricted anode root attachment is observed with hydrogen plasma compared to argon plasma.

The movement of the point of anode attachment, as indicated by the arc voltage fluctuations given in Fig. 8.9, reveals three different modes of operation [Coudert et al. (1994), Coudert et al. (1995), Planche et al. (1997), Duan et al. (1999a), Dorier et al. (2001), Duan et al. (2000, 2002)].

- the "*steady*" mode corresponding to a fixed location of the arc root attachment on the anode with very low fluctuations of the voltage trace,
- the "*take-over*" mode with the arc root moving back and forth along the main flow direction and with a sinusoidal wave form of the arc voltage,
- the "*restrike*" mode where the arc attachment moves downstream inside the anode nozzle until an upstream restrike occurs with a new connection closer to the cathode between the arc column and the anode nozzle. The arc voltage has a saw-tooth-shaped form.

The *restrike* mode is mostly observed when using molecular plasma forming gases. It was observed in both upstream and downstream restrike configurations with high-voltage amplitude fluctuations, which can reach values of 30 to 70% of the average arc voltage, and frequency typically between 2 and 6 kHz [Duan and Heberlein (2002)]. The *take-over*mode is mostly observed with pure noble gases such as Ar and He; the magnitude of the fluctuations is directly connected with the arc current and usually of the order of 20 to 50% of the mean arc voltage. It has a much wider Fourier spectrum of the fluctuation frequencies. For the *steady*mode, only minimal fluctuations are observed at low

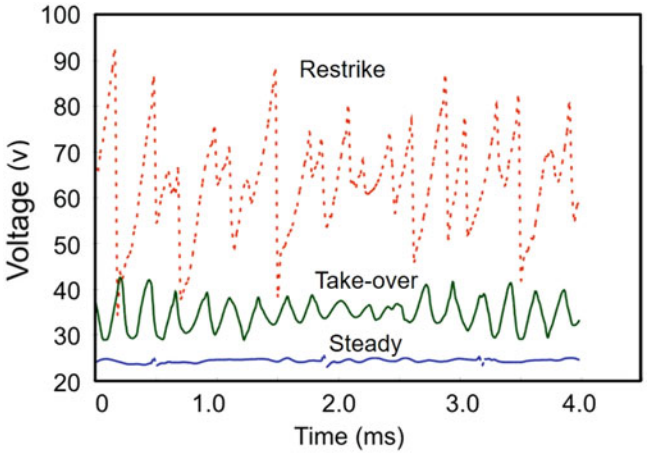

Fig. 8.9 Typical voltage traces for DC plasma torch operating in restrike mode (100 A, 12 slm Ar +40 slm He), take-over mode (500 A, 40 slm Ar + 20 slm He), and steady mode (900 A, 60 slm Ar). [Duan and Heberlein (2002)]. (Reprinted with permission of ASM International. All rights reserved)

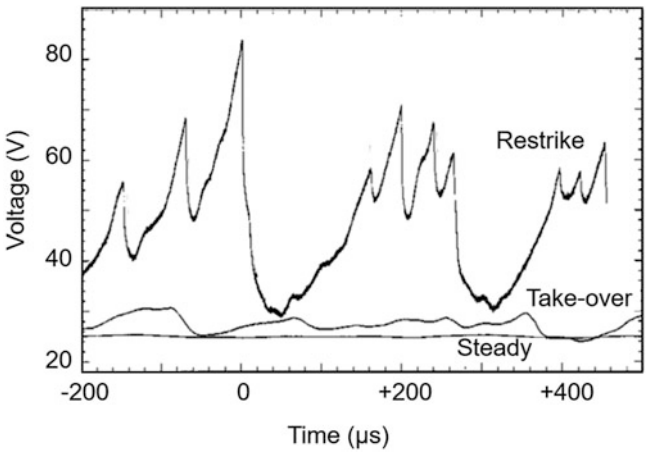

Fig. 8.10 Typical voltage traces for an F4 plasma torch, in the restrike, take-over, and steady modes of operation obtained with warn electrodes, and a straight gas injector. (**a**) restrike mode, 500 A, 40 slm Ar + 4 slm H_2, (**b**) take-over mode 500 A, 40 slm Ar, (**c**) steady mode, 600 A, 30 slm Ar. [Dorier et al. (2001)]

frequencies, and these fluctuations are not associated with the fluid dynamic behavior of the arc.

A study of the performance of the F4 torch by Oerlikon-Metco was reported by [Dorier et al. (2001)]. Typical voltage traces under different operating conditions are given in Fig. 8.10. These were obtained using worn electrodes with a straight gas injector. The "*restrike*" mode trace was obtained for a current of 500A, and gas composition of (40 slm Ar + 4 slm H_2) show high voltage fluctuations formed of large voltage drops with smaller irregular voltage drops in between. For the "*take-over*" mode, obtained with a current of 500 A and plasma gas of pure argon (40 slm Ar), the voltage signal exhibits smooth fluctuations of weak amplitude (less than 10 V). Operating at high current with a reduced gas flow of pure argon (600 A, and 30 slm Ar), the take-over mode switches to the so called "*steady*" mode for which the voltage is nearly constant. The typical power spectra of the voltage fluctuations in the r*estrike* and *take-over* modes are given in Fig. 8.11. These were obtained with new electrodes and Ar/H_2 plasma gas with a swirl injector. The spectra given in Fig. 8.11a were in the *take-over*mode with currents of 200 and 600 A. These show that the fluctuations of the arc voltage are reduced especially at high currents. The corresponding power spectrum for operation in the *restrike*mode, with an arc current of 400 A and plasma gas of (40 slm Ar + 4 slm H_2), is given in Fig. 8.11b. This spectrum is characterized by a strong peak at 3.6 kHz, corresponding to the frequency of the major restrikes.

According to [Dorier et al. (2000)], the gas injection mode (straight or vortex) can also modify the shape of the restrike signal, as shown in Fig. 8.12a, for N_2-H_2 plasma [Dorier et al. (2000)]. The corresponding power spectrum, given in

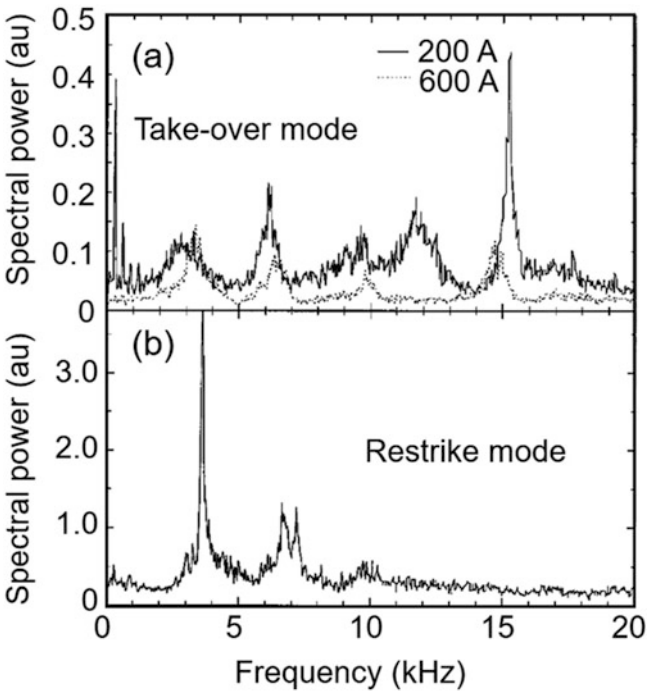

Fig. 8.11 Power spectra of the voltage fluctuations for an F4 plasma torch using new electrodes and a swirl gas injector (**a**) take-over mode with arc currents of 200 and 600 A, 40 slm Ar, (**b**) restrike mode with arc current of 400 A, plasma gas (40 slm Ar +4 slm H_2). [Dorier et al. (2001)]

Fig. 8.12b, shows significant differences for these two types of injection modes of the plasma forming gas.

By assigning a "mode value" of "zero" to the *steady* mode, of "one" to the *take-over* mode, and of "two" to the *restrike* mode, and using an algorithm based on the ratio of

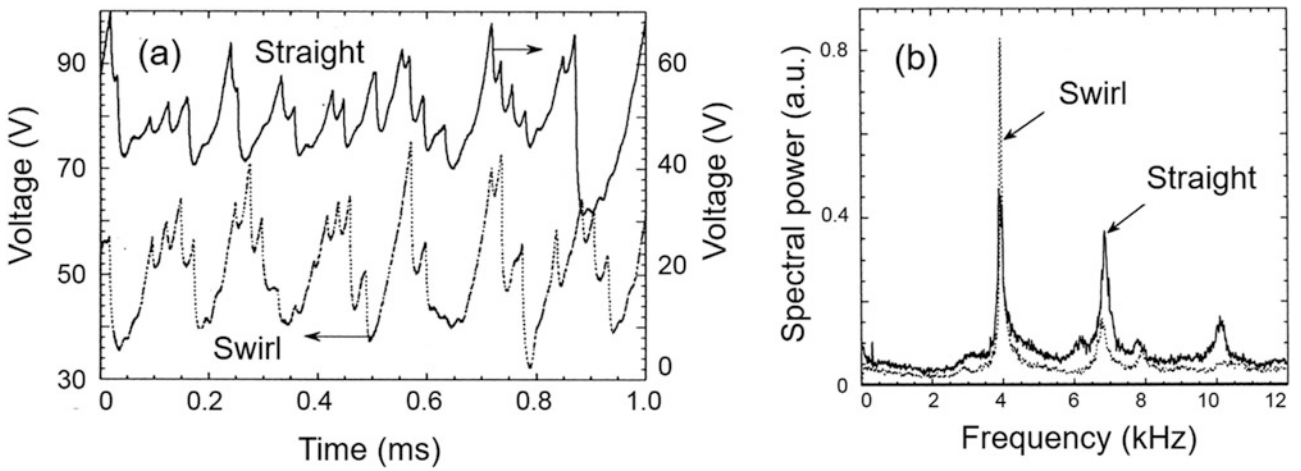

Fig. 8.12 (**a**) typical voltage traces and (**b**) corresponding power spectra for an F4 torch operating with N_2-H_2 mixture with vortex and straight injection of the plasma forming gas. [Dorier et al. (2000)]

the rate of voltage increase vs. the rate of voltage decrease, and of the absolute value of the voltage fluctuation, any arc appearance between the extremes can be quantified by assigning a specific mode value between zero and two to the voltage trace [Duan and Heberlein (2000)]. The mode value for distinguishing the *restrike* mode from the *take-over* mode is characterized by the shape factor "S," defined as:

$$S = Time\ of\ voltage\ increase / Time\ of\ voltage\ decrease,$$

while the mode value for distinguishing the *take-over* mode from the *steady* mode is based on the amplitude factor "A" of the voltage trace:

$$A = (\Delta V/V)\ 100\%$$

A ≥ 10% and S 5	the arc is in a *restrike* mode with a mode value of 2
A ≥ 10% and S < 1.1	the arc is in a *take-over* mode with a mode value of 1
A ≥ 10% and S < 5	the arc is in a *restrike – take-over* mixed mode, and the mode value is determined as [1 + (S-1.1)/3.9]
A < 2%,	the arc is in a *steady* mode with a mode value of 0
2% < A < 10%,	the arc is in a *take-over – steady* mixed mode with a mode value of [(A – 2%)/8%]

The physical significance of this mode value can be explained by the end-on picture of the arc inside the nozzle shown in Fig. 8.13a, together with an intensity scan giving the arc cross-section and the thickness of the boundary layer between the arc and the anode nozzle wall. Most of the data given in Fig. 8.13b show a clear correlation between the mode value and the thickness of the boundary layer. A thicker boundary layer generated by higher gas flow rates, higher hydrogen or helium concentrations in the plasma gas, or lower currents, results in a more *restrike*-like mode. In

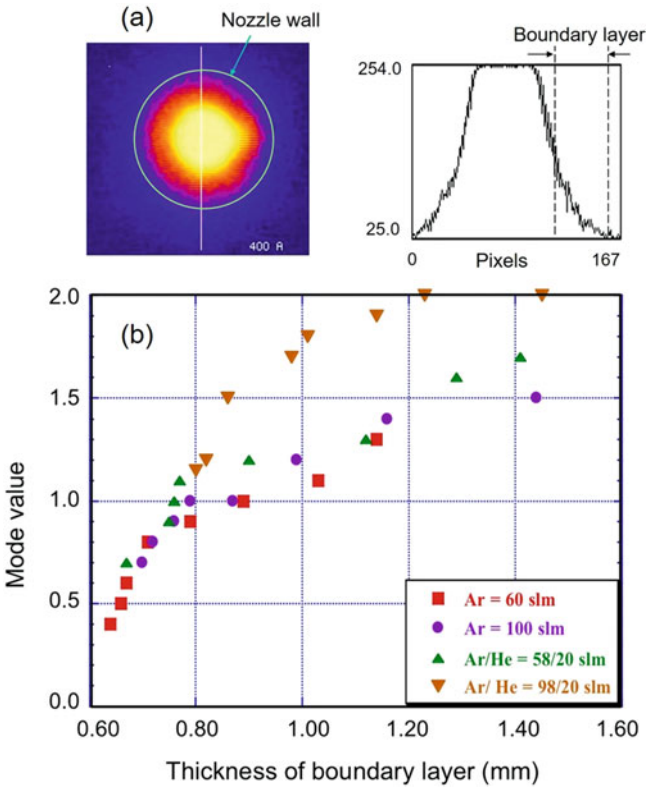

Fig. 8.13 (**a**) End-on image of the arc inside the anode nozzle and the associated intensity scan used for boundary layer thickness measurements. (**b**) The relation between torch operating mode value and boundary layer thickness. [Duan and Heberlein (2002)]. (Copyright © ASM International. Reprinted with permission)

general, a *restrike* mode does not occur with a pure argon arc, but addition of hydrogen or nitrogen beyond a certain amount will constrict the arc and increase the boundary layer thickness, favoring a *restrike-like* behavior. A study of the effect of operating parameters on the boundary layer thickness and the voltage fluctuations for different nozzle designs show that the arc current has the strongest effect on reducing the boundary layer thickness and the arc root fluctuations, but that the effect of increasing the total mass flow rate and the concentration of the secondary gas such as hydrogen can be different for different nozzle designs, and will depend on the nature of the primary gas, being argon or nitrogen [Nogues et al. (2007)]. For plasma spraying, well controlled arc motion to distribute the heat input to the anode surface is necessary to reduce anode erosion and extend its life. The preferred mode should not give rise to excessive variations of the arc voltage as experienced in the *restrik*e mode since it would result in significant fluctuations of the arc power, that is, a mode close to the *take-ove*r mode value of "one."

Table 8.1 Plasma torch operating conditions

Parameter	Setting
Arc current	200 to 900 (A)
Primary gas	40 to 120 slm (Ar)
Secondary gas	0 to 40 slm (He)
Gas flow	20% vortex +80% straight
Anode internal diameter	8 and 10 (mm)
Anode condition	New, used, burnt

According to [Duan and Heberlein (2002)], the control over coating quality in plasma spraying is partly dependent on the arc and jet instabilities of the plasma torch. Different forms of instabilities have been observed with different effects on the coating quality. Authors report on an investigation of these instabilities based on high-speed end-on observations of the arc. The framing rate of 40,500 frames per second has allowed for the visualization of the anode attachment movement and the determination of the thickness of the cold-gas boundary layer surrounding the arc. The images have been synchronized with voltage traces. The arc instabilities can be seen to enhance the plasma jet instabilities and the cold-gas entrainment. These results are particularly useful for guiding plasma torch design and operation in minimizing the influence of plasma jet instabilities on coating properties. The investigation has been carried out with a Praxair SG-100 plasma-spray torch operating in the subsonic mode. A #2083–129 cathode and a #2083–720 anode have been used. The anode has a straight bore nozzle with an 8 mm diameter and 25 mm in length. The torch is operated with argon as the primary gas and helium as the secondary gas. The operating parameters include arc current, mass flow rate of the plasma gases, gas injection method, and anode condition. The spray parameters are summarized in Table 8.1.

Figure 8.14 [Duan and Heberlein (2002)] shows the mode value distribution for different currents and mass flow rates of

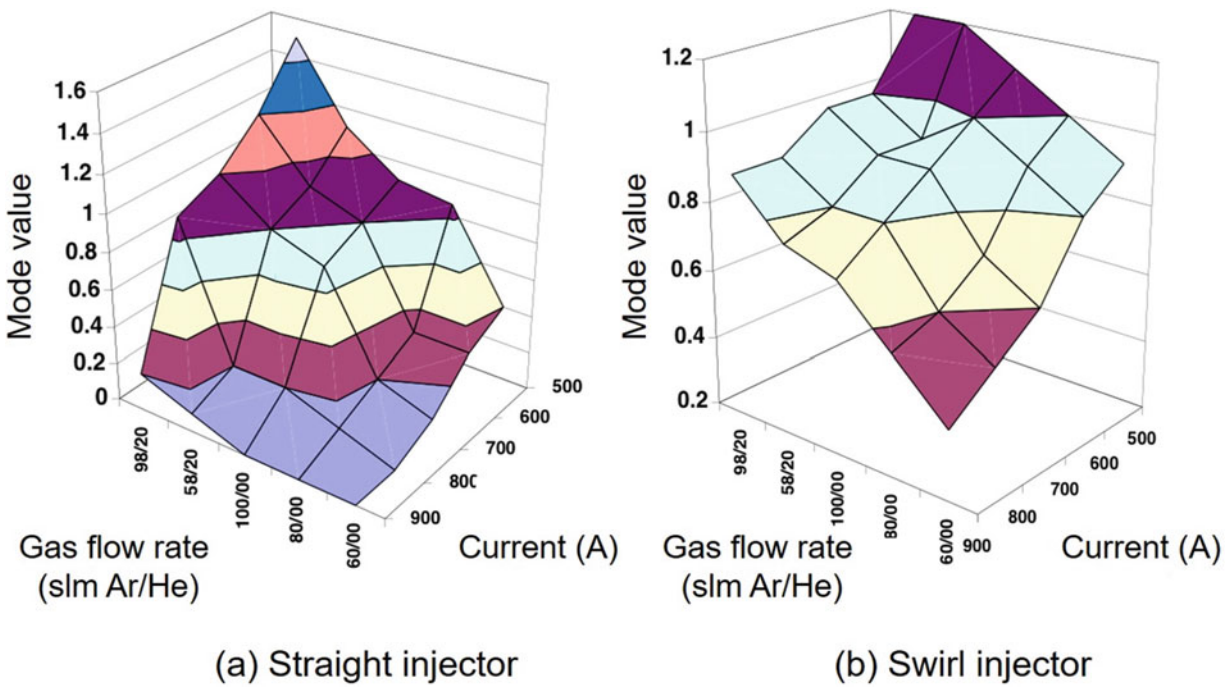

Fig. 8.14 Mode value contours for different arc currents and plasma gas flow rates for a Praxair SG 100 torch with (**a**) straight injection and (**b**) swirl injection (right). [Duan and Heberlein (2002)]. (Copyright © ASM International. Reprinted with permission)

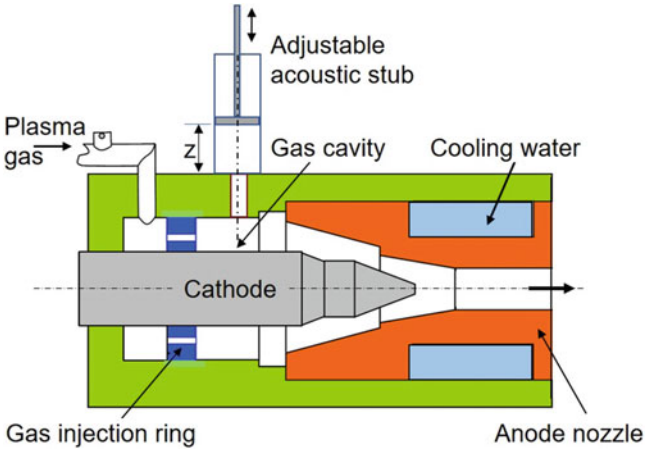

Fig. 8.15 Schematic of (**a**) the PT F4 torch with the cathode cavity volume V, (**b**) the acoustic stub fixed on the pressure probe position and acting as resonator on the cathode cavity [Rat and Coudert (2011)]. (Copyright © ASM International. Reprinted with permission)

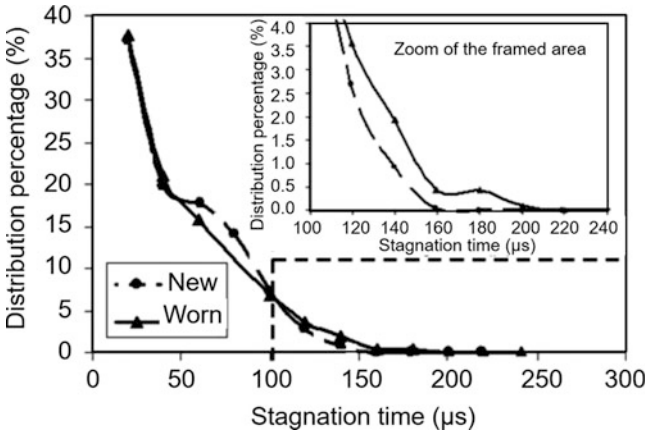

Fig. 8.17 Fraction of occurrences that an arc has a specified residence time at a given location, for "New" and "Worn" anode. The inset shows an increase in residence time above 120 μs for the used anode, indicating accelerating erosion. [Fauchais (2004)]. (Copyright IOP Publishing. Reproduced with permission. All rights reserved)

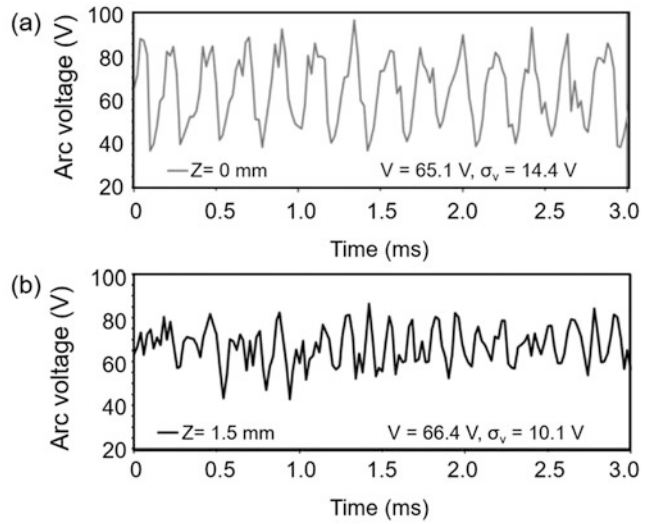

Fig. 8.16 Arc voltage fluctuations for different piston positions of the acoustic stub, Ar-H_2 (45–10 slpm), 500 A. (**a**) z = 0 mm, (**b**) z = 1.5 mm [Rat and Coudert (2011)]. (Copyright © ASM International. Reprinted with permission)

a Praxair SG-100 plasma torch (see Sect. 8.2.3.1 for torch description) for two different plasma gas injection methods, straight injection and tangential (swirl) injection. It is clear that the distributions for both injection methods have a plateau with a mode value between 0.8 and 1 (*take-over* mode), which indicates a stable mode of operation where small variations in the operating parameters do not change the mode value very much. Lower currents, higher mass flow rates, and higher concentrations of the auxiliary gas such as helium in the plasma gas lead to higher mode values, that is, a more *restrike-like* behavior.

[Coudert et al. (2007) and Rat et al. (2008)] studied the arc voltage fluctuations for a commercial plasma torch, Sulzer Metco F4, with a 6 mm i.d. anode-nozzle, arc current of 600 A, working with Ar-H_2 mixtures as plasma gas (45 slm (Ar) + different flow rates of H_2). Power spectra of the arc voltage fluctuations revield main fluctuation frequencies between 4 and 5 kHz, with a secondary peak observed at 7.5 kHz for low hydrogen flow rates. Attributing the mean arc spot lifetime exclusively to the Cold Boundary Layer (CBL) is not fully justified since the fluctuation frequency increases as the hydrogen flow rate increases. Moreover, according to the voltage signal, the duration of arc restrikes is about 30–100 μs, that is, frequencies higher than 10 kHz and the evolution of the main fluctuation frequency (4–5 kHz) cannot be described in terms of CBL thickness. [Coudert and Rat (2008) and Rat and Coudert (2011)] showed that the restrike mode is superimposed on the main fluctuation of arc voltage, observed around 4–5 kHz. This main oscillation is mainly due to the compressibility effects of the plasma-forming gas in the rear part of the plasma torch, that is, in the cathode cavity represented in Fig. 8.11 [Coudert et al. 2007; Coudert and Rat 2008)].

The plasma torch behaves like a Helmholtz resonator where pressure inside the cathode cavity is coupled with the arc voltage. The authors showed that pressure inside this cavity is correlated with the arc voltage. They have correlated the intermittent behavior of the torch, and the oscillation modes exchange energy. They also showed that the Helmholtz mode can be damped by the use of an acoustic stub (see Fig. 8.15b) mounted on the plasma torch body at the pressure probe position (see Fig. 8.15a). By adjusting the position, z, of the piston (see Fig. 8.15b), the amplitude of the voltage fluctuations can be reduced. This is illustrated in Fig. 8.16 showing the change of the time dependence of the

arc voltage with a varying z, generated with an Ar-H_2 (45–10 slm), a 500 A arc, and a nozzle with an inner channel diameter of 6 mm. In this figure, arc voltages are raw signals and contain all contributions (modes) described previously. The position z = 0 mm corresponds to the situation (Fig. 8.16a) where the acoustic stub is inactive and z = 1.5 ± 0.5 mm to the most effective position to damp the Helmholtz mode. Of course, such studies are preliminary ones and additional work is still necessary.

The electrical stability of the arc is determined by its volt-ampere characteristic. The free-burning arc has over a range of conditions a falling characteristic, meaning that the voltage decreases with increasing current. Stable operation requires current control by the power supply, which is offered by practically all modern DC power supplies. For most plasma torches, the average arc voltage does not change strongly with changing current. However, increasing the gas flow rate will increase the arc voltage. The strongest effect has a change in plasma gas composition. A pure argon arc will have the lowest arc voltage, addition of helium or nitrogen will increase the voltage, and hydrogen in the arc will provide the highest voltage, that is, for a constant current also the highest power dissipation and strongest spray particle heating and acceleration. A variation in pressure will also change the voltage, with lower voltage at lower pressures (reduced heat losses) and higher pressures resulting in increased radiation losses and higher voltages. This holds, of course, only for the same arc current and the same arc length.

8.2.5 Electrode Erosion

Cathode erosion occurs mainly when the current density at the cathode attachment is high enough to result in larger molten volumes. This occurs when

- the attachment area is constricted, for example, by having a pointed conical cathode tip,
- there is a lack of low work-function material within the cathode,
- there is strong arc constriction due to the use of a molecular plasma gas such as hydrogen,
- the use of high currents exceeds the cathode design value.

The lack of low work-function material can occur when the material addition to the tungsten matrix evaporates faster than it can diffuse to the surface. This effect can be mitigated by the redeposition of the material when it is ionized after evaporation and driven back to the cathode surface by the cathode voltage drop [Zhou and Heberlein (1998)]. In general, cathode erosion affects torch operation during the first few hours, in particular during the first hour, resulting in a decrease in the arc voltage.

Anode erosion is caused by the strong heat fluxes of the constricted arc attachment between the arc column and the anode surface. For a constricted attachment through a cold gas boundary layer, it has been shown that an instability exists, leading to an electron temperature run-away and to localized evaporation of anode material [Yang and Heberlein (2007)]. Anodes of plasma-spray torches exhibit this type of erosion following the first few hours of operation. The erosion patterns can result in preferred arc attachment spots, leading to the establishment of preferred tracks for the arc attachment movements. A study of the erosion patterns and the associated arc voltage traces was reported. [Rigot et al. (2003)] have shown that the preferred anode attachment slightly moves upstream and becomes slightly more constricted with arc operation. The amount of erosion has been found to correlate with the residence time of the arc (time of a constant voltage value) at a specific location. Under normal conditions, this residence time varies from 30 µs to 150 µs, with the lower values occurring much more frequently. The relative distribution of the stationary arc attachment times for "New" and "Worn" anodes are given in Fig. 8.17 [Fauchais (2004)]. While for the new anode the attachment times remain smaller than 150 µs, the worn anode shows an increasing fraction of residence time at a specific attachment location exceeding this value. A thermal analysis indicates that with residence times of 150 µs, a strong increase in erosion can be expected, that is, once a slightly eroded spot has formed, the arc prefers to attach at this spot, rapidly increasing the erosion rate [Rigot et al. (2003)].

Anode erosion can also be strongly influenced by the anode design and the gas injection method. The results of a fluid dynamics study for a commercial plasma torch are given in Fig. 8.18 [Sun and Heberlein (2005)]. To observe the fluid flow in the torch, a glass torch was constructed; the arc heated gases were represented by a flow of heated helium emanating from the cathode tip, and cold argon gas was injected at the base of the cathode as in a conventional torch with three different gas injectors:

- commercial radial gas injector,
- commercial swirl gas injector with four injection holes,
- modified commercial gas injector with eight injection holes.

The flow was visualized by introducing fine particles with the gas flow. Flow simulations performed using a commercial CFD code indicated regions of flow recirculation, and the flow visualization experiments indicated powder deposits on the nozzle wall where the recirculation was predicted. Comparison with the erosion patterns of an actual plasma torch with an identical internal geometry indicated that erosion started at the

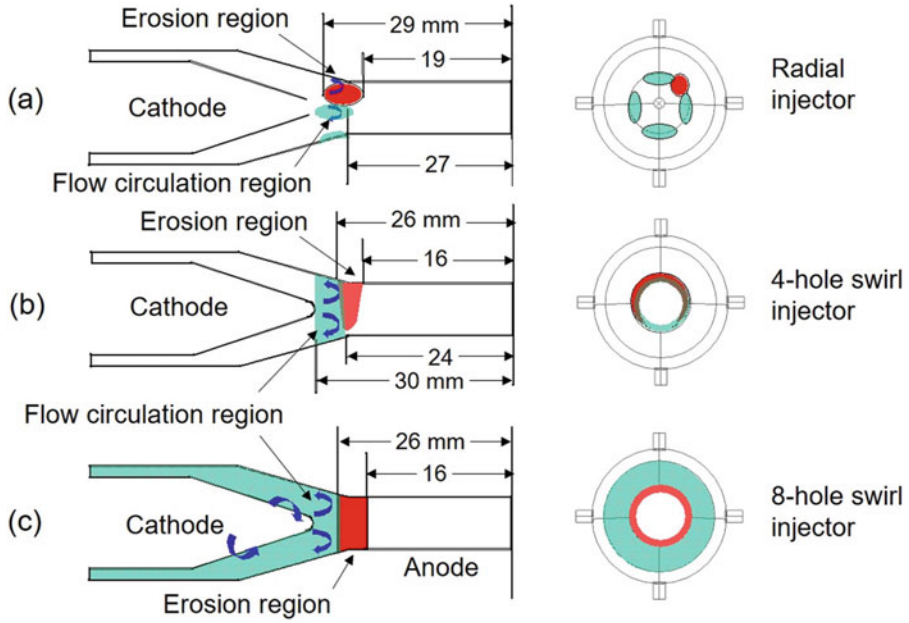

Fig. 8.18 Schematic indication of locations of the flow recirculation region, powder deposition, and observed erosion pattern for (**a**) radial gas injector, (**b**) 4-hole swirl gas injector, (**c**) 8-hole swirl gas injector. [Sun and Heberlein (2005)]. (Copyright © ASM International. Reprinted with permission)

spots where recirculation was predicted and powder deposits were observed. Clearly, radial gas injection results in rapid erosion in a region where recirculation can occur, in a circumferential location between two injection holes. The flow pattern of the four-hole swirl injector indicates that the gas is not swirling uniformly, but that stratified flow zones exist with stronger and weaker swirl velocities. Accordingly, there is circumferentially non-uniform erosion of the nozzle wall. The eight-hole swirl gas injector has the least amount of erosion, most uniformly distributed around the circumference, but predominantly in the region of recirculation [Sun and Heberlein (2005)].

Typically, plasma spray torch anodes can be used for 30 to 60 hours before they are eroded to a degree that the coating quality is strongly compromised. The number of arc-starts has also a strong impact on anode erosion due to the high currents associated with the high-frequency breakdown resulting in a pitted anode surface. Such an erosion mode can be limited by the use of argon as plasma gas for torch start-up and by limiting the start-up current to 100–150 A. A study of the long-term stability of the spray torch has shown that over the period between 10 and 40 hours of operation, the voltage and torch power decrease steadily, and the average particle temperatures proportionally [Leblanc and Moreau (2002)]. Since coating porosity is a strong function of particle temperature, maintaining a constant coating quality requires adjustment of torch power over this time period.

It is of interest to point out that while anode erosion reduces the average value of the arc voltage, it is responsible for increased voltage fluctuations. Both the absolute value of the voltage, and the amplitude and frequency of the voltage fluctuations can be used as a measure for erosion and process stability. Since the acoustic spectrum of the noise emitted by the arc is directly linked to such voltage fluctuations, recording this spectrum with a microphone can also be used as a means of detecting the erosion level of the electrodes and check if it has reached unacceptable levels [Duan et al. (2000)].

8.3 Plasma Torch Design

The basic DC plasma spray torch design has evolved considerably over the past two to three decades. The main objectives have been

- Improve plasma jet stability.
- Extend electrode life.
- Extend the range of plasma gases that could be used.
- Facilitate access to the plasma stream for injection of the spray material.
- Reduce ambient air entrainment into the plasma jet.
- Increase torch power for higher productivity.

Schematic representations of some of the basic concepts commonly used in the design of DC plasma spray torches are illustrated in Fig. 8.15. These differ mostly in the cathode design, which ranges from "stick-type" hot cathode

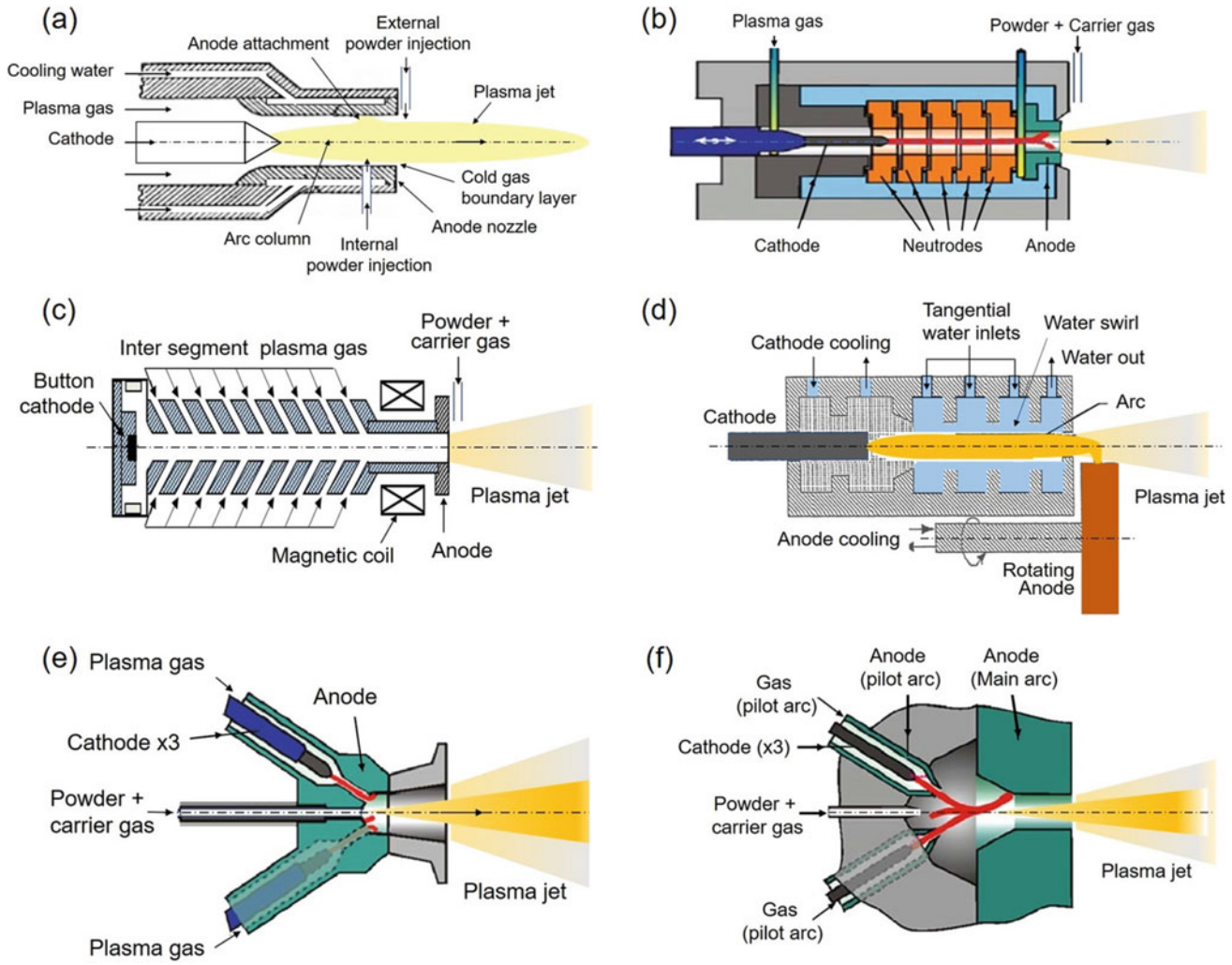

Fig. 8.19 Schematics of basic design concepts used for DC plasma spray torches (**a**) Gas-stabilized DC torch design, (**b**) Wall-stabilized torch design [Marqués et al. (2009)], (**c**) Segmented, Cascade plasma torch with inter segment gas injection [Zhukov (1979)], (**d**) Water-stabilized arc torch [Hrabovsky (1992)], (**e**) Converging plasma jet configuration [Marqués et al. (2009)], (**f**) Multi-cathode plasma torch. [Marqués et al. (2009)]

(Fig. 8.19a, b, e and f) to "button" cathode (Fig. 8.19c), consumable cathode (Fig. 8.19d), and multiple cathode arrangement (Fig. 8.19e, f). They also differ in the arc stabilization technique used, which ranges from "gas stabilized" (Fig. 8.19a, e, and f) to wall stabilized (Fig. 8.19b), segmented wall with inter-segment gas injection (Fig. 8.19c), and water-stabilized (Fig. 8.19e). In the following, a few examples the torch designs developed and used in plasma spray coating operations have been given.

8.3.1 Gas-Stabilized DC Plasma Torch

The design illustrated in Fig. 8.19arepresents the configuration used in the majority of "conventional" DC plasma spray torches in which an arc is struck between a water-cooled, "stick" type thoriated tungsten cathode, and a cylindrical, water-cooled copper anode coaxial with the cathode. Most of the torches manufacture the anode using oxygen-free copper for its higher thermal conductivity in order to ensure effective cooling of the anode walls and reduce anode erosion. The anode nozzle is typically between 5 and 8 mm in diameter, with its length between 1 and 5x its diameter. The plasma gas is introduced into the discharge cavity through a ceramic annular diffuser ring with a tangential velocity component, in most cases, in order to induce into the flow a swirling velocity component in order to ensure a uniform distribution of the plasma gas in the annular space between the cathode and the anode. The swirling motion of the plasma gas is also necessary for maintaining the arc root in constant movement over the surface of the anode in order to distribute the thermal load of the arc root heat losses on as large an area of the anode as possible and thus reduce its erosion. Because of the use of a tungsten cathode, this type of torches could

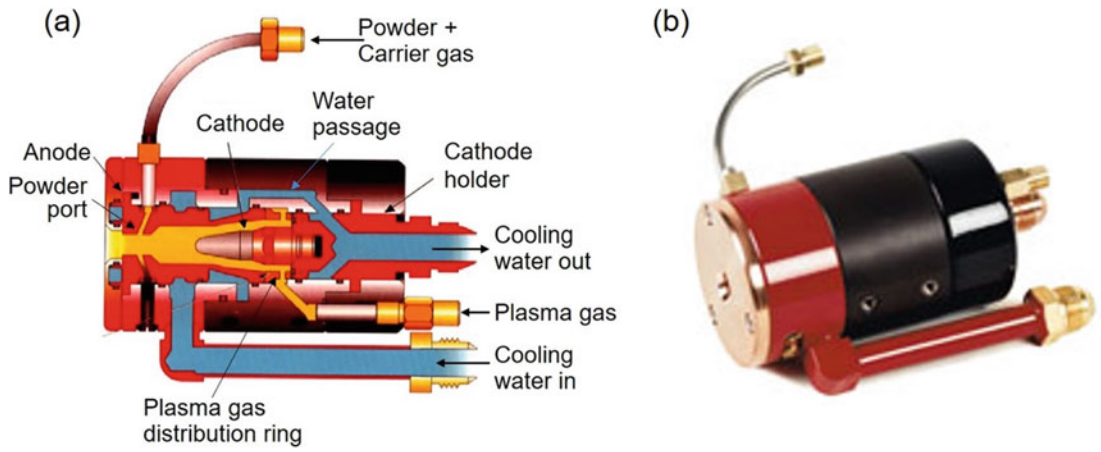

Fig. 8.20 (**a**) Schematic representation and (**b**) photograph of the SG-100, DC plasma spraying torch with internal powder injection by Praxair-TAFA cop Fig. 8.20 (a) Sectional

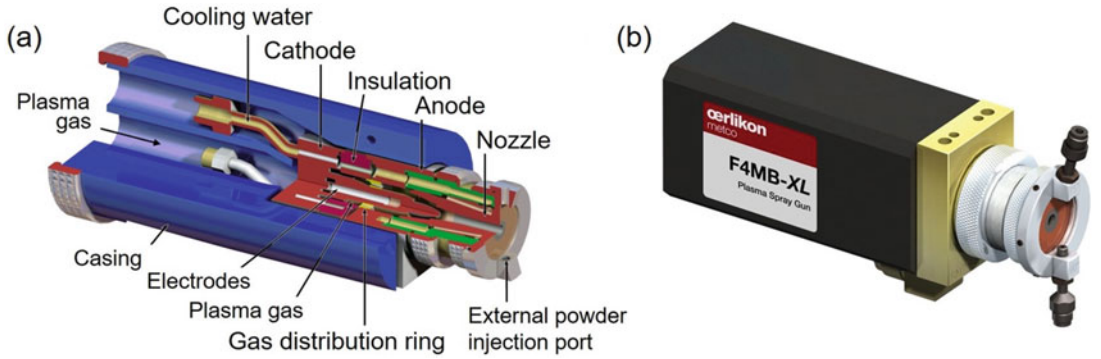

Fig. 8.21 (**a**) Sectional view and (**b**) photograph of the Oerlikon-Metco F4 MB-XL DC plasma gun with external powder injection. [Reproduced with kind permission of Oerlikon-Metco Corp]

only be used with inert or reducing plasma-forming gas. The presence of any oxygen in the plasma gas would result in the rapid oxidation of the tungsten cathode, forming a volatile tungsten oxide, leading rapidly to its destruction. Powder injection into the plasma stream is made radially, either internally through an appropriate channel into the anode wall, or externally at the exit level of the plasma jet from the anode nozzle.

Schematics and photographs of two of the leading torches used for plasma spraying are illustrated in Figs. 8.20 and 8.21, which are rated for operation at power levels up to 80 kW with anode nozzle diameters in the range of 5 to 8 mm i.d. Fig. 8.20 shows a schematic of the SG-100 by Praxair-TAFA DC gun with its high-pressure cooling water circuit (typically between 1 and 1.18 MPa) entering first on the anode side and exiting from the cathode side. The reverse sequence is sometime used depending on pressure drop across each of these two components. In many of these designs, the cooling-water hoses also carry the electric power cables for each of the two electrodes. As shown in the figures, the plasma gas is injected separately into the discharge cavity through a ceramic gas distribution ring, which serves to control the flow pattern in the discharge. The powder to be sprayed is injected into the plasma stream using a carrier gas internally into the anode nozzle. Fig. 8.21 shows a sectional view and a photograph of the F4 MB-XL DC plasma gun by Oerlikon-Metco Corp. It features a compact, relatively light-weight design (below 3 kg without the connecting cables) that which allows for easy mounting on a robotic arm. The torch is equipped with a double-port powder-injecting ring externally attached to the anode nozzle. One of the ports can be used for 90°

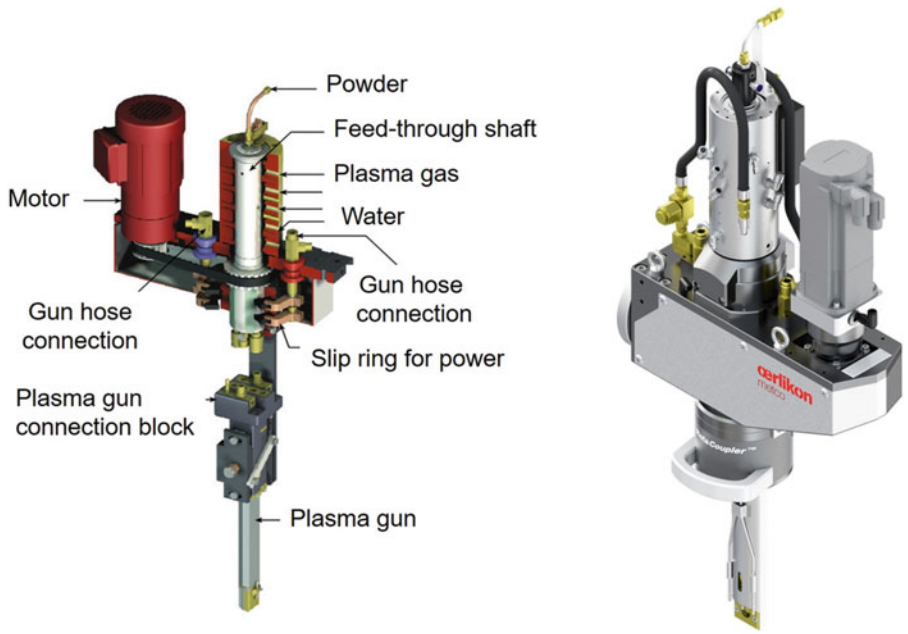

Fig. 8.22 Schematic of Oerlikon-Metco Rota-plasma torch for coating inside surfaces of cylinders. (Reproduced with kind permission of Oerlikon-Metco AG, Switzerland)

injection of the powder into the plasma stream, while the second port allows for a slight upstream inclination of the powder injection port.

With increasing demand for the use of plasma spraying for the coating of the interior surfaces of cylinder bores for aluminum cylinder blocks in the automobile industry, Sulzer-Metco developed a compact design of a DC plasma torch, commercialized under the name "Rota-Plasma," which is capable of rotation on its axis [Barbezat (2001)]. A schematic representation and photograph of an updated version of this torch is given in Fig. 8.22 (courtesy of Oerlikon-Metco Corp). The most notable of these developments is the compact torch design with the axis of the spray nozzle perpendicular to the axis of rotation of the torch body combined with its ability to operate under a harsh environment inside the cylinder bore during the coating process. The gas and cooling-water connections are made through a rotating feed-through shaft. The torch can be used for the coating of cylinder bores with diameters of as small as 60 mm, rotating at speeds up to 800 rpm, and power levels of 16 kW. Modular plasma-extension guns have also been developed for operating at higher powers, up to 90 kW (for the iPro-90 model), capable of coating internal bores as small as 150 mm and 600 mm deep.

8.3.2 Wall-Stabilized DC Plasma Torch

One of the problems with the arc-root fluctuations in conventional plasma spray torch presented in Fig. 8.15a are the development of large arc voltage fluctuations, which can be of the same order of magnitude as the mean arc voltage (typically a few tens of volts). These would result in a strong variation of the power dissipated in the torch and serious degradation of its powder melting capabilities. One way of overcoming such a difficulty is by significantly increasing the mean arc voltage through an increase in arc length and by improving its stability in the discharge cavity. The principle of wall stabilization of arcs has been known for more than 60 years; it was introduced in connection with arc lamps. The basic concept behind it is to confine the arc within a water-cooled circular channel in which the arc is to assume a rotationally symmetric, coaxial position. In the event of an accidental displacement of the arc toward the wall of the channel, the increase in heat conduction to the wall will result in the local cooling of the plasma in this location and, consequently a drop in its electrical conductivity, which will force the arc to return to its coaxial equilibrium position at the center of the channel. In this situation, increased thermal conduction to the wall of the arc confinement tube and the associated secondary effects represent the stabilizing mechanism.

Plasma torch designs providing stable arc operation by fixing the anode attachment location have long been used for plasma arc property studies [Maecker (1955), Zhukov (1994)]. Two methods can be used to elongate the arc: either by using a nozzle with a step diameter change in it or by having the channel consisting of a number of water-cooled segments, electrically insulated from each other and from the anode, called a segmented or cascaded arc. One problem with these designs is an enhancement of the anode erosion that

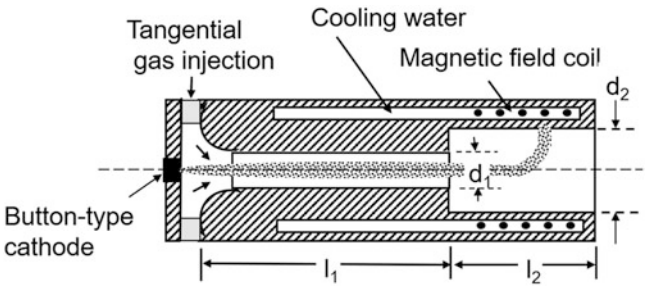

Fig. 8.23 Fixed anode attachment with a button-type cathode, injection of the plasma-forming gas as a vortex and an anode with a step. [Zhukov (1989a, b)]. (Reproduced with permission of VSP)

occurs with one fixed anode attachment. Limiting it requires reducing the arc current, but the higher arc voltage compensates for the lower power levels (about 3 to 6 times that of conventional spray torches.

The anode-nozzle with a step change in diameter is represented schematically in Fig. 8.23 [Zhukov (1989a, b)]. The length l_1 of the smaller diameter (d_1) part has to be shorter than the length l_{ca} that the arc would assume without the step change in the anode diameter d_2. Under such conditions due to the recirculation, which occurs downstream of the step change, the arc strikes close to this step change. To achieve a long free attachment in the nozzle of diameter d_1, a strong vortex must be used with a high swirl, which can be achieved when the ratio d_v/d_1 is high, d_v being the diameter of the gas injection tangentially to the arc chamber. This high vortex requires using a button type cathode. For low arc currents, the arc characteristic is first slightly decreasing and then slowly increasing [Zhukov (1994)].

In order to cope with the extremely high wall heat fluxes experienced with high-intensity arcs enclosed in small-diameter channels, Maecker introduced the concept of using a stack of electrically insulated, water-cooled disks (usually made of Cu), often referred to as "neutrodes," as shown in Fig. 8.24, leading to what is commonly known as the wall-stabilized, cascaded arc, which has been extensively used as a basic research tool. The same principle found widespread application in the design of high-power arc gas heaters with considerably higher arc voltages. Due to the much higher electrical conductivity of metals compared with that of the arc column, segmentation of the channel enclosing the arc is necessary because a continuous metal tube would cause a double arc through the metal wall (arcing from the cathode to the metal tube and from the metal tube to the anode) seeking the path of least resistance. If E is the field strength in the arc column and δ_x the thickness (in field direction) of an individual segment, the following condition has to be met for avoiding double arcing:

$$\int_0^{\delta_z} E\, dz \leq (V_c + V_a) \tag{8.9}$$

The minimum voltage required for establishing and maintaining an arc is the sum of the cathode fall, V_c, and the anode fall, V_a. A reduction in the inside diameter of the segments (arc constriction) leads to a marked increase of the field strength, keeping the other arc parameters the same, and accordingly to higher energy losses by heat conduction. In this situation, the maximum thickness of a segment may be limited to $\delta_z = 1.2$ to 2.0 mm. It is essential for retaining the wall-stabilizing effect that the diameter of the channel containing the arc be smaller than the diameter of a free-burning arc operated under the same conditions. If the channel diameter is too large, the stabilizing effect due to heat conduction is lost and, at the same time, free convection effects may cause serious distortions to the arc column.

With these torches, a much higher voltage between the cathode and the anode is obtained. Limiting its axial movement to the anode length stabilizes the long arc. If at the anode, voltage fluctuations ΔV can reach ±40 to 50 V with molecular gases and especially hydrogen, as the mean arc voltage V_m can be higher than 150 V, effects of fluctuations are significantly reduced. As the erosion of electrodes depends essentially on the arc current and fairly little on the voltage, power levels 3 to 4 times higher than with conventional torches without compromising anode erosion and electrode life.

8.3.3 Laminar Plasma Torch

Numerous studies, especially in China, have been devoted to the development of laminar plasma jets because of their inherent stability and long contact time between the particle and the plasma flow, which could represent a significant improvement in system controllability and material-processing technology [Pan et al. (2001), Liu et al. (2018), Liu et al. (2019)]. The approach used has mostly been centered on improving arc stability through modification of the internal geometry of the arc confinement channel and operating conditions. A schematic of the DC plasma torch used by [Pan et al. (2001)] is given in Fig. 8.25. This features the introduction of an interelectrode insert between the cathode and anode of the torch which serves mainly to confine the arc root movement of the surface of the anode to a limited circular range. The anode nozzle diameter was varied over the range of 4 to 10 mm, separate main gas inlets were incorporated in the design, allowing for the introduction of the gas in the torch either tangentially to the wall of the discharge cavity or in a linear flow mode in the axial direction

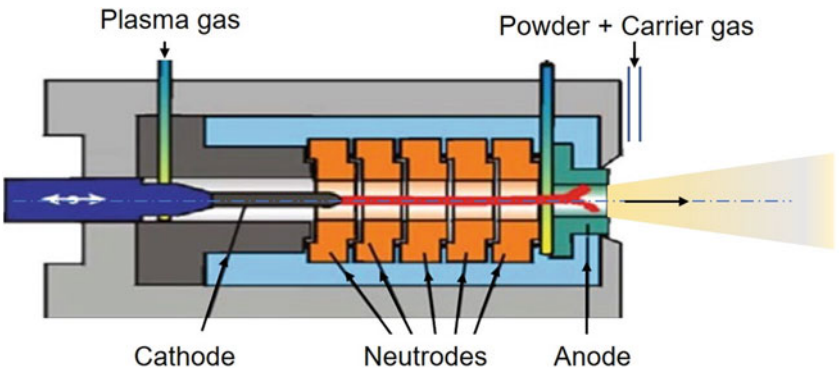

Fig. 8.24 Schematic of a plasma torch with neutrodes: Advanced Plasma Gun (APG). [Marqués et al. (2009)]

of the torch. Provision was also made for the tangential introduction an auxiliary gas stream downstream of the cathode region for a closer control of the flow pattern and the composition distribution in the gases while operating with mixed plasma gases. Results are given operating with a plasma gas composed of [4.8 slm (N_2) +8.4 slm (Ar)] with an 8 mm i.d. anode nozzle at an arc current of 160 A. A photograph of the plasma jet obtained, given in Fig. 8.22, shows a long, stable plasma jet with a length-to-diameter ratio of 45. The effect of the total gas flow rate and the mode of injection of the gas into the discharge cavity were investigated for a pure argon plasma generated by the same torch with an anode diameter of 8 mm, operated at essentially the same conditions as those used earlier.

Photographs given in Fig. 8.27a show a rather turbulent jet generated with a plasma gas flow rate of 27 slm (Ar) and an arc current of 160 A. Fig. 8.27b and c, obtained with a lower gas flow rate of 13.2 slm (Ar), shows, on the other hand, a considerably longer and more stable plasma jet due to the lower gas flow rate for the same arc current. The authors point out that the apparent difference in arc length of the two jets was caused by the different inlet modes of introduction of the plasma working gas. The gas was fed along the torch axis for the jet shown in Fig. 8.27b and tangentially with the channel wall for the jet shown in Fig. 8.27c. The results indicate that a vortex motion of the gas in the discharge cavity would be favorable for lengthening the plasma jet compared to the axial injection mode. The authors attributed the effect to arc stabilization by the vortex motion in the discharge cavity. Throughout this study, the authors point out to a direct correlation between the operation of the plasma torch in the laminar mode with a stable plasma jet and the significant reduction in the noise level associated with running the plasma torch.

A wall-stabilized design of a DC plasma torch was reported by [Liu et al. (2019)] for the generation of silent, stable, and super-long laminar plasma jets in atmospheric air. A schematic of the DC, non-transferred laminar plasma torch (ZH-30, Zhenhuo Plasma Technology Co. Ltd., Chengdu, China) used in this study is given in Fig. 8.28. Basically, it is comparable with the design proposed earlier by [Marqués et al. (2009)], see Fig. 8.24, composed of a cathode, insulated inserts (neutrodes), an anode, and a nozzle outlet. The diameter of the nozzle exit is 5 mm, with the neutrodes assembled using intersegment insulating rings to extend and constrict the arc column in a cylindrical channel. The length of the insulated inserts can be changed depending on the desired applications. The trumpet-like structure is innovative for laminar jets and beneficial for their stable generation.

The results given in Fig. 8.29 were obtained at atmospheric pressure, with a mixture of Ar/N_2 as plasma gas (30 vol.%

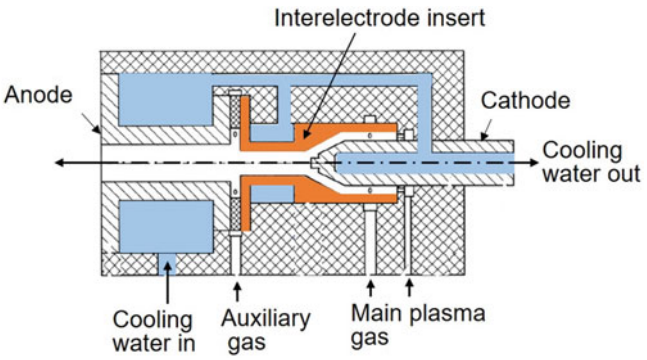

Fig. 8.25 Schematic of the modified DC plasma torch used for operation in the laminar plasma mode. [Pan et al. (2001)]

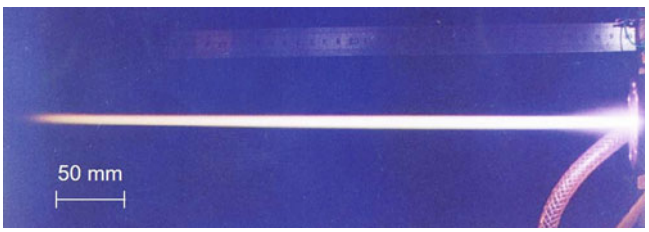

Fig. 8.26 Argon/Nitrogen laminar plasma jet generated using 4.8 slm (N_2) +8.4 slm (Ar) as plasma gas and arc current of 160 A. [Pan et al. (2001)]

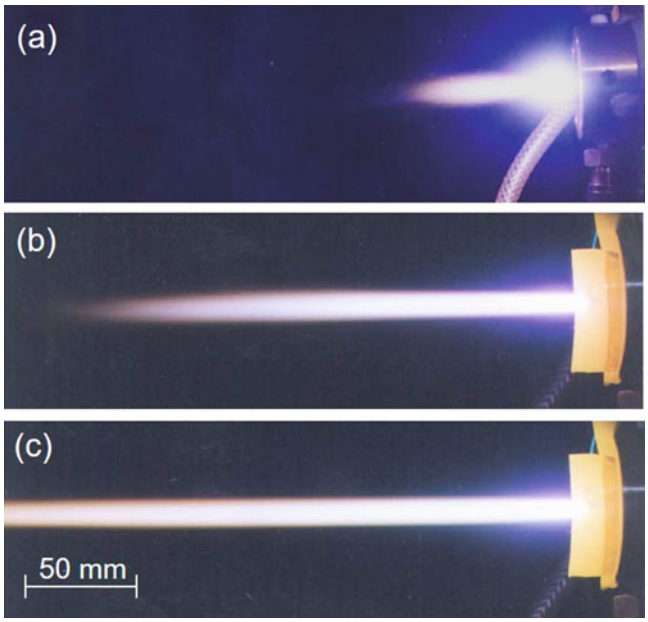

Fig. 8.27 Argon plasma jets generated with an arc current of 160 A, and gas flow rate of (**a**) 27 slm, (**b**) 13.2 slm, axial gas injection, (**c**) 13.2 slm, tangential gas injection. [Pan et al. (2001)]

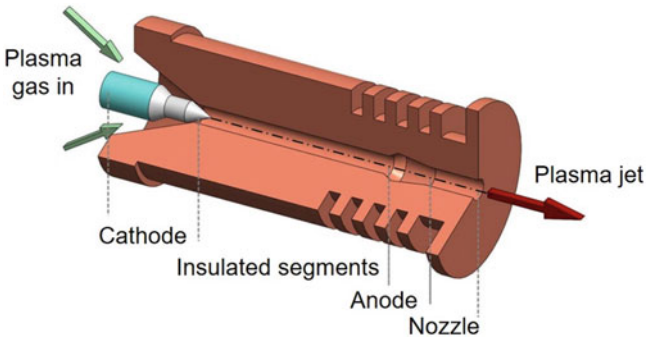

Fig. 8.28 Schematic diagram of internal structure of the laminar plasma torch. [Liu et al. (2019)]

Ar + 70 vol.% N_2) at gas flow rates of 8.5 to 15.00 slm, arc currents varying from 60 to 165 A, and torch power of 8.5 to 28 kW. The length of the corresponding laminar plasma jets varied from 100 to 720 mm with an ambient generated noise level of <80 *dB*. When the inlet gas rate was outside this range, lower than 8.5 slm or higher than 15 slm, the plasma jets become uniformly shorter (about 80 mm) and extremely noisy (about 110 dB) because of intense entrainment of ambient air, just as in the case of conventional direct-current non-transferred arc plasma jets. The photographs given in Fig. 8.29a, obtained for a gas flow rate of 8.5 slm and arc currents varying between 60 and 165 A, show a steady s of the length of the plasma jet with increase in the arc current. The arc stability, however, seems to be very sensitive to the plasma gas flow rate since, as shown in Fig. 8.29b, the increase in the plasma gas flow rate from 8.5 to 15 slm results in a significant decrease in the length of the plasma jet for the same current rating. Observations of temporal evolution of the plasma jet appearance and the voltage demonstrated, however, that the jet is highly stable in the atmospheric environment over the range investigated.

8.3.4 Cascade DC Plasma Torch with Intersegment Gas Injection

As demonstrated by [Zhukov (1994)] and his coworkers, the need for additional gas injection arises from the behavior of long arcs stabilized by a vortex flow as shown schematically in Figs. 8.19c and 8.30. In these conditions, the length of the segments surpasses the limit at which double arcing would occur. The cold gas injection, which creates a new cold boundary layer simultaneously, reduces the heat losses to the wall. This principle has been successfully used in high-enthalpy, high-power torches for re-entry simulation. The arc voltage in these conditions is much higher than those obtained with conventional plasma spray torches.

The fraction of the total mass flow rate of the sheath gas, which is injected in the i^{th} segment, is defined as $x_i = (\rho_i v_i / \rho_o v_o)$, whose value can vary between 0.1 and 1. The index "o" corresponds to the mean gas conditions in the torch. v_i is the gas injection velocity, which can be in the range of 0.5–0.7 the velocity of sound in the cold plasma forming. [Zhukov (1994)] proposed a semi-empirical relationship between the mean ratio, $\overline{R_z}$, of the segment length $\overline{\delta_z}$ to its diameter d_c by

$$\overline{R_z} = \frac{\overline{\delta_z}}{d_c} = \frac{1.3 \times R_e^{0.25}}{\left(1 + 1.85 \times 10^{-3}\left(I/\left(d_c \times \sqrt{\mu_0 h_0 \sigma_0}\right)\right)\right.} \quad (8.10)$$

With, I, μ_o, h_o, and σ_o being respectively the current (A), the viscosity (kg/m. s), the specific enthalpy (J/kg), and the electrical conductivity (A/V. m) of the plasma at the temperature T_o corresponding to 1 vol.% of electrons. The Reynolds number, *Re*, is calculated using the following expression:

$$Re = \frac{\dot{m}_g}{\mu_o d_o} \quad (8.11)$$

Where, $\dot{m}_g$ is the total gas flow rate (kg/s) and d_o the internal diameter (i.d.) of the cylindrical nozzle, and μ_0 is the viscosity of the plasma at the temperature T_o corresponding to 1%

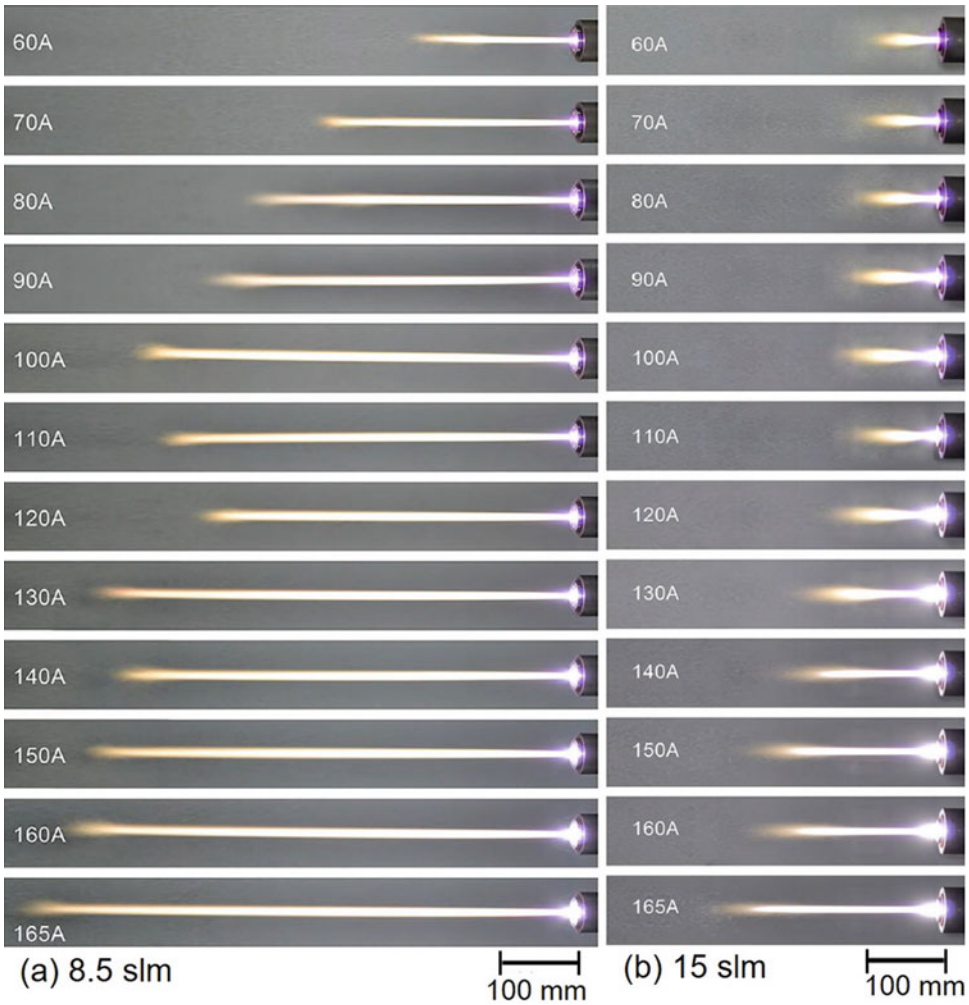

Fig. 8.29 Variation in the length of an atmospheric pressure laminar plasma jet (Ar 30 vol% + 70 vol.% N_2) for different plasma gas flow rates and arc currents (**a**) 8.5 slm, (**b**) 15 slm. [Liu et al. (2019)]

of electrons. For (I/d_c) values between 1–10^4 A/m and $Re = 10^4 to\ 10^5$, Eq. 8.10 predicts values of $(\overline{R_z}.Re^{-0.25})$ between 1.3 and 0.8.

High electric fields and correspondingly high voltages (up to 6–8 kV) are feasible with such torches, which are commercially available, for example [Acurex, Aero Therm Mountain View, CA 94043, SKF, Santen et al. (1986) and Thörnblom (1989), and Aerospatiale, Van den Brook et al. (1987)]. They have also been extensively developed in the former USSR [Pustogarov (1994), Zhukov (1989a, b)]. This principle has been successfully used in high-enthalpy, high-power plasma torches for re-entry simulation, with power ratings in the range from 50 kW to 5 MW. The EDP-119 Plasma torch (referred to in the Russian literature as Plasmatron), illustrated in Fig. 8.31, is an example rated for 500 kW [Zhukov and Zasypkin (2007)]. A scaled-down version of this design to the 100 kW power level was recently adapted by [Belashchenko (2010)] for plasma spray coating applications.

8.3.5 Water-Stabilized DC Plasma Torch

Water was used as a stabilizing medium for an electric arc in the early 1920s [Gerdien and Lotz (1922)], mainly to achieve higher plasma temperatures. The high specific heat of water, steam, and hydrogen/oxygen was used in this case to constrict the arc, increase its voltage and local energy generation, and consequently increase the arc temperature. These basic phenomena were used at the Institute for Plasma Physics of the Czech Academy of Sciences [Hrabovsky (1992), Chraska and Hrabovsky (1992)] for the development of the water-stabilized plasma torch, as schematically illustrated in Fig. 8.19d. The first version of the torch was based on the use of a consumable carbon electrode as cathode and a water-cooled external, rotating copper disc as anode. The electric arc crossing the plasma torch was confined by a narrow circular channel created by a high-velocity vortex flow of water in the discharge cavity. The water is introduced into the arcing chamber with a strong swirl component in several sections,

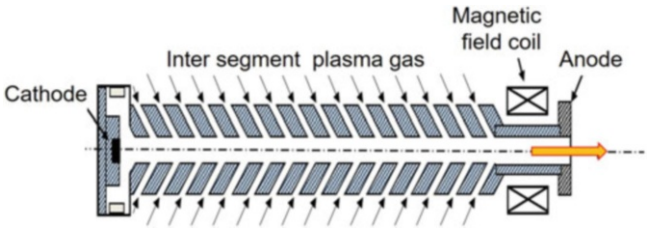

Fig. 8.30 Principle of an arc constrictor with insulated segments and intersegment gas injection. [Zhukov (1979)]

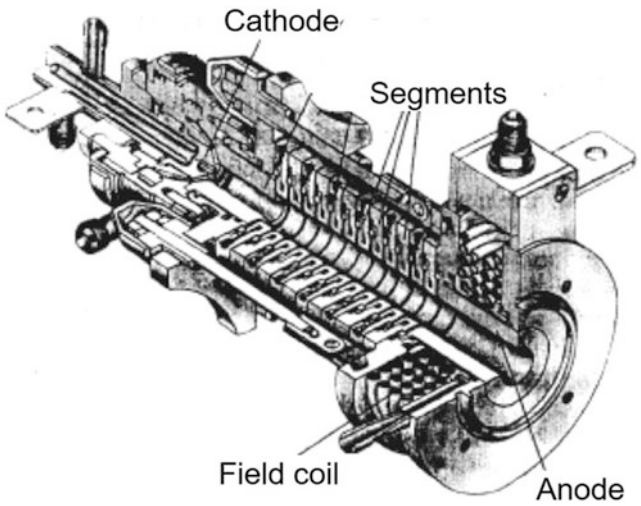

Fig. 8.31 Schematic of the EDP-119 plasma torch. [Zhukov (1977)]

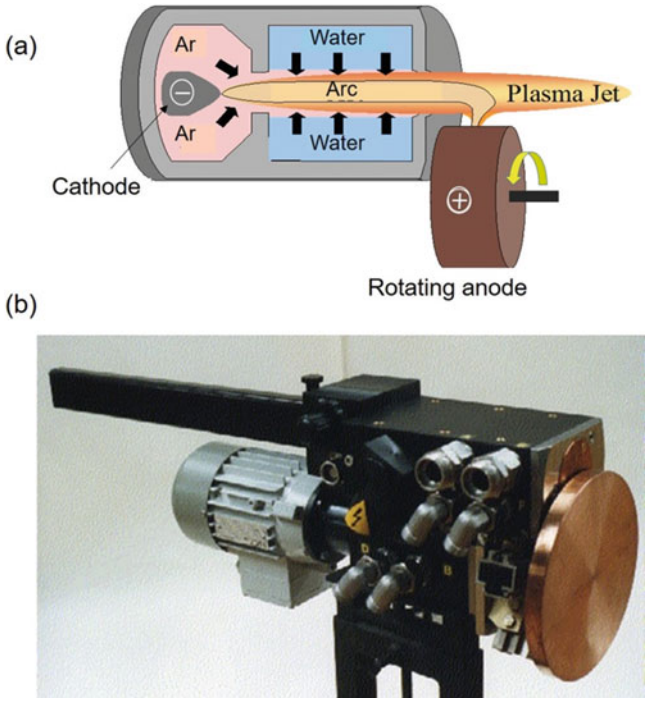

Fig. 8.32 (**a**) Schematic and (**b**) photograph of a water-stabilized arc plasma torch with an external rotating anode. (With kind permission of Milan Hrabovsky and the Institute of Plasma Physics of the Czech Academy of Sciences)

and an outlet right before the torch nozzle allows a return of the unused water. The arc is established through a contact electrode and transferred from the cathode to the external anode. The plasma gas is provided by the evaporation of the water that is heated by the electric arc before exiting the torch through a nozzle, as a high-velocity plasma jet. The anode is rotating at a high speed to distribute the high heat load received from the plasma and the anode-root attachment.

As the torch design evolved, a water-cooled cathode with an argon gas shield was used to replace the consumable graphite electrode, which was limiting the ease at which the torch could be integrated in normal plasma-spraying operations. Environment in the upstream part of the torch (hybrid torch) providing significantly increased operation times. A schematic of the torch using the shrouded cathode, in combination with the rotating water-cooled anode, is given in Fig.8.32a; a photograph of the torch, courtesy of Dr. Milan Hrabovsky, is given in Fig. 8.32b. The strong cooling of the arc results in very high arc voltages (260 to 300 V) and high torch powers (80 to 200 kW) for moderate currents (300 to 600 A). Temperatures at the nozzle exit can reach 28,000 K, and peak plasma velocities of 7000 m/s have been reported [Hrabovsky et al. (1995)]. A comparison between the performance of water-stabilized torches and that of gas-stabilized torches in terms of power per unit mass of plasma medium is given in Fig. 8.33. As can be noted, for an equivalent power rating, water-stabilized torches operate at a considerably lower mass flow rate of the plasma medium (water + Ar as shield gas) than gas-stabilized torches (Ar/H_2 or Ar/N_2). Only a small fraction of the mass is used, with the torch achieving the high power and enthalpy levels in the plasma jet. These values allow for spray rates in the range of 25 to 45 kg/h for ceramics and 80 to 100 kg/h for metals, which are an order of magnitude higher than that for regular plasma torches operating at 40 to 50 kW, and still significantly higher than that of high-power plasma torches operating at 200 kW with a nitrogen-hydrogen mixture. The high deposition rates make this torch particularly useful for the manufacturing of free-standing shapes or for coating large areas. However, the external rotating anode makes torch movement somewhat more difficult.

8.3.6 Multi-Electrode DC Plasma Torch

As was discussed earlier in Chap. 5, "Plasma and particle dynamics in thermal spray," special attention has been devoted to powder injection in plasma streams in order to optimize their trajectories and extend their residence time in the plasma stream to achieve the best thermal processing conditions for the precursor material. When using

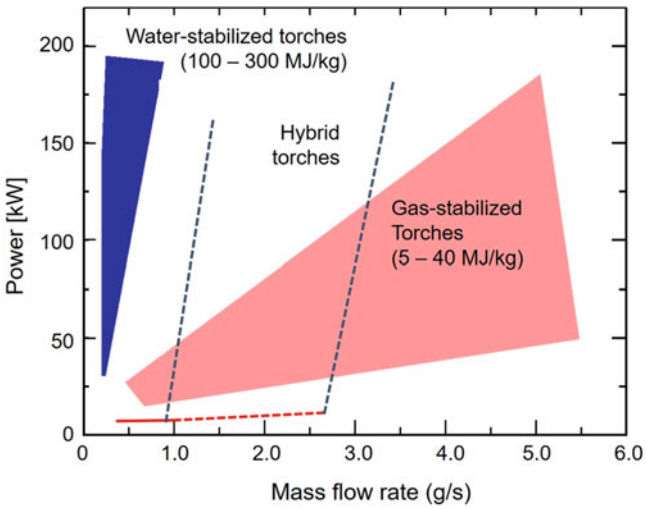

Fig. 8.33 Illustration of torch power variation with plasma mass flow rate for water swirl stabilized and for gas-stabilized torches. (With kind permission of Milan Hrabovsky)

conventional DC plasma sources for spraying operation, considerable challenges are met due to the high energy density, high velocity, and relatively small diameter of DC plasma jets, which are dependent on the torch nozzle diameter, typically in the range of 4 to 8 mm i.d. Particle injection from one side of the plasma flow also leads to the classification of particle trajectories according to their initial momentum. Particles with higher mass and injection velocity can penetrate the plasma jet and traverse it, having the majority of their trajectories in the low temperature fringes of the jet on the opposite side of their injection location. In contrast, particles with too low a momentum (lower mass and/or lower velocity) will not be able to penetrate the plasma jet and will remain in the fringes on the injection side. Neither of these groups of particles will have the required temperature and velocity for the formation of a dense coating with good adhesion to the substrate.

The use of multiple plasma sources converging to a single point has long been considered a viable option for increasing the volume of the discharge, allowing for an easier access for central injection of the precursor into the plasma. Specific design options were proposed by [Fukanuma (1988), Marantz and Herman (1991, 1992), Muehlberger et al. (1994), Chen et al. (2000) and Marqués et al. (2009)] for the use of a multiple converging plasma torch configuration or multiple cathodes, with a single-anode configuration, with the arc transferred to either an internal or an external common anode, as illustrated respectively in Fig. 8.19e and f. These would allow for the stabilization of the arc length, a reduction in the fluctuation of the arc voltage and torch power, and an increase in plasma volume. As pointed out by [Marqués et al. (2009)], one of the inherent problems in all of these systems is the need to ensure that the reactant stream is uniformly

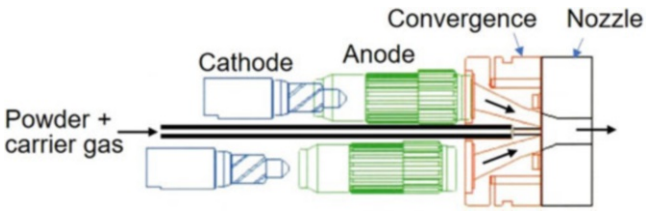

Fig. 8.34 Schematic of Northwest Mettech Axial III central injection torch. (Courtesy of Northwest Mettech)

contacted and distributed in the plasma stream formed from the converging discrete plasma jets. Nozzle blocking or "spitting," defined as the periodic burst of released precursor material built-up on the system walls, or exit nozzle, is another common problem that has been observed. None of these systems finally had a significant technological or commercial success.

The commercial torch Axial III was developed at the University of British Colombia by Doug Ross in 1990 and exclusively licensed to Northwest Mettech (Canada) [Moreau et al. (1995), Burgess (2002)]. The basic design of the Axial III torch, as illustrated in Fig. 8.34, consists essentially of three cathode-three anode spray torches, arranged such that their axes are parallel, surrounding the powder feed tube placed along the central axis of the torch, followed by a convergent section. The powder is injected with an axial trajectory at the point where the three plasma streams converge. As the powder is entrained by the plasma gas, the individual particles are accelerated and heated to their melting temperature before exiting the torch through the torch nozzle (8–25 mm i.d.). A sectional 3-D view of the internal torch construction and a photograph are given in Fig. 8.35 (courtesy of Northwest Mettech). The torch operates using either argon or nitrogen as the primary plasma forming gas to which hydrogen or helium can be added depending on the required spraying conditions. The maximum gas flow rates are factory set at 400 slm (Ar), 200 slm (N_2), 100 slm (H_2), and 140 slm (He). The individual arc current can be set at 3×30–250 A, with electrode voltages 60–200 V, for a maximum power rating between 50 and 150 kW. Cooling-water requirement is 50 l/min at a pressure of 1.4 MPa (200 psig). The principal advantage of the Axial III torch is its high powder-feed rate, up to 120 g/min (7.2 kg/h) and high deposition efficiency (80%). The torch has been successfully demonstrated for use with powders, liquids, or suspensions as feed material with coating quality less sensitive to the powder material, that is, size distribution and morphology, compared to standard DC plasma spray torches. However, the problem of plasma/arc fluctuations remains.

A development by the Universität der Bundeswehr, Munich, and Sulzer Metco, has succeeded in solving the problem of plasma arc instability and increased anode erosion by dividing the arc current into three separate arcs with three

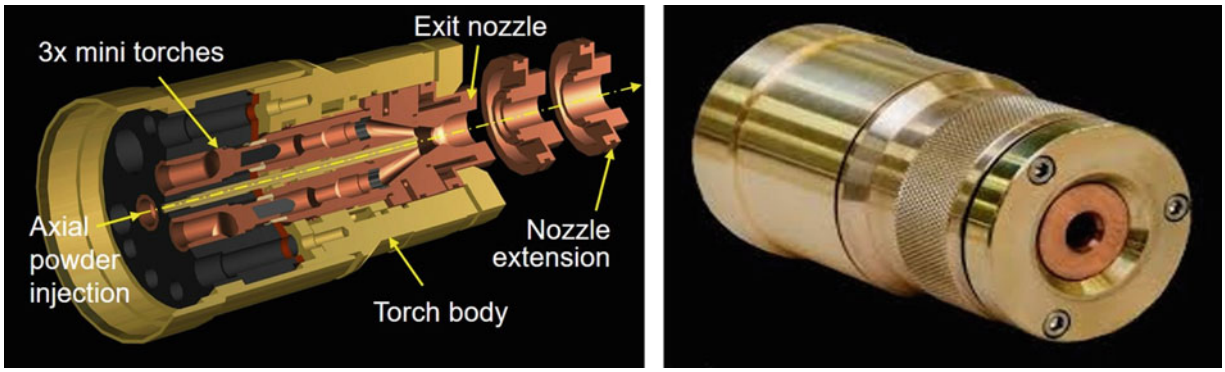

Fig. 8.35 (**a**) Sectional view and (**b**) Photograph of the Northwest Mettech Axial III central injection torch. (Courtesy of Northwest Mettech)

Fig. 8.36 Sectional view of Orelikon-Metco Triplex Torch. (Reproduced with kind permission of Orelikon-Metco AG, Switzerland)

cathodes and three separate anode attachments ("Triplex" torch, see Fig. 8.36, courtesy of Orelikon-Metco) [Zierhut et al. (1998), Barbezat and Landes (2000a, b)]. As shown in Figs. 8.36a and 8.37a, the arc length is extended through the use of several insulated segments, which constitute the wall of the arc channel, giving rise to a higher operating voltage of the torch (around 100 V). While the individual arc root fluctuations at the anode are the same as those for a conventional DC plasma spray torch with a stick-type cathode (for example, about $\Delta V = \pm 10 - 15$ V), their relative value to the mean arc voltage for Ar-He plasma is considerably lower for the Triplex torch compared to a conventional torch, Fig. 8.38. Considering that for a conventional torch operating with Ar/He mixture as plasma gas, the mean arc voltage V_m can be around 35 V and the ratio $\Delta V/V_m$ would be at 15/35 (43%). In contrast, the corresponding value of the $\Delta V/V_m$ ratio for the Triplex torch would be 15/100 (15%).

This torch also offers a very stable operation with argon or argon-helium mixtures, with a significant increase in the powder feed rate. However, powder injection is external to the plasma torch immediately downstream of the anode, using single or multiple three injectors adjusted 120° around the periphery of the exit nozzle for the torch, as shown in Fig. 8.36b. The improved arc stability, lower turbulence in the jet, and the use of three injection systems allow for higher deposition rates in addition to better process control and longer operating time. The anode-nozzle i.d. is between 6 and 9 mm. When observing the plasma jet for small anode-nozzle diameters, it can be observed that they consist of three lobes, as shown in Fig. 8.37b (courtesy of Oerlikon-Metco). Thus, particles can be injected either into the lobes or between the lobes, the latter injection being called the cage effect.

Emission tomography studies of the temperature field of the generated plasma jet, using three CCD cameras rotating around the jet axis, were reported by [Mauer et al. (2011a, b)]. The results allowed for the tomographic reconstruction of the gas temperature distribution and a better positioning of the powder injectors in the regions of high gas temperature and thus of high gas velocity and viscosity. In all investigated cases, the most efficient particle heating corresponded to an injection direction between two high temperature lobes, thus confirming the so-called "cage effect" [Mauer et al. (2011b)]. As can be noted in Fig. 8.37b, the lobe opposite to the injector kept in particular the larger particles properly in the jet center and prevented them from passing through the plume due to their too high momentum. As particle velocities were found to vary only moderately, the particle temperatures were more meaningful

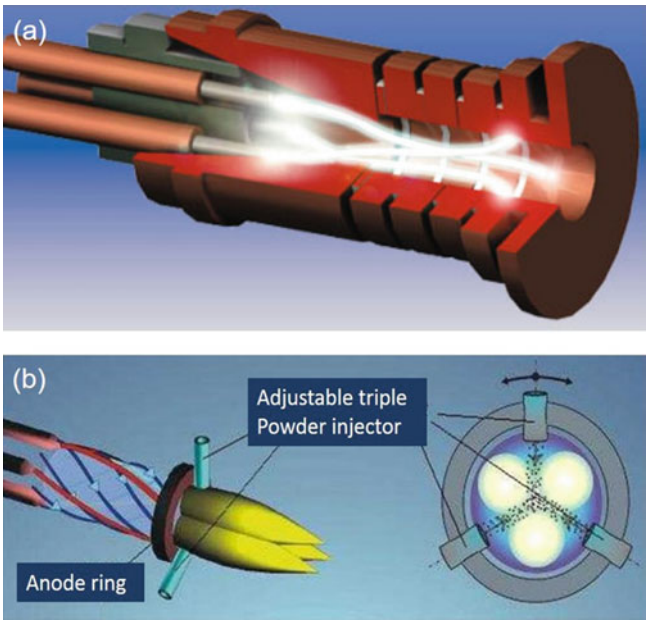

Fig. 8.37 (**a**) Sectional view, (**b**) 3-D representation of the arc lobs inside the of Sulzer Metco Triplex Torch. [Mauer et al. (2011b)]. (Reproduced with kind permission of Orelikon-Metco AG, Switzerland)

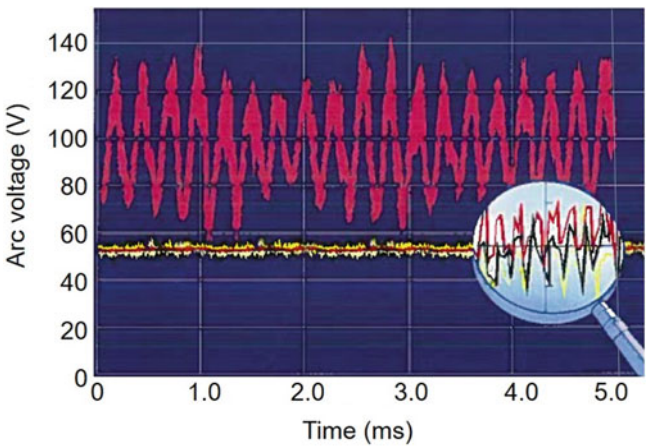

Fig. 8.38 Comparison of a typical voltage fluctuation signal for a standard DC plasma torch (toptrace) compared to the a Triplex torch (bottom trace [Barbezat G and K Landers])

when the injection conditions were to be optimized. The results showed that particle injection between the hot lobes, combined with an appropriate carrier gas mass flow rate, allowed for the optimization of the process effectiveness as a function of the size of the injected particles.

The Triple Torch Plasma Reactor (TTPR) developed by Pfender and his collaborators at the University of Minnesota represents another use of multiple electrode arrangement for powder synthesis and spraying experiments [Lu and Pfender (1989)], [Young and Pfender 1989)]. As shown schematically in Fig. 8.39 [Chen et al. (2000)], the system is composed of three torches arranged inside a controlled atmosphere chamber with an adjustable angle to the chamber axis and distance to a central substrate holder. The three plasma jets join to form an enlarged plasma region. The powder is injected through a central water-cooled injection tube on the axis of the reactor, close to the location where the three jets join to form the combined jet. Three power supplies are necessary to operate the reactor. Operating currents can be varied between 250 and 320 A with Ar or Ar-H_2 mixtures as the plasma gas. Enthalpy probe measurements of the plasma flow show a rather uniform temperature and velocity field over a relatively large surface area of the substrate [Asmann et al. (2001)]. The temperature and velocity in the central portion of the plasma jet can be adjusted by changing the carrier gas flow rate, that is, higher carrier gas flow rates will result in cooling of the central portion of the jet and reduced particle heating. Clearly, coating of complicated shapes will be difficult because the torches cannot be moved independently, but the substrate can be moved. This torch has been used for specialty coatings, such as the three layers of a solid oxide fuel cell (SOFC), where in a single process, the porous Ni-YSZ anode layer, the high-density YSZ electrolyte layer (with 99.5% density), and the porous lanthanum manganite perovskite cathode layer were deposited [Chen et al. (2000)].

8.4 Gas and Particle Dynamics in DC Plasma Spraying

This section is devoted to a discussion on the gas and particle dynamics in DC plasma torches and their dependence on the torch design and its operating conditions. The subject is treated in three district subsections dealing first with the characteristics of arc and gas dynamics, which build on Sect. 8.2.4 arc instabilities, and their impact on the gas dynamics in the plasma jet. This is followed by a discussion on the time-averaged, steady-state characteristics of the plasma jet and its interactions with ambient atmosphere. The important topic of particle injection into the plasm jet is treated next, which builds up on the fundamental concepts developed earlier in Chap. 5, Gas and Particle Dynamics in Thermal Spray.

8.4.1 Arc and Plasma Jet Dynamics

As mentioned earlier in Sect. 8.2.4, arc instabilities are inherent to the basic configuration of the design of DC plasma spray torches with a central hot cathode surrounded by a water-cooled, coaxial annular anode forming the torch nozzle. The arc is stuck between the cathode tip, which is usually in the form of a sharp cone, “stick-type cathode,” and the anode walls. The arc-root bridging the anode boundary layer,

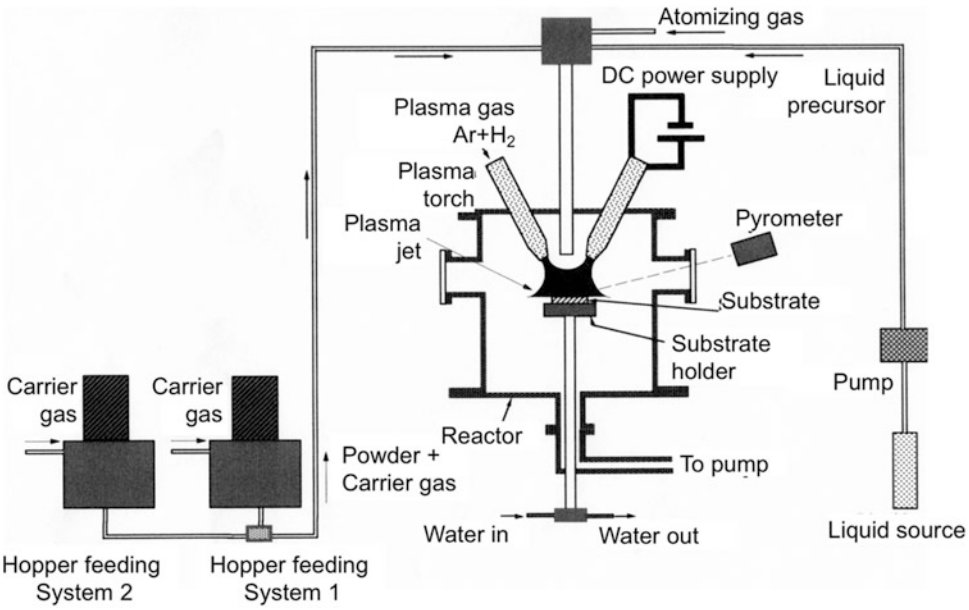

Fig. 8.39 Triple Torch Plasma Reactor with three torches in controlled atmosphere chamber and central injection and multiple powder/liquid feeders. [Chen et al. (2000)]. (Copyright © ASM International. Reprinted with permission)

connecting the arc column to the point of attachment on the anode surface, is exposed to multiple forces, the most important of which are the drag force exerted by the gas flow in the direction of the gas stream and the electromagnetic force due to the self-induced magnetic field. In the case of torch designs incorporating a magnetic field coil such as those illustrated in Figs. 8.23, 8.30 and 8.31, the applied field will also exert an additional electromagnetic force on the arc root forcing its continuous movement on the surface of the anode. The resulting arc movement illustrated on the LHS of Fig. 8.40a and supported by the highspeed images given on the RHS Fig. 8.40a, after [Wutzke et al. (1967)], gives rise to corresponding arc-voltage fluctuations typical of the restrike mode of operation, as illustrated in Fig. 8.40b, after [Coudert et al. (1966)].

Such strong arc voltage fluctuations encountered in the restrike mode of operation are promoted by thick boundary layers between the arc and the anode nozzle wall, which mostly exist under conditions of low currents, high plasma gas flow rates, and high percentages of molecular gases such as hydrogen or helium. However, restrike-like behavior can also be observed when the anode is eroded, and a preferred track exists for the motion of the anode root attachment. The restrike motion is usually characterized by a specific frequency in the low kHz range (2–6 kHz), and increased erosion will give rise to a voltage fluctuation with this frequency. Fig. 8.41 [Duan et al. (1997)] shows the Fourier transform of arc voltage fluctuations progressing from a random distribution, at the top of the figure for a new anode, to a spectrum dominated by a specific frequency as the anode becomes increasingly eroded. Even more sensitive than the Fourier transform of the voltage trace is the spectrum of the sound pressure level as obtained with a microphone. For a new anode, two frequency peaks are observed, one coinciding with the frequency of the voltage peak (in the 2–6 kHz range) and another in the 8–10 kHz range, as shown in Fig. 8.42 [Duan et al. (2000)]. As the anode becomes increasingly eroded, the lower frequency peak will shift to lower frequencies and its height increases with respect to the high frequency peak. While such changes in the acoustic spectrum with the erosion of the anode would be somewhat different for other torch nozzle designs, the acoustic spectrum still offers an interesting diagnostic indicator for the anode state.

Such stochastic arc movement gives rise to a complex flow pattern in the discharge cavity as well as in the emerging plasma jet, as illustrated in Fig. 8.43a, for a conventional DC plasma spray torch. The intense and close interaction between the arc column and the plasma forming gas in the discharge cavity results in the rapid heating of the plasma-forming gas and its acceleration through the exit nozzle forming the plasma jet with corresponding plasma jet oscillations, as shown in the high-speed images given in Fig. 8.43b.

Such plasma-jet oscillations are also sensitive to the anode conditions, as can be observed in Fig. 8.44 [Duan et al. (1997)], which shows two high-speed images of a plasma jet obtained with a Laser-Strobe camera (Control Vision) at 100 nm exposure time. Fig. 8.44a shows a typical image of the jet with a new anode, while Fig. 8.44b shows the image of a strongly eroded anode. The jet length is strongly decreased.

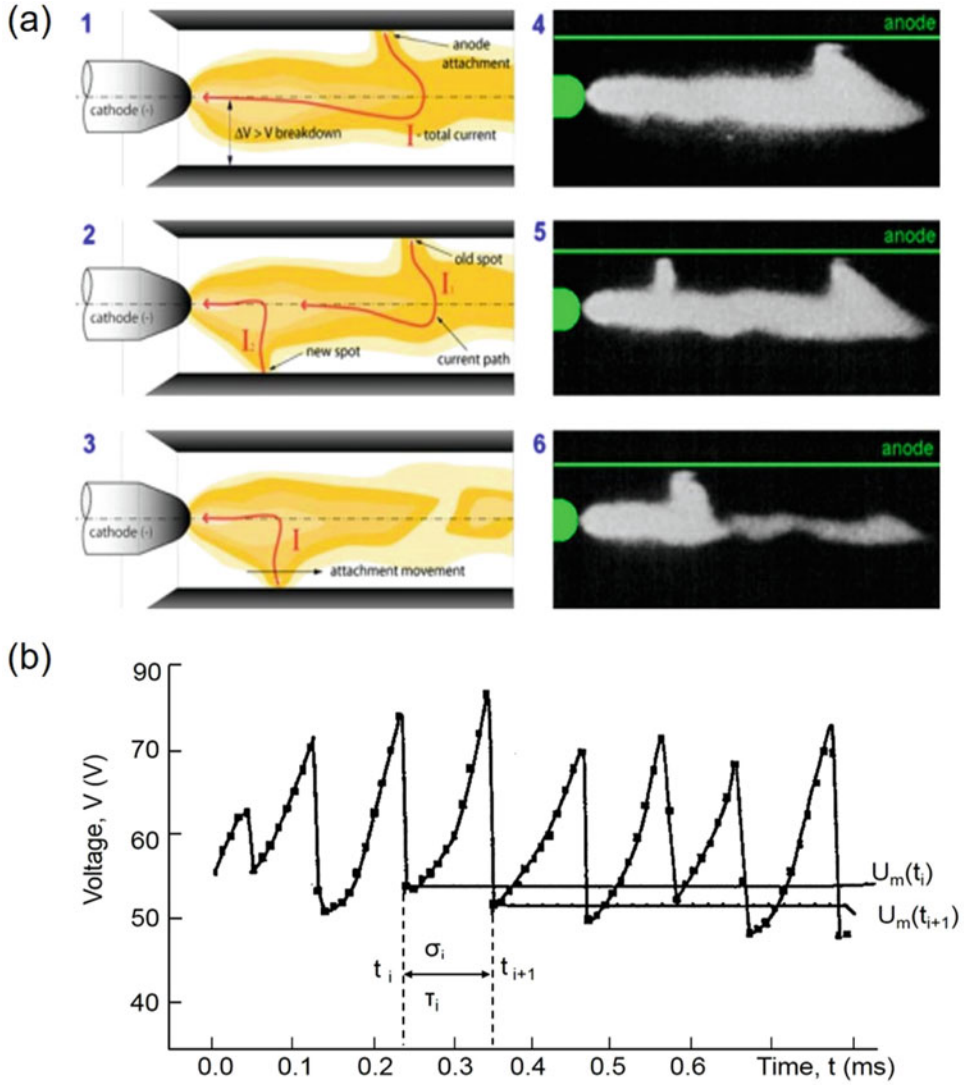

Fig. 8.40 Arc attachment dynamics and associated arc voltage for a DC plasma spray torch of conventional design. (**a**) Schematic of the arc attachment process (left) and supporting experimental high-speed images (right) [Wutzke et al. (1967)], (**b**) reconstruction of the temporal evolution of the arc voltage. [Coudert et al. (1966)].

Since the turn of the century, a systematic effort has been devoted to the dynamic modeling of the arc in the discharge cavity using 3-D, time-dependent, laminar flow simulation involving the numerical solution of the transient continuity, momentum, and energy-conservation equations simultaneously with the electric current and electromagnetic equations [Moreau et al. (2006), Trelles et al. (2006a, b, 2007a, b, c, 2008, 2009, 2011, 2013]. Additional assumption made are:

- gas is treated as incompressible, that is, its Mach number is <0.3,
- gas properties are temperature dependent,
- optically thin plasma in local thermodynamic equilibrium (LTE).

While the assumption of LTE is valid in the arc column, it is questionable in the electrode boundary layers where noticeable deviations from thermal and chemical equilibrium may occur. This was overcome by [Moreau et al. (2006)] assuming an initial high temperature "appendage" between the arc column and the anode wall, often referred to as "arc-root." Upstream restrike was obtained by re-establishing such an arc-root between the main arc column and the anode surface at a location where the electric field at the anode surface exceeds a critical value. This allowed for the reproduction of the different voltage fluctuation modes of steady, takeover, and restrike for an argon-hydrogen arc with the LTE assumption.

A comparable three-dimensional, transient, equilibrium (LTE) model was developed by [Trelles et al. (2006) and Trelles (2006c)] through the solution of the fluid and

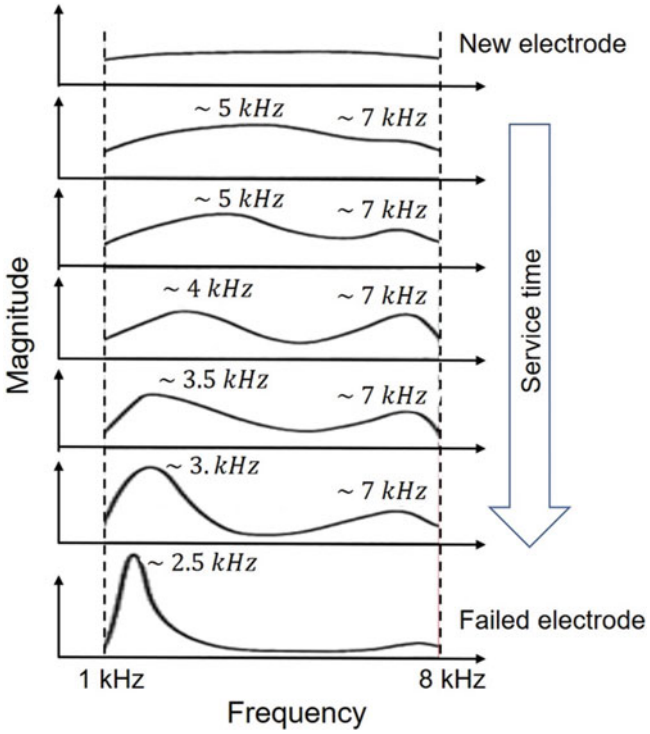

Fig. 8.41 Schematic representation of the Fourier transform power spectrum of the voltage trace of an arc with a new anode (top) to a progressively eroded anode (bottom) showing the increase in the power in the 2–4 kHz range and the shift to a somewhat lower frequency. [Duan et al. (1997)]. (Reprinted with permission of ASM International. All rights reserved)

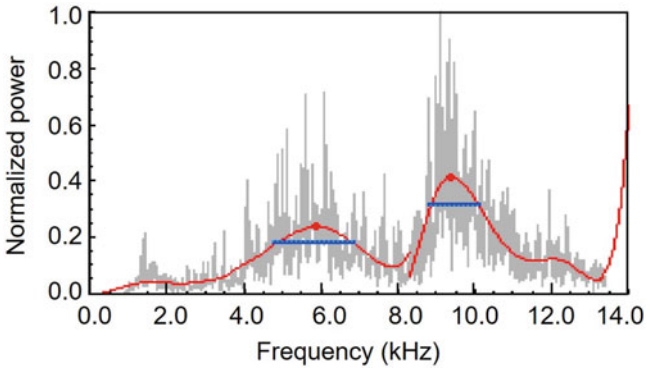

Fig. 8.42 Acoustic spectrum for the Praxair SG 100 torch showing two distinct peaks. The lower frequency peak increases with increasing erosion. [Duan et al. (2000)]. Copyright © ASM International. (Reprinted with permission)

electromagnetic equations in a fully coupled approach by a multiscale finite element method. The model allowed for the prediction of the operation of the torch in steady and take-over modes without any further assumption on the reattachment process, except for the use of an artificially high electrical conductivity region near the electrodes needed because of the equilibrium assumption. Typical results obtained for an

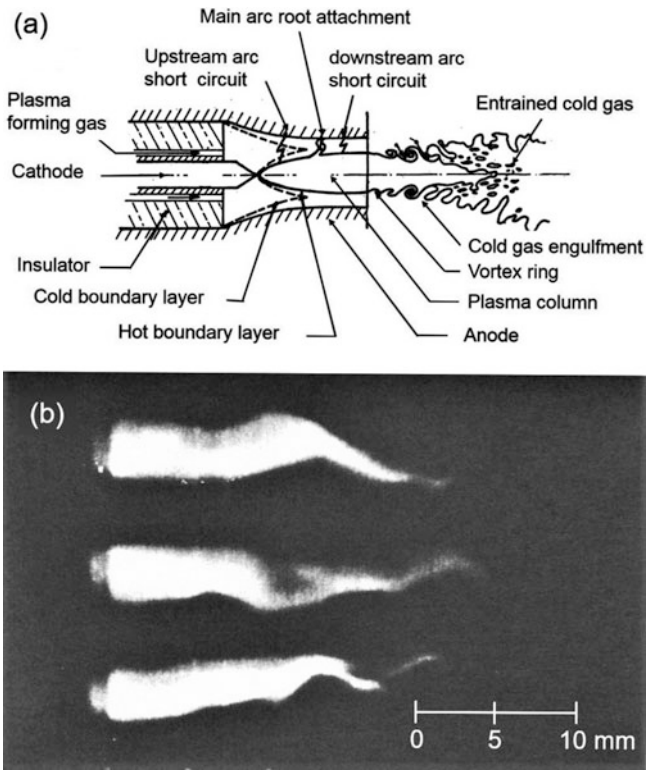

Fig. 8.43 Schematic representation of a conventional DC plasma-spraying torch (**a**) Flow structure [Fauchais and Vardelle (1997)], (**b**) supporting high-speed images (50 ns exposure) of plasma-jet oscillations [Pfender (1999)]

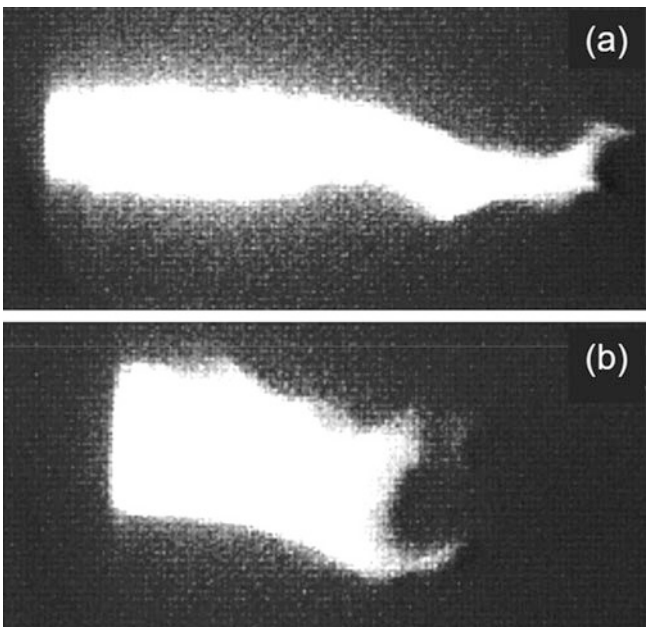

Fig. 8.44 High-speed images (100 ns) of a plasma jet with a new anode (top) and an eroded anode (bottom). [Duan et al. (1997)]. (Reprinted with permission of ASM International. All rights reserved)

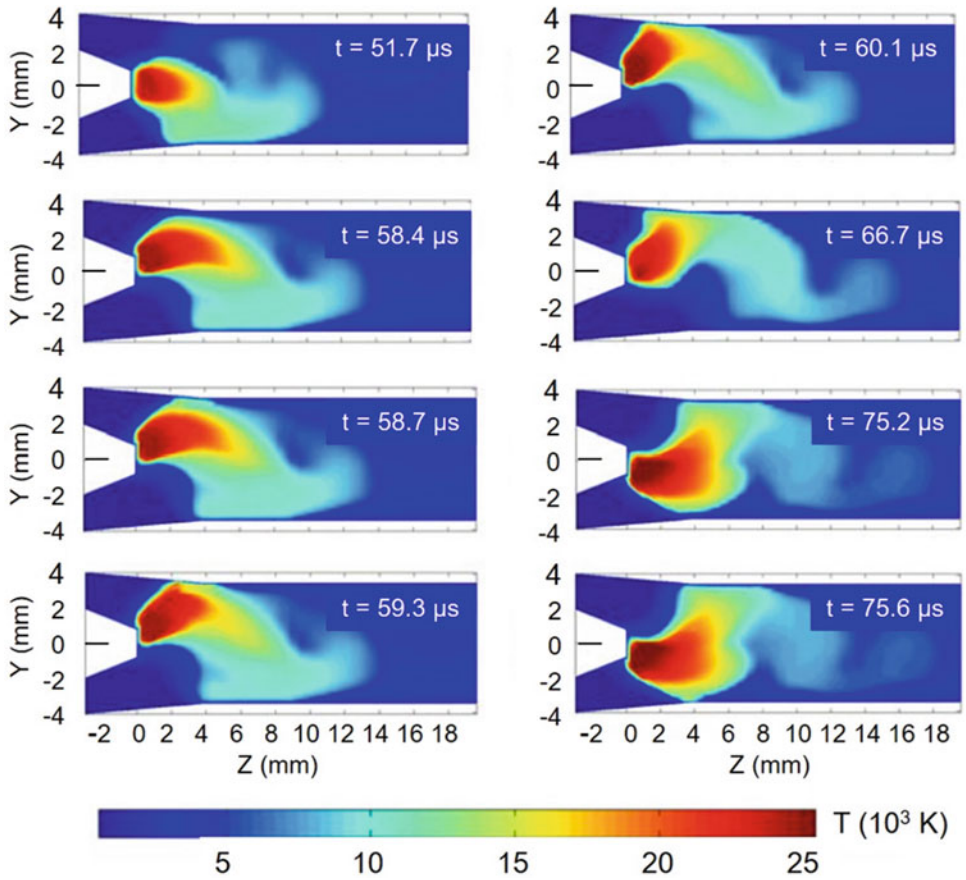

Fig. 8.45 Temperature distribution through a vertical plane during the different time steps of formation of a new arc-root attachment, Ar/H_2 plasma (45 slm Ar +15 slm H_2), 600 A. [Trelles et al. (2006)]

F4-MB torch geometry operating with an arc current of 400A using Ar/H_2 as plasma gas at a flow rate of (45 slm Ar + 15 slm H_2) are given in Fig. 8.45. This shows a time sequence of the reattachment process formed whenever the arc gets "close enough" to the anode. The required proximity being a function of the thickness of the region in front of the anode specified with an artificially high electrical conductivity (∼0.1 mm). The results obtained indicate that the reattachment process in these operating modes may be driven by the movement of the arc rather than by a breakdown-like process used by [Moreau et al. (2006)]. Trelles et al. (2006) reports that for a torch operating in these modes using straight gas injection, the arc reattachment tends to be on the opposite side of its original attachment point due to the imbalance between electromagnetic and fluid drag forces.

The results show that, when straight or swirl injection is used, the arc is dragged by the flow and then jumps to form a new attachment, preferably at the opposite side of the original attachment, as has been observed experimentally. The predicted restrike frequencies, arc length, and anode spot size were in fairly good agreement with experimental values. Arc voltages obtained were, however, too high compared to experimentally observed voltages.

This model was also used to compare the arc movement inside anode nozzles for different torch designs operating with argon-hydrogen or argon-helium mixtures as plasma gas [Trelles et al. (2006), Trelles et al. (2007a)]. Simulations of an F4-MB torch from Sulzer-Metco (presently Oerlikon-Metco) and two configurations of the SG-100 torch from Praxair. A schematic of the attachment scheme proposed by [Trelles et al. (2007a)] for the LTE arc modeling is given in Fig. 8.46. It consists of the following four steps:

(a) arc deflected by incoming flow and location where the breakdown condition is satisfied,
(b) insertion of an electrically conductive channel,
(c) formation of a new attachment,
(d) predominance of the new attachment over the old one.

Non-equilibrium, two-temperature modeling of the DC arc plasma torches was reported by [Trelles et al. (2007b)]. Because of the significant increase in computation load, the model was limited to thermal non-equilibrium, thus neglecting chemical non-equilibrium effects. Computations were carried out for a conventional torch configuration

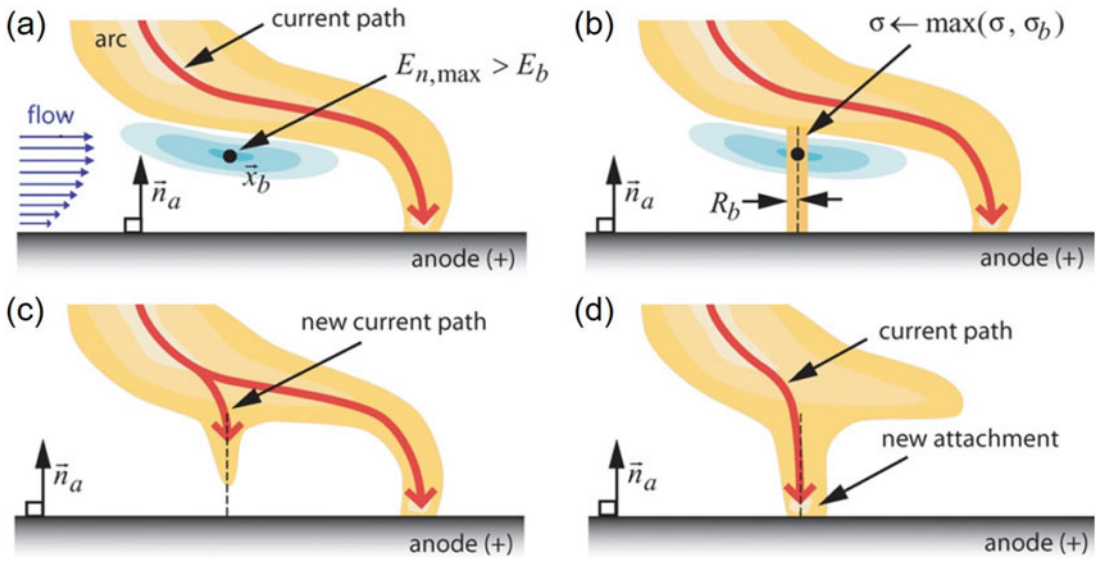

Fig. 8.46 Schematic of the different steps of the reattachment model used in LTE simulation. [Trelles et al. (2007a)]

operating with pure argon as plasma gas (60 slm) with 45° swirl injected, and arc currents of 400 and 800 A. Typical results given in Fig. 8.47 present snapshots in time of the reattachment process for the 400 A arc current case. The temperature distributions given in Fig. 8.47a, b, obtained using the non-equilibrium model (NLTE), are presented, respectively, in terms of the heavy particle temperature, T_h, and electron temperatures, T_e. For comparison, the equivalent results obtained at the same time steps using the equilibrium model (LTE) are given in Fig. 8.46c. The NLTE results show the cathode jet, the movement of the anode column, the formation of a new arc attachment, the small fluctuation of the arc column, and the undulating behavior of the flow as it leaves the torch. It can also be observed how the anode attachment is driven by the net angular momentum over the arc toward the opposite side of the original attachment point. For the conditions studied, a reattachment model was not needed for the NLTE simulation since the formation of a new attachment, as observed by the appearance of a small high temperature "appendage" (see arrows in Fig. 8.47a, b), seems to be driven by high values of the local effective electric field and high values of electron temperature. The reattachment process occurs in this case in a natural manner mimicking the *take-over* and/or *steady* modes of operation. This is not necessarily the case for the *restrike* mode where the use of a reattachment model such as the one used in the LTE simulations (see Fig. 8.46) would be required even in non-equilibrium simulations.

Figure 8.48 shows a time sequence of the dynamics of the arc inside the torch and the plasma jet immerging from the torch nozzle as obtained numerically with an NLTE model, represented by iso-contours of heavy-particle temperature, as well as high-speed images of the plasma jet for the same torch, conventional design with an 8.0 mm nozzle i.d. and closely similar, though not identical, operating conditions. Modeling being done for operation at 400 A, pure argon plasma (60 slm (Ar), with 45° swirl injection with an open discharge in an argon ambient atmosphere, with images given at $\sim$*0.1 ms* interval. The experimental images were taken also at 400 A arc current, for Ar/He plasma (48 slm Ar + 14 slm He) 45° swirl injection, with an open discharge in ambient air with images given at an interval of $\sim$*2 ms*. Both modeling and experimental observations are consistent and in general agreement showing large-scale structures of the plasma jet oscillation that can be traced back to the dynamics of the arc inside the torch, while the fine-scale structures are a consequence of the interaction of the jet with the cold surrounding gas. No turbulence model has been employed in those simulation results.

Further development of DC non-transferred plasma torch modeling was reported by [Trelles (2001, 2013)], linking for the first time the dynamic plasma jet characteristics with the transient arc motion in the discharge and anode nozzle regions. The flow of a plasma jet produced by a non-transferred arc DC plasma torch impinging on a flat substrate is simulated using a fully coupled thermodynamic non-equilibrium (two-temperature) model. For simplicity, the chemical equilibrium assumption was maintained. The modeling results indicate that the dynamics of the arc inside the torch cause the quasi-periodic movement of the jet, which leads to the formation of complex patterns in the heavy-species and electron temperature distributions, together with significant deviations from thermodynamic equilibrium, near the substrate. It is observed that the evolution of the degree of non-equilibrium near the substrate is strongly correlated with the direction of movement of the jet and, hence, with the arc

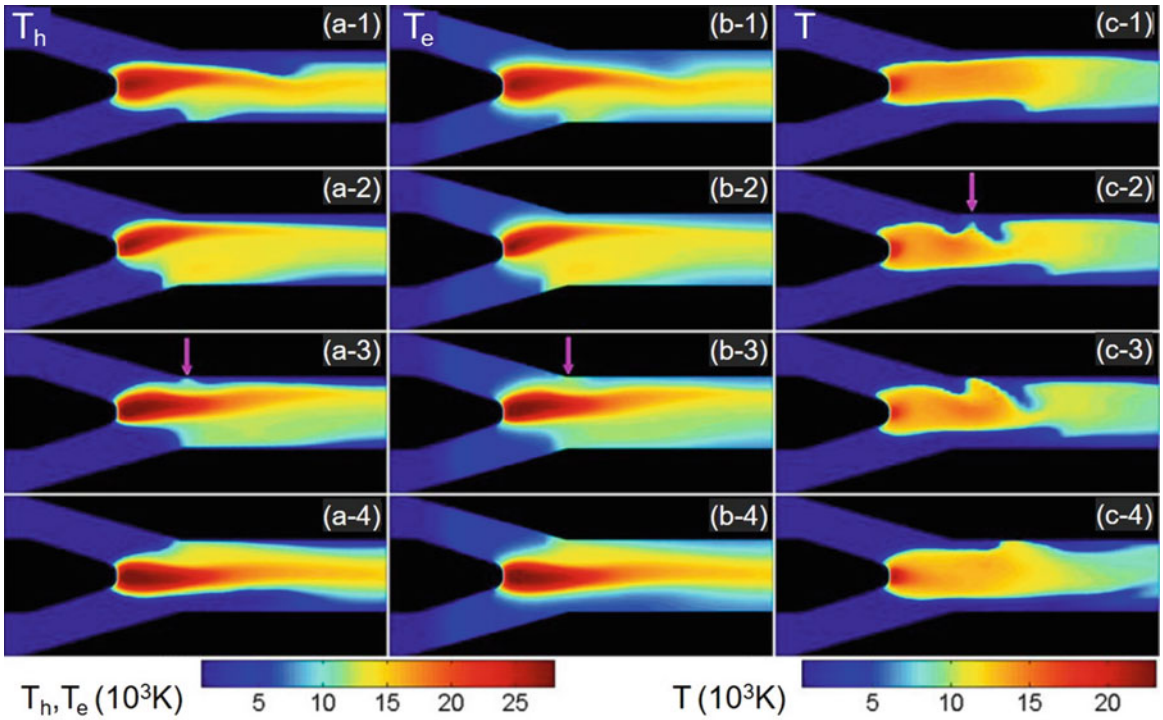

Fig. 8.47 Temperature fields inside the torch during the reattachment process for a DC arc plasma torch, 8 mm nozzle i.d., 60 slm (Ar) 45° swirl injection, and 400 A obtained using NLTE model (**a**) heavy-particle, (**b**) electron temperatures and LTE model, and (**c**) equilibrium temperature. The arrows indicate the location where the new attachment starts forming. [Trelles et al. (2007b]

dynamics inside the torch. Simulation results also uncover distinct aspects of the flow dynamics, including the jet forcing due to the movement of the electric arc, the prevalence of deviations between heavy-species and electron temperatures in the plasma fringes, the development of shear-flow instabilities around the jet, the occurrence of localized regions with high electric fields far from the arc, and the formation and evolution of coherent flow structures.

Typical results given in Fig. 8.49 depict the difference between the heavy-species and the electron temperature fields during an arc attachment event. The time instants corresponding to the snapshots are indicated. According to Trelles (2013), comparing the location of the anode attachment and the curvature of the jet in Fig. 8.49a, b-1 with those of Fig. 8.49a, b-4, it is possible to notice a correlation between the dynamics of the arc inside the torch and the large-scale structure of the plasma jet. Trelles (2013) also proposes that the turbulent nature of the plasma jet could be linked to shear flow instabilities (also known as Kelvin–Helmholtz) near the torch exit, as shown by the sequence of snapshots given in Fig. 8.50, which were obtained at time sequels indicated in the figure. It is underlined, however, that the inherently sensitive nature of instability development phenomena makes imperative the use of high-accuracy numerical simulations, which was not the case in this study. By contrasting the results in Fig.8.49 with those in Fig. 8.50, it is observed that the shear-flow instabilities are correlated with the distribution of T_h and not with the distribution of T_e.

8.4.2 Ambient Gas Entrainment by the Plasma Jet

The unsteady nature of the plasma jet has been the subject of numerous studies [Spores and Pfender (1989), Spores et al. (1990), Pfender et al. (1990), Spores et al. (1990), Fincke and Swank (1991), Coudert et al. (1995), Planche et al. (1997), Duan et al. (1999a, b), Duan and Heberlein (2000, 2002), Gregori et al. (2003), Bisson et al. (2003), Bisson and Moreau (2003), Nogues et al. (2007), Coudert et al. (2007), Coudert and Rat (2008)]. There are two primary causes for this unsteady behavior:

- the constant movement of the arc root, resulting in voltage and power fluctuations and strong temporal variations of the jet temperature and velocity distributions, and,
- the extreme density and viscosity gradients between the low-density, high-viscosity plasma jet and the cold gas surroundings [Pfender et al. (1990)].

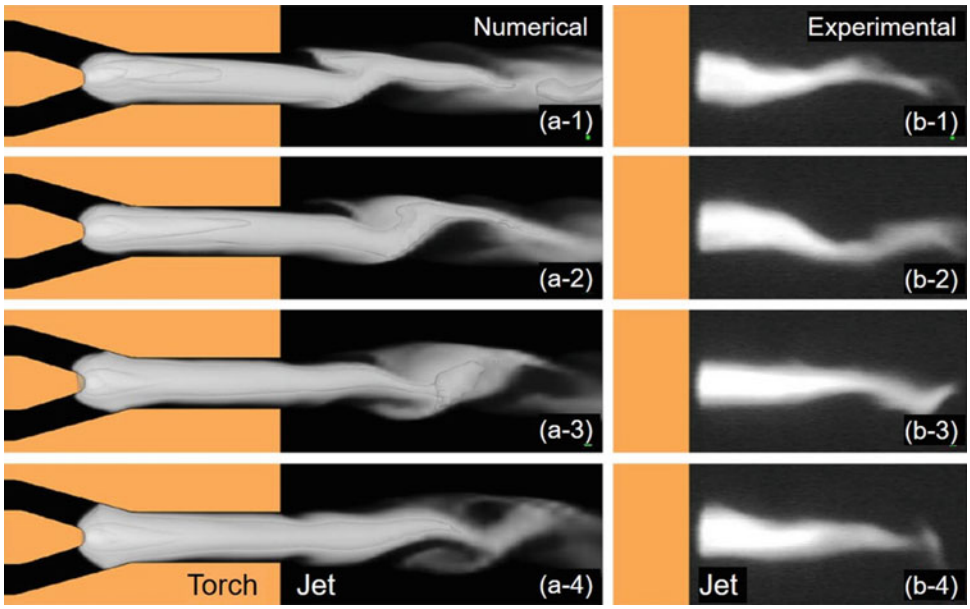

Fig. 8.48 Arc and plasma jet dynamics for an 8 mm i.d. torch nozzle operated at 400 A (**a**) sequence of heavy-particle temperature distributions obtained using an NLTE model, pure argon plasma gas 60 slm (Ar) 45° swirl injection, with ~100 μs time interval between frames (Numerical) and (**b**) experimental highspeed images, plasma gas (48 slm Ar + 14 slm He) 45° swirl injection, ~2 ms time interval between frames (Experimental). [Trelles et al. (2008)]

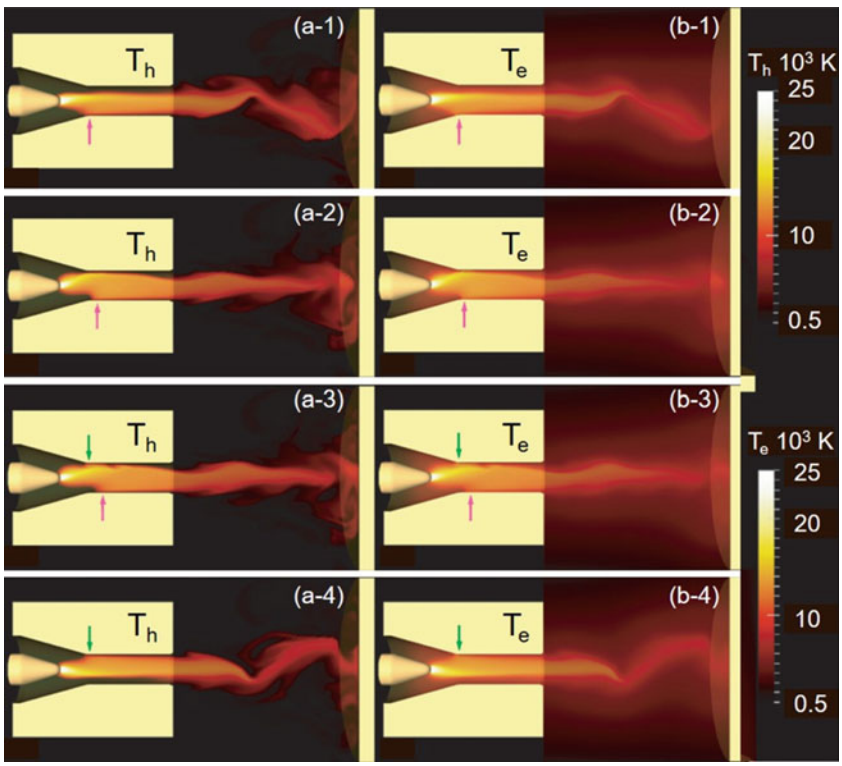

Fig. 8.49 Temperature dynamics during an arc reattachment event (**a**) T_h and (**b**) T_e; sequence 1 to 4, respectively, at 1.16, 1.29, 1.31, and 1.41 ms. [Trelles (2013)]

These give rise to intense plasma jet fluctuations shown in the series of high-speed images given in Fig. 8.43 [Pfender (1999)], Fig. 8.44 [Duan et al. (1997)], and Fig. 8.48 [Trelles et al. (2008)]. As schematically illustrated in Fig. 8.51a [Pfender et al. (1990)], a rather complex flow pattern develops rapidly around the plasma jet as it exits the plasma

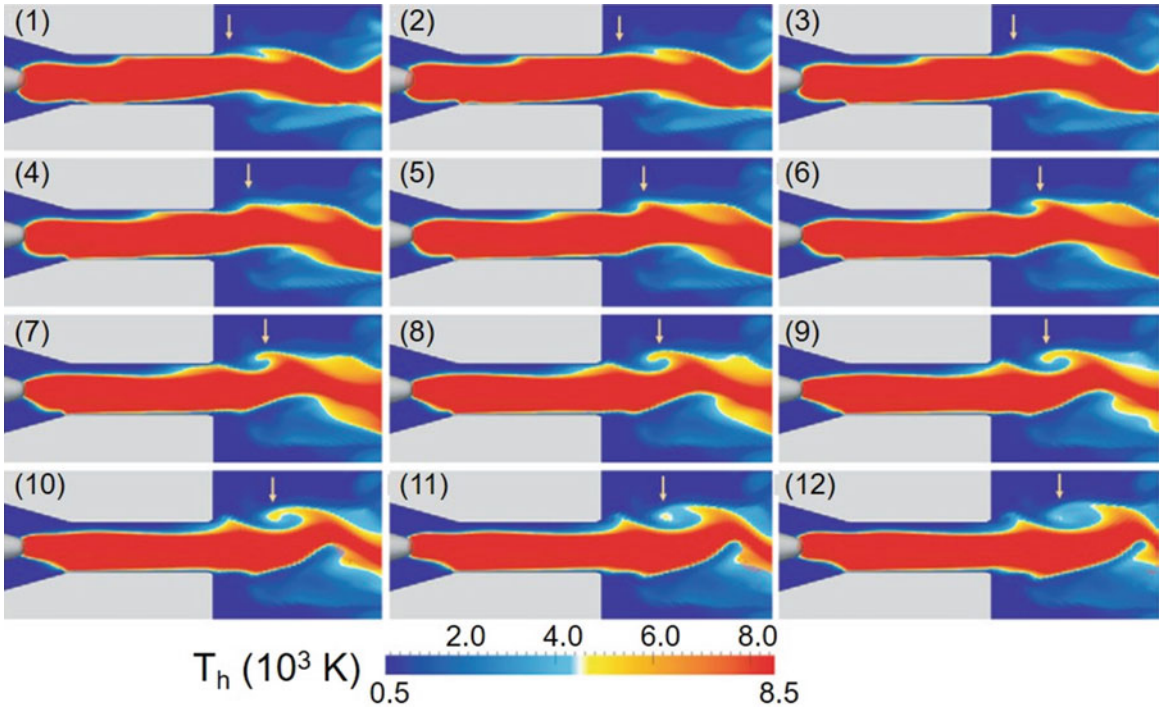

Fig. 9.50 Formation and development of shear-flow instabilities: sequence of snapshots of T_h distribution in the region encompassing the cathode tip and the torch discharge. The arrows indicate the location where an instability develops. The color scale used emphasizes the development of the instabilities. [Trelles (2013)]

torch nozzle and penetrates the ambient gas. The large velocity difference between the plasma jet and the ambient gas causes the rolling up of the flow around the nozzle exit into a ring vortex, which is pulled downstream by the flow, allowing the process to repeat itself again at the nozzle exit. Adjacently formed vortex rings at the outer edge of these vortices then lead to wave instabilities growing around the entire ring. Next, the distorted vortex rings start entangling themselves with adjacent rings, finally resulting in a total breakdown of the vortex structure into large-scale eddies and the onset of turbulent flow. This entanglement process of adjacent unstable vortices results in the first large-scale engulfment of the ambient gas, although some entrainment also takes place during the roll-up process of the jet's shear layer. These large eddies of cold gas that are entrained have a much higher density and thus greater inertia than their high-temperature counterparts. The eddies of cold gas travel in the axial direction at much lower velocity, while the hot plasma gas essentially accelerates around and stagnates on the cold gas eddies with little initial mixing. All eddies in the flow are continually breaking down into smaller and smaller eddies, while diffusion is taking place on the molecular level at all eddy boundaries. The mixing and diffusion process eventually reaches the centerline of the jet, foretelling the end of the laminar core. The jet now undergoes transition and eventually becomes fully turbulent, while eddies of external gas continue to be engulfed and then absorbed into the main jet along its entire length, further reducing both the mean temperature and velocity.

This qualitative description of turbulence development and cold gas entrainment is corroborated by the pulsed-laser Schlieren photograph (exposure time 10 ns) of argon DC plasma jet given in Fig. 8.51b after [Finke et al. (2003)], obtained for an SG-100 plasma torch with a nozzle i.d. of 8.0 mm operated using pure argon as plasma gas (35.4 slm), 900 A and 15.4 V arc current and voltage, respectively. Based on measurements of temperature and velocity, the centerline Mach number at the torch axis is ~0.49.

Further corroboration of the intense mixing between the plasma jet and the ambient atmosphere is given in Fig. 8.52, after [Pfender et al. (1991)], showing 2-D isocontours of relative nitrogen concentration in DC plasma jet, 12.7 mm nozzle id, operated using pure argon as plasma gas (9.8 slm), and arc currents of 250 and 500 A, with a corresponding torch power of 5 and 10 kW, respectively. The data given in this figure were obtained using CARS, which is a nonintrusive diagnostic technique capable of measuring nitrogen molecular concentrations which are given in this figure normalized to the number density of N_2 at ambient conditions ($No \approx 1.7\ 10^{19}\ cm^{-3}$). The rapid entrainment of air into the core flow of the jet, coincident with the onset of turbulence and jet breakup, is evident in the concentration contours. It is interesting to note that even though the onset of turbulence occurs earlier in the 5 kW case, a laminar, all-argon core

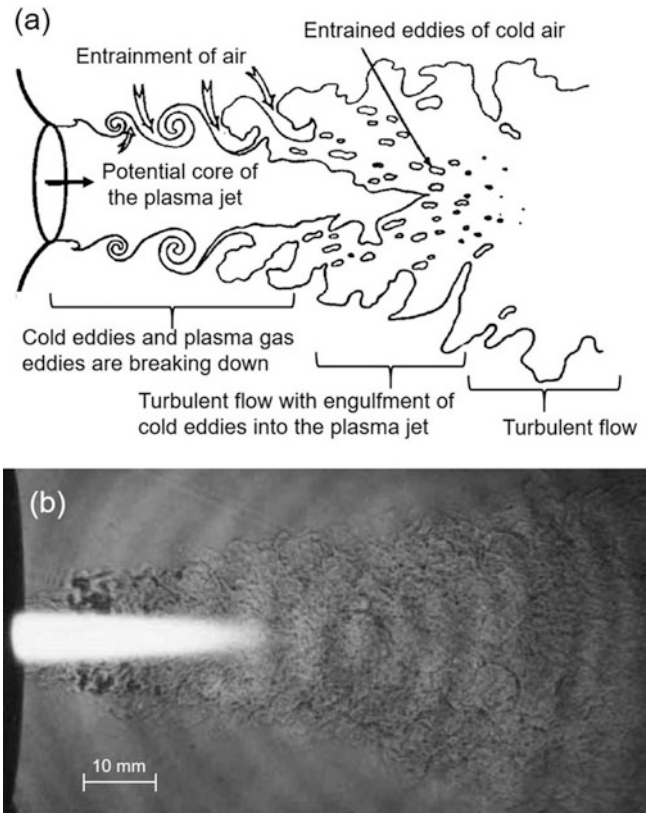

Fig. 8.51 Schematic of the large-scale turbulence and cold gas entrainment in a DC plasma jet issuing into a cold gas environment [Pfender et al. (1990)] and pulsed-laser Schlieren images of a turbulent Ar plasma jet, SG-100 torch, 8 mm nozzle id, 35.4slm, 900 A. 15.4 V. [Finke et al. (2003)] (Reprinted with permission of ASM International. All rights reserved)

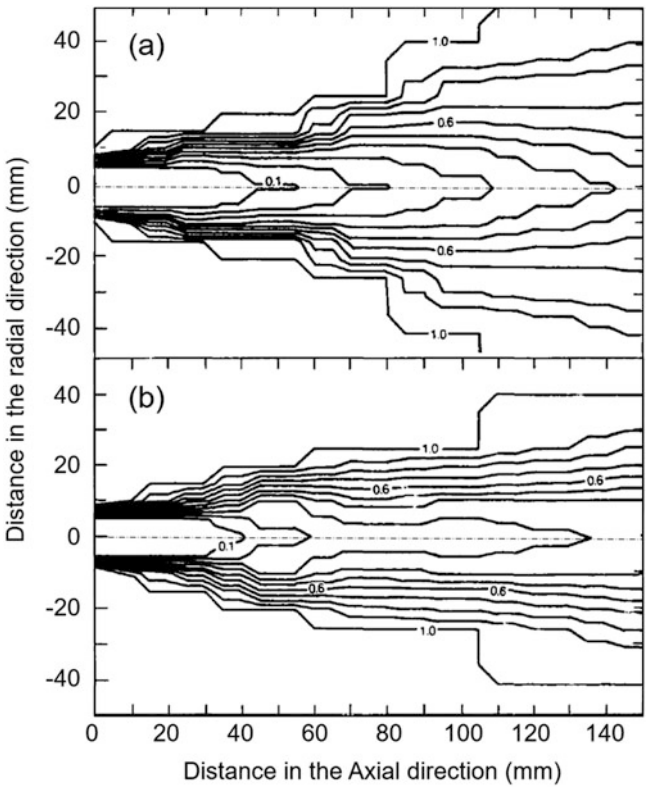

Fig. 8.52 Contours of nitrogen entrained from an ambient air atmosphere into a pure-argon DC plasma jet 9.8 slm (Ar). Values give are normalized to the number density of N_2 at ambient conditions, (**a**) 250 A, 5 kW, (**b**) 500 A, 10 kW. [Pfender et al. (1991)]

appears to persist for approximately the same distance in both cases, and initially the mixing rates are comparable. Farther downstream, the lower power 5 kW case spreads more rapidly and entrains air at a greater rate.

Measurement of the amount of air entrained in an argon plasma jet issuing into an air environment, using gas sampling with enthalpy probes, showed that at an axial location 20 mm downstream from the nozzle exit, 50% of the gas consisted of air [Pfender et al. (1990)]. Furthermore, in a set of definitive experiments using enthalpy probe measurements, two-photon Laser-Induced Fluorescence and CARS, the entrainment of air into an argon plasma jet was demonstrated, and the CARS measurements showed that the entrained oxygen remains at a low temperature of about 2000 K [Finke et al. (2003)]. Fig. 8.53 shows for the plasma torch and operating conditions used for Fig. 8.51b, the axial temperature decay measured with an enthalpy probe, the fraction of the air in the gas sample obtained with the enthalpy probe, and the temperature of the entrained oxygen derived from CARS measurements of the rotational–vibrational level populations of molecular oxygen. The results clearly indicate the significant difference in temperatures between the plasma jet and the entrained air, as confirmed by numerical simulations results [Williamson et al. (2003)]. Corresponding radial profiles of the measured plasma axial velocity, temperature, and entrained air concentration profiles at different distances downstream from the nozzle exit level of the torch are given in Fig. 8.54.

Figure 8.55a [Gregori et al. (2003)] shows 100 measured values of peak temperatures in an atmospheric-pressure argon plasma jet (35 slm) at an axial location 11 mm from the nozzle exit, derived from spectroscopic measurements of an absolute line intensity with a time resolution of 50 μs. The strong variation in this peak temperature (± 2000 K) is evident. However, what is even more interesting is the radial position at which this peak temperature has been measured (see Fig. 8.55b), ranging from the axis to a position 3 mm from the axis for a nozzle radius, $r_o = 4$ mm [Gregori et al. (2003)]. Clearly, the nice axisymmetric distributions obtained with measurements over a time scale of seconds cannot be assumed when processes are considered at or below the millisecond time scale.

As described earlier, the mixing of the ambient air with the plasma jet flow cools it down rather rapidly, mainly due to oxygen dissociation starting at 3000 K. To delay this entrainment effect, the mixing with the ambient gas, and the cooling of the plasma, it is possible to use an anode

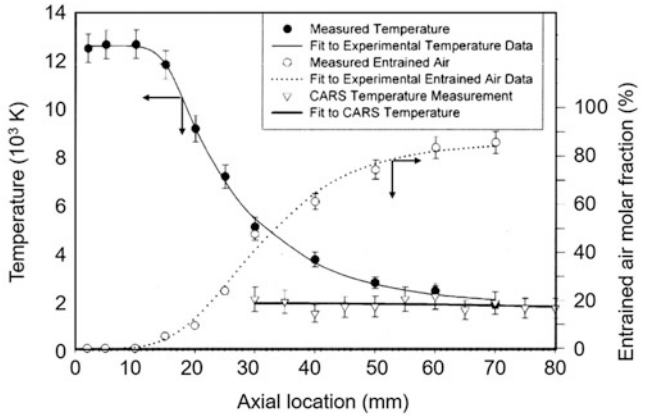

Fig. 8.53 Axial distributions of enthalpy-probe measurements of plasma temperatures, volume fraction of entrained air in the plasma jet, and CARS-temperatures of the entrained oxygen showing the low temperatures of the entrained oxygen. [Finke et al. (2003)]. (Reproduced with kind permission of Elsevier)

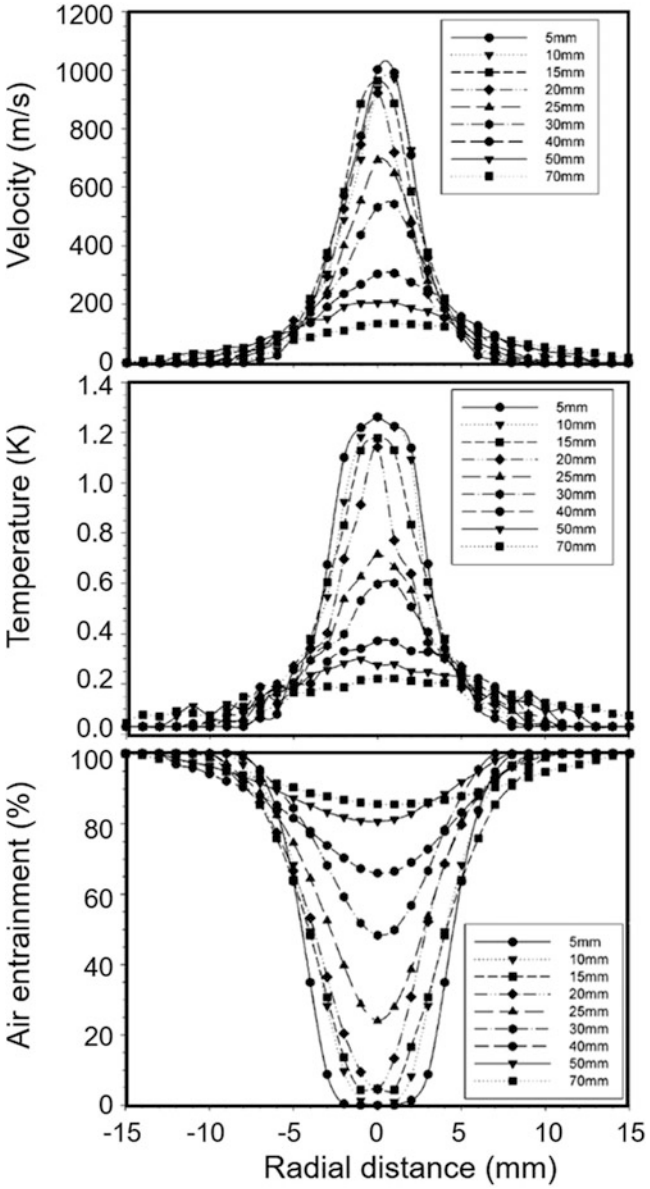

Fig. 8.54 Enthalpy probe measurements of the radial profiles (**a**) axial velocity, (**b**) temperature, and (**c**) entrained air mole fraction, for a pure-argon DC plasma jet SG-100, 8.0 mm nozzle id, 35.4 slm (Ar), 900 A, 15.4 V in an open discharge in ambient air. Distance in legend are axial location measured from the face of the torch. [Finke et al. (2003)]. (Reproduced with kind permission of Elsevier)

nozzle extension with the same diameter as that of the nozzle. Such an approach, generally called "solid shroud," has been proven to be effective in delaying the contact of the plasma gas with the ambient atmosphere with limited loss in terms of plasma energy (generally of the order of 10 to 15%) to the wall of the extension tube. According to [Roumilhac (1990)], the plasma jet core exiting the anode nozzle extension had almost the same length as that of the jet core without the anode nozzle extension. Another important feature of these extensions is that, even with the power lost to cool the extension, the temperatures and velocities of the jet are not significantly reduced at the extension exit. [Betoule (1994)] reported that a DC plasma torch with an anode nozzle i.d. of 7 mm working with an Ar–H_2 mixture (45–15 slm) and an arc current of 600 A corresponding to 40 kW, has measured 2 mm downstream of the nozzle exit on the torch axis a gas temperature of 13,000 K and a velocity of 2000 m/s. 52 mm downstream on the torch axis, the temperature was 6200 K and the velocity was about 500 m/s. With an insertion of a 50 mm long nozzle extension of the same i.d., the temperature was 11,000 K and the velocity 1700 m/s due to 5.7 kW lost in the extension cooling. Unfortunately, these nozzle extensions are difficult to use with powder radially injected in the anode nozzle downstream of the arc root, due to their divergent trajectories. However, such extensions can be used with axial injection torches, where the particle jet divergence is much less than for radial powder injection. In this case, at the exit of the extension, particles reach high velocities, especially for submicron- or nano-sized particles which, in spite of the Knudsen effect, reach velocities between 500 and 700 m/s. Extensions that have a divergent shape and are rather long (about 100 mm) have also been used for spraying. The main problem is again the tendency of the fully molten particles to stick to the inner wall of the solid shroud. To avoid that, the total angle of the divergent shape must have a value between 40 and 50°. While this configuration reduces plasma losses to the shroud wall, boundary layer separation gives rise to recirculating flow and the entrainment of ambient air in the shroud space, which defeats its purpose.

Fluid dynamic shrouds, without nozzle extension, provide a curtain of an inert gas between the plasma jet and the surrounding atmosphere. The problem with such shrouds is

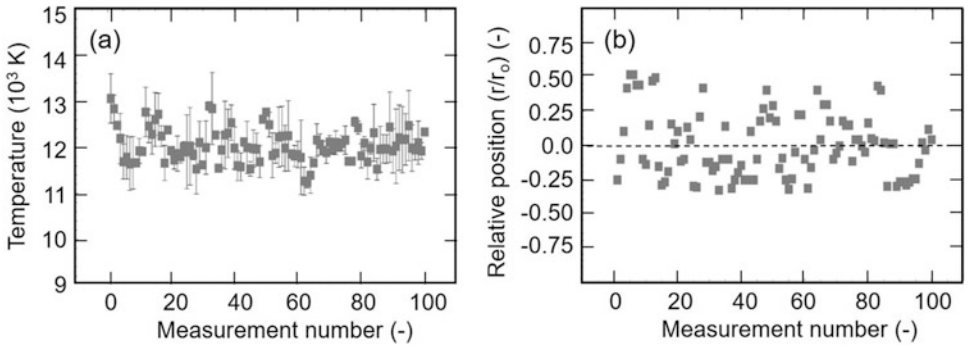

Fig. 8.55 Consecutive measurements of the peak temperature and its location relative to the torch axis for a pure-argon (35 slm) DC plasma jet, 600 A in an atmospheric pressure open-air discharge at an axial position 11 mm from the nozzle exit. Time resolution of the measurement 50 μs, 5 Hz repetition rate (**a**) peak temperature (**b**) relative distance to the torch axis (r/Ro), where Ro is the nozzle radius. [Gregori et al. (2003)]. (Reproduced with kind permission of IPCS)

that the amount of gas in the shroud has to be rather large to match the boundary layer velocity because of the relatively large cross-sectional area. With a shroud where argon gas was injected parallel to the flow of the plasma jet through a ring-shaped slit surrounding the jet, it was possible to spray reactive metal particles in an air environment with minimal oxidation. The amount of shroud gas was varied from 100% to 300% of the plasma gas flow rate, and at 300% shroud mass gas flow, the oxygen fraction at the center of the jet was less than 0.5% at a standoff distance of 85 mm. The appropriate selection of the distance between the nozzle wall and the ring-shaped slot was crucial for the success [Mohanty et al. (1996)].

A similar approach has been taken with an axial injection torch (Axial III from Northwest Mettech, Canada) in a spray process depositing a Hastelloy bond coat [Burgess (2002)]. The oxidation of the particles was minimized by using a double shroud with a total gas flow rate of 300 slm for a plasma gas flow rate of 240 slm (75% Ar, 15% H_2, 10% N_2). An inner argon-gas shroud surrounded the plasma jet as it exited the nozzle, and an outer shroud of nitrogen was introduced further downstream at the end of a cylindrical guide tube for the inner shroud.

In a somewhat modified approach, an anode nozzle was modified at its downstream end by fitting a porous ring surrounding the original copper nozzle wall [Malmberg et al. (1995), Chen et al. (1996)]. One of the two powder feed channels of an SG-100 torch was used to provide the shroud gas (see Fig. 8.56) [Chen et al. (1996)]. In some experiments, this shroud was complemented by injecting part of the gas tangentially between the point of the arc attachment and the powder injection point to provide a swirl component opposing the swirl of the plasma gas. The results showed that the particle fluxes were more confined to the central hot core part of the jet. The coatings showed lower porosity and higher deposition efficiencies. The amount of shroud gas in this case did not exceed the plasma gas flow.

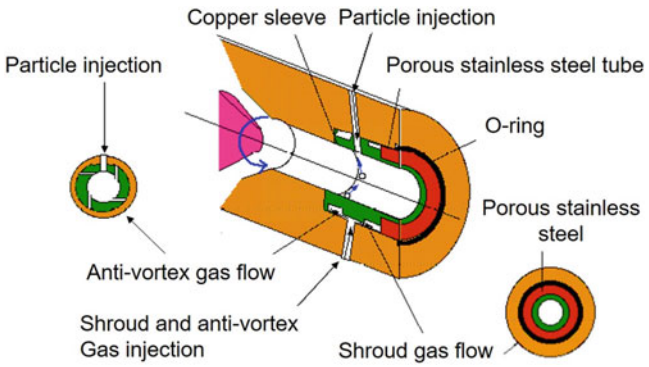

Fig. 8.56 Schematic of modification to SG-100 anode with porous ring shroud and counter swirl. [Chen et al. (1996)]. (Reprinted with permission of ASM International. All rights reserved)

8.4.3 Plasma Jet Characteristics

8.4.3.1 Plasma Torch Operating Parameters

Most DC plasma torches operate in a current control mode, that is, the current is kept constant through a feedback control loop in the power supply which compensates by changing the voltage in order to maintain the current at the required set value. The current set point and the plasma gas flow rate and composition are the independent parameters and are chosen by the operator. A specific plasma torch is then characterized by the time-averaged arc voltage, its standard deviation, and the cooling water temperature rise, and these two quantities allow for the determination of the torch operation, its energy efficiency, and the power carried into the plasma jet, as well as the average specific enthalpy of the plasma gas, its average temperature, and velocity. The typical voltage–current diagram for a DC plasma torch of conventional design operating at atmospheric pressure using Ar/H_2 (45 slm Ar + 15 slm H_2) as plasma gas is given in Fig. 8.57. This shows a strong dependence of the arc voltage on the mode of plasma gas injection into the discharge cavity, with axial injection giving rise to the

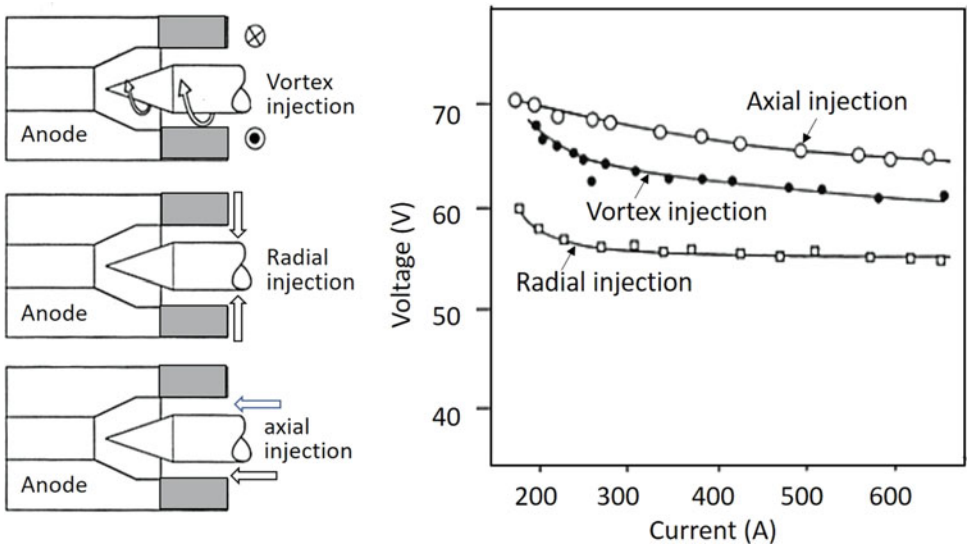

Fig. 8.57 Arc voltages as a function of arc current for Ar/H_2 plasma using three different plasma gas injection modes. [Roumilhac (1990]. (Courtesy of P. Roumilhac)

highest voltages, corresponding to the longest arc length, with vortex and radial injection modes giving rise to shorter arc lengths and successively lower voltages. In all three cases, the arc voltage drops gradually with the increase in the arc current.

The corresponding variation in the arc voltage [Roumilhac et al. (1990a, b)] and energy efficiency [Roumilhac (1990a, b)] plasma torch with increase in the molar fraction of the secondary gas (H2 or He) are given in Fig. 8.58. These were obtained for a DC torch of conventional design using an axial injection of the plasma gas and arc current of 600 A. The addition of a secondary gas such as hydrogen or helium to the argon plasma gas has visibly a strong influence on the arc voltage and torch efficiency. A small addition of hydrogen in concentrations of the order of 10 to 20 vol.%, leads to a significant increase in the arc voltage and torch efficiency. This is mostly caused by the increased thermal conductivity of the arc column due to the fast diffusion of the smaller hydrogen atoms to its fringes. The resultant local cooling effect in the fringes of the arc column will cause a severe constriction of the arc and an increase in the arc voltage. The higher efficiency can be explained by the fact that for a given arc current, the anode root heat losses, which are primarily determined by the arc current, remain constant, while the arc voltage and arc power increase significantly with the introduction of the secondary gas. Energy losses to the anode will accordingly represent a smaller fraction of the total arc power, which combined with the reduced radiation losses from the arc smaller arc column diameter will give rise to an increase of the overall energy efficiency of the torch.

8.4.3.2 Velocity and Temperature Fields

The plasma jet can be characterized by several diagnostic methods. Emission spectroscopy, enthalpy probes, and laser scattering can yield the distribution of temperature and electron density in the jet, and laser Doppler anemometry will allow for the determination of the velocity distributions [Vardelle et al. (1982)].

Figure 8.59 [Coudert et al. (1995)] shows the radial velocity distribution of an argon jet 5 mm from the nozzle exit and that of an argon arc with 20 vol.% hydrogen addition, for approximately the same current but considerably higher gas flow rate. A small addition of hydrogen causes the jet to be severely constricted and more than doubles the peak velocity. It should be noted that the effect on temperature is much less because the high specific heat of hydrogen reduces the temperature.

Figures 60 and 8.61 [Vardelle et al. (1982)] give, respectively, examples of the temperature and velocity distributions in the jet of a plasma spray torch in an open discharge in ambient air operating with a mixture of N_2/H_2 or Ar/H_2 as plasma gases. These were obtained for a DC plasma torch of conventional design with the following nozzle dimensions and operating conditions:

- for the N_2/H_2 case, Fig. 8.60 shows an exit nozzle i.d. of 6.0 mm with a length of the cylindrical channel 26 mm, plasma gas flow rate (37 slm N_2 + 27 slm H_2), DC power 29 kW,
- for the Ar/H_2 case, Fig. 8.61 shows an exit nozzle i.d. of 8.0 mm with a length of the cylindrical channel 22 mm, plasma gas flow rate (75 slm Ar +37 slm H_2), DC power 29 kW.

Measurements were carried out using emission spectroscopy for the 2-D temperature fields, and laser Doppler anemometry for the velocity fields which required that the flow be seeded by small particles, which are assumed to

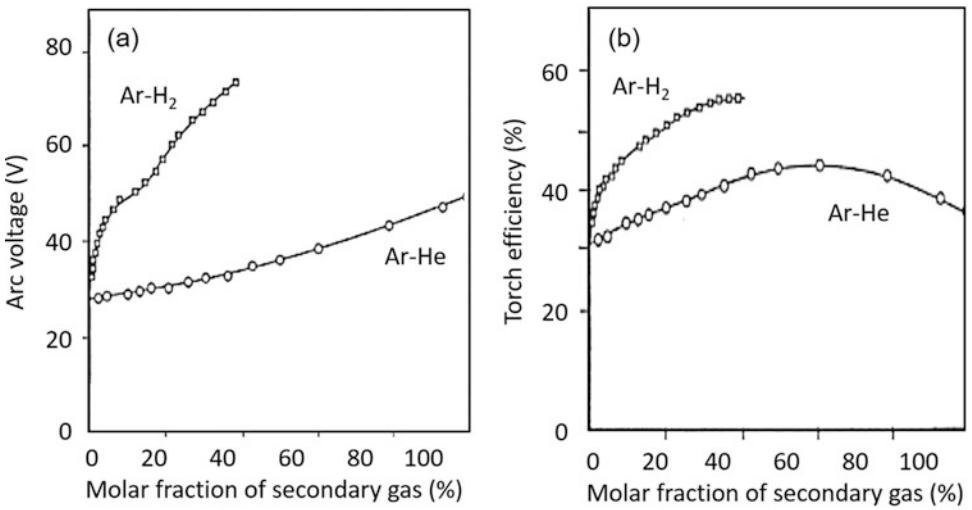

Fig. 8.58 Effect of secondary gas concentration (vol%) at constant arc current, 600 A, on the (**a**) Arc voltage and (**b**) torch energy efficiency, for a conventional DC plasma torch. [Roumilhac et al. (1990a, b)]. (Reprinted with permission of ASM International. Courtesy of P. Roumilhac)

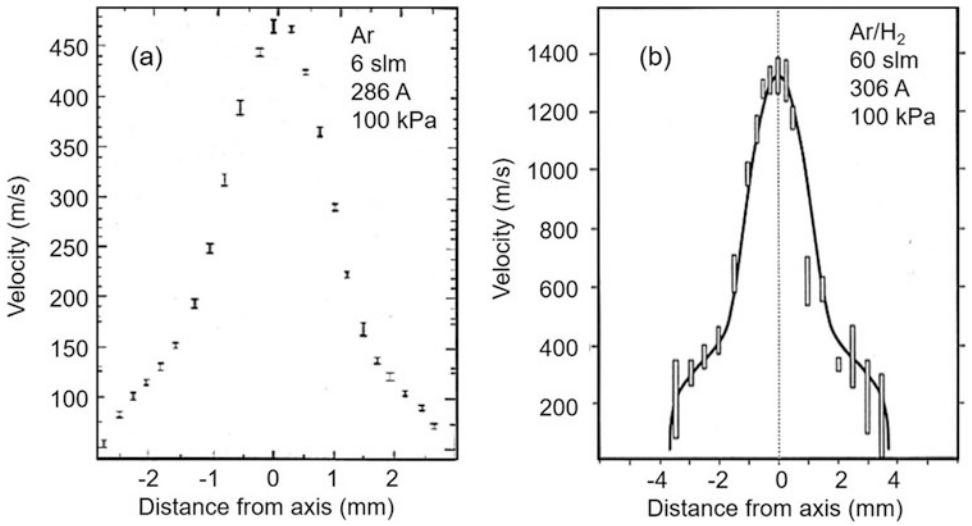

Fig. 8.59 Effect of plasma gas composition on the radial profiles of the axial plasma velocity for (**a**) a pure argon jet with 6 slm at 286 A and (**b**) an Ar/H_2 (20 vol.% H_2) jet with 60 slm at 306 A. [Coudert et al. (1995)]. (With kind permission from Springer Science+Business Media B.V)

follow the flow field. In both cases, Fig. 8.60a and Fig. 8.61a, the plasma jet can be divided into three regions. The core region is the one in which the plasma temperature is relatively constant, 12,000–12,500 K, extending to about 10 to 12 mm from the torch nozzle. This is followed by a transition region in which the plasma temperature falls rapidly to less than 3000 K at 100 mm from the nozzle exit. In the last region, the gas temperature drops gradually as the gas is mixed with the entrained ambient air. The radial temperature profiles are particularly steep over the core region. The presence of such steep temperature gradients explains the problem of the thermal treatment of the particles in a DC plasma jet, which requires very close control of the particle injection conditions into the plasma.

In Fig. 8.60b, the axial velocity isocontours are shown for the N_2/H_2 case. Beyond the core region, the plasma velocity drops rapidly with increase in distance from the torch nozzle. Similar results at the same power level of 29 kW are represented in Fig. 8.61b for an Ar/H_2 mixture. It can be seen that the diameter of this jet is greater than the one of N_2/H_2 (due to the increase in the nozzle diameter) and that the core and plume of the jet are also longer (for the core, about 30 mm for N_2/H_2 and 50 mm for Ar/H_2 on the axis). The velocities in the N_2/H_2 jet are higher

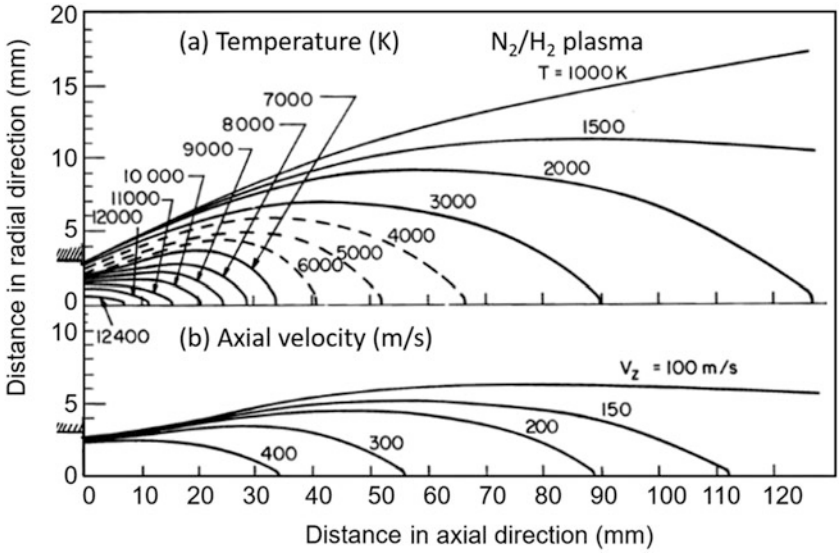

Fig. 8.60 (**a**) Temperature (**b**) axial velocity isocontours for an N_2/H_2 DC plasma jet (37 slm N_2 + 27 slm H_2), power 29 kW, [Vardelle et al (1982)]. (With kind permission from Springer Science Business Media B.V.)

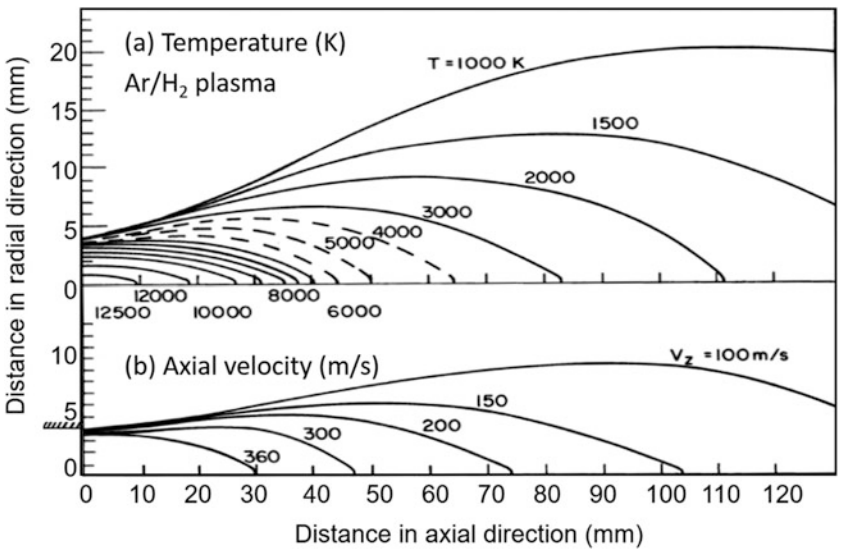

Fig. 8.61 (**a**)Temperature (**b**) axial velocity isocontours for an Ar/H_2 DC plasma jet (75 slm Ar + 37 slm H_2), power 29 kW. [Vardelle et al (1982)]. (With kind permission from Springer Science Business Media B.V.)

than the ones in the Ar/H_2 jet, a phenomenon due probably to the lower viscosity of the N_2/H_2 mixture and to the smallest nozzle diameter used in the N_2/H_2.

The design of the anode nozzle and the mode of gas injection of the plasma gas into the discharge cavity affect the length of the arc and consequently arc stability, power loss to the cooling water, and the temperature and velocity distributions in the plasma jet. Numerous nozzle designs have been proposed and tested, allowing for the control of the plasma jet temperature and velocity distributions, as function of the operating parameters [Rahman et al. (1998)]. An example of the impact of small changes in the nozzle design, such as a slight divergence of the nozzle downstream of the arc attachment, on the temperature distributions in the plasma jet is given in Fig. 8.62 [Coudert et al. (1993)]. There are few general rules on how the nozzle influences the jet because the primary influence is provided by the location of the arc attachment. A smaller nozzle diameter or a constriction of the nozzle downstream of an arcing chamber will result in shorter arcs, lower temperatures at the nozzle exit, though possibly higher velocities for the same current and mass flow rate. The effect of a divergent anode nozzle or a Laval-type anode nozzle has been shown to result in less cold gas

entrainment by the plasma jet [Henne et al. (2001)] and higher deposition efficiencies [Schwenk et al. (2004)].

The mode of gas injection into the discharge cavity, whether radial, axial, or tangential (swirl), offers an important design variable for the control of the fluid dynamics of the flow in the discharge cavity, the arc stabilization, and the characteristics of the plasma jet. An example of the temperature contours for two Ar/H_2 plasma jets, with radial and axial gas injection modes, is given in Fig. 8.63 [Romilhac et al. (1990a, b)]. In both cases, plasma gas composition, flow rates, and arc currents are comparable. Significantly lower temperatures are observed for the plasma jet, with radial gas injection compared to that with axial injection. The effect is attributed to the longer arc length, with axial injection giving rise to a higher arc voltage, and higher power for the same arc current. It should be mentioned that the change from swirl injection to radial injection can be achieved in steps by simply changing the orientation of the gas injection orifices in the gas distribution ring from pointing toward the torch axis (radial injection) to having a purely tangential orientation. Intermediate positions have shown to provide for a stable plasma operating and plasma jet structure [Outcalt et al. (2007)].

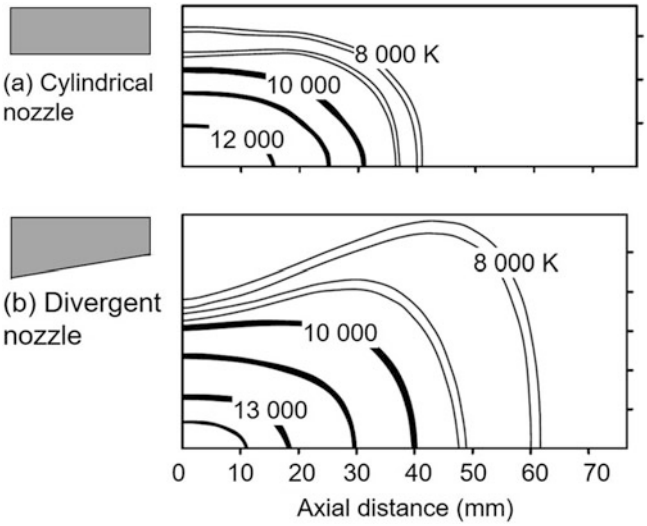

Fig. 8.62 Plasma jet temperature contours for two different nozzle shapes showing the longer and broader jet with a divergent nozzle, (**a**) cylindrical nozzle, (**b**) divergent nozzle. [Coudert et al. (1993)]. (With kind permission from Springer Science+Business Media B.V)

The effect of the surrounding atmosphere is frequently overlooked in plasma spraying. Both the atmospheric pressure and the composition (e.g., humidity) have a strong influence on the jet appearance, and the heat and momentum transfer to the spray particles because the surrounding gas is mixed with the plasma gas in the turbulent jet as described in the previous "Section 8.4.2 ambient gas entrainment by the plasma jet." As an example of this influence, Fig. 8.64 [Romilhac et al. (1990a, b)] shows the constant temperature contours in an argon–hydrogen plasma jet issuing into an air, nitrogen, or argon ambient atmosphere. It is clear that mixing with air results in the strongest quenching of the jet. The quenching will be even stronger when there is high humidity in the air. Lower atmospheric pressures will not only result in less quenching and longer jets but also reduce the heat and momentum transfer to the particles, as discussed in "Chapter 5, Plasma and particle dynamics."

Close attention has also been given to the impact of the electrode design and the operating conditions on the radial profiles of the plasma axial velocity at the torch exit. A study by [Planche et al. (1998)] reported time-of-flight image velocimetry measurements of the plasma axial velocity for a DC plasma torch of conventional design with a cylindrical anode nozzle with an i.d. varying between 6 and 10 mm. The plasma gas was a mixture of Ar/H_2 (25 vol% H_2) or pure N_2, at flow rates varying between 30 and 80 slm. Typical results given in Fig. 8.65 show the radial profiles of the axial plasma velocity for the 10 mm i.d. anode, at a distance of 4 mm from

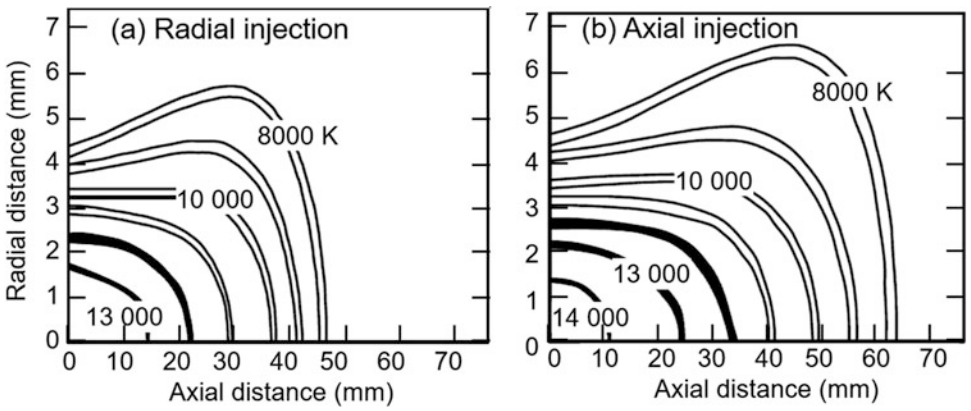

Fig. 8.63 Plasma jet temperature contours for two different plasma gas injection modes indicating the longer high-temperature zone with the axial injection, (**a**) radial injection, (**b**) axial injection (derived from data published in [Romilhac et al. (1990b]

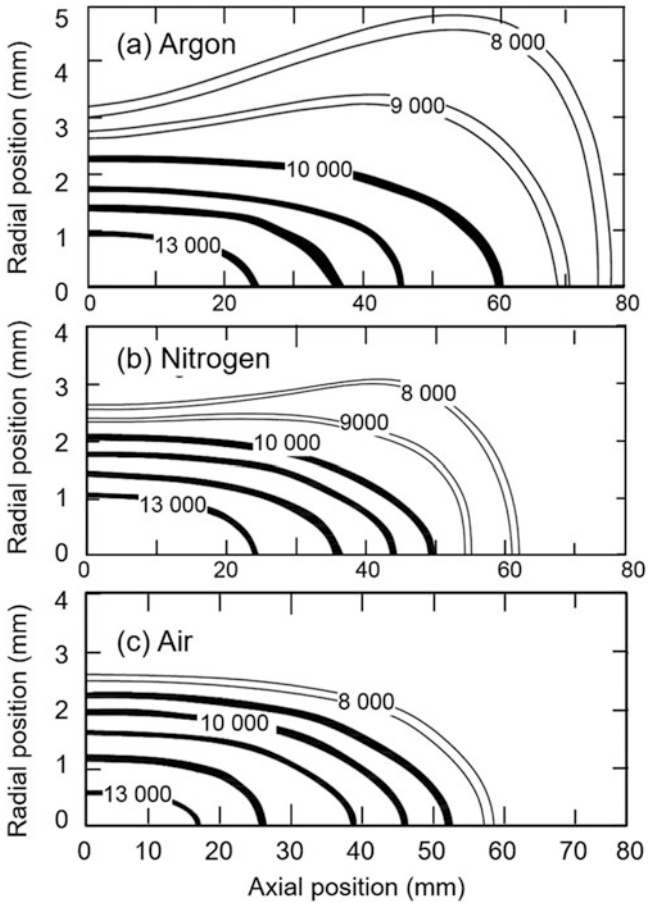

Fig. 8.64 Effect of the ambient gas entrainment on the temperature contours of an argon plasma jet, with air showing the strongest quench effect. (**a**) Argon ambient gas. (**b**) Nitrogen. (c) Air, derived from data published by [Romilhac et al. (1990a, b)]

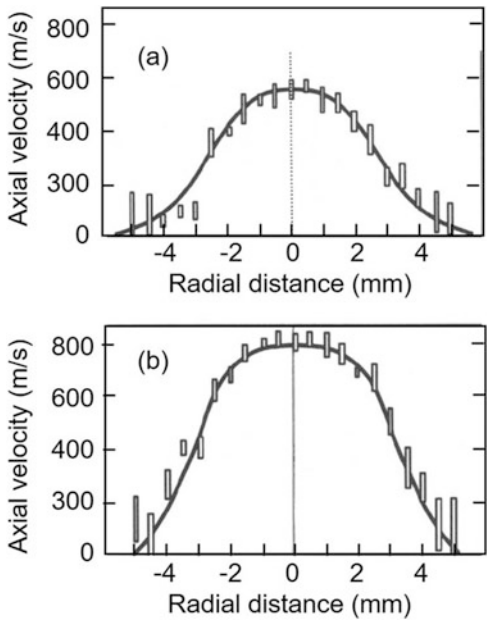

Fig. 8.65 Effect of arc current on the radial profiles of the axial plasma velocity for Ar/H_2 plasma gas flow rate of 60 slm (25 vol.% H_2), *nozzle i.d.* = *10* mm, z = 4 mm from the nozzle exit (**a**) I = 299 A, (**b**) I = 632 A. [Planche et al. (1998)]

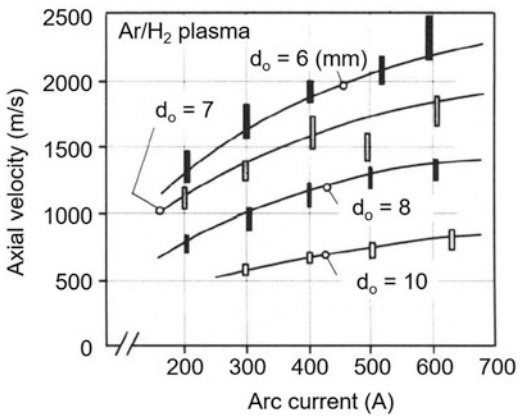

Fig. 8.66 Evolution of the maximum axial plasma velocity on the torch axis, with the arc current for different nozzle i.d.s varying from 6–10 mm, z = 4 mm, Ar/H_2 plasma gas flow rate of 60 slm (25 vol.% H_2). [Planche et al. (1998)]

the nozzle exit, for a single plasma gas flow rate of (45 slm Ar +15 slm H_2) and arc currents of 299 and 632 A. The corresponding arc voltages were respectively 64.5 and 48 V (arc power of 19.3 and 30.3 kW). The results indicate that the increase in the arc current from 299 to 632 A gives rise to an increase in the maximum plasma velocity on the axis of the torch, from 550 to 780 m/s, together with the flattening of the profile. These results are summarized in Fig. 8.66, where the center line velocities at the nozzle exit (4 mm) are plotted as functions of arc current for a 60 slm flow rate and nozzle internal diameters ranging from 6 to 10 mm. As can be expected, the tendencies shown in this figure indicated the strong influences of both the diameter and the arc current intensity on the velocity values.

The effect of the gas flow rate on velocity distributions is illustrated in Fig. 8.67 for the same plasma torch using an 8 mm i.d. anode nozzle and the same plasma gas composition of Ar/H_2 (25 vol.% H_2). For gas flow rate value of 32, 48, and 68 slm. The arc current was fixed in all three cases at 600 A. The corresponding arc voltage increased steadily with the increase in the plasma gas flow rate to 45, 55, and 58 V, respectively (torch power 27.0, 33.0, and 24.8 kW). It may be noted that the maximum plasma velocity did not follow the flow rate changes and seemed to be almost constant (1200 ± 100 m/s), despite the fact that the flow rate was increased by a factor higher than 2. As suggested by the solid curves plotted in these figures, by reducing the velocity profile width when it was increased, the flow rate seemed to participate efficiently to the thermal pinch of the arc column.

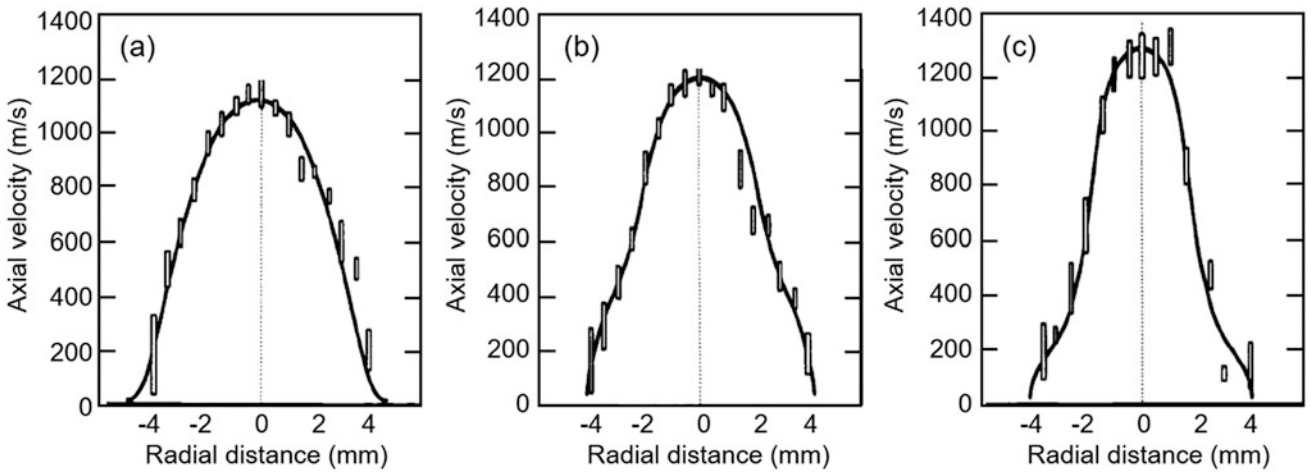

Fig. 8.67 Effect of plasma gas flow rate on the radial profiles of the axial plasma velocity for DC plasma torch, do = 8 mm, z = 4 mm. Plasma gas Ar/H_2 (25 vol.% H_2) I = 595 ± 5 A, (**a**) 32 slm (**b**) 48 slm; (**c**) 68 slm. [Planche et al. (1998)]

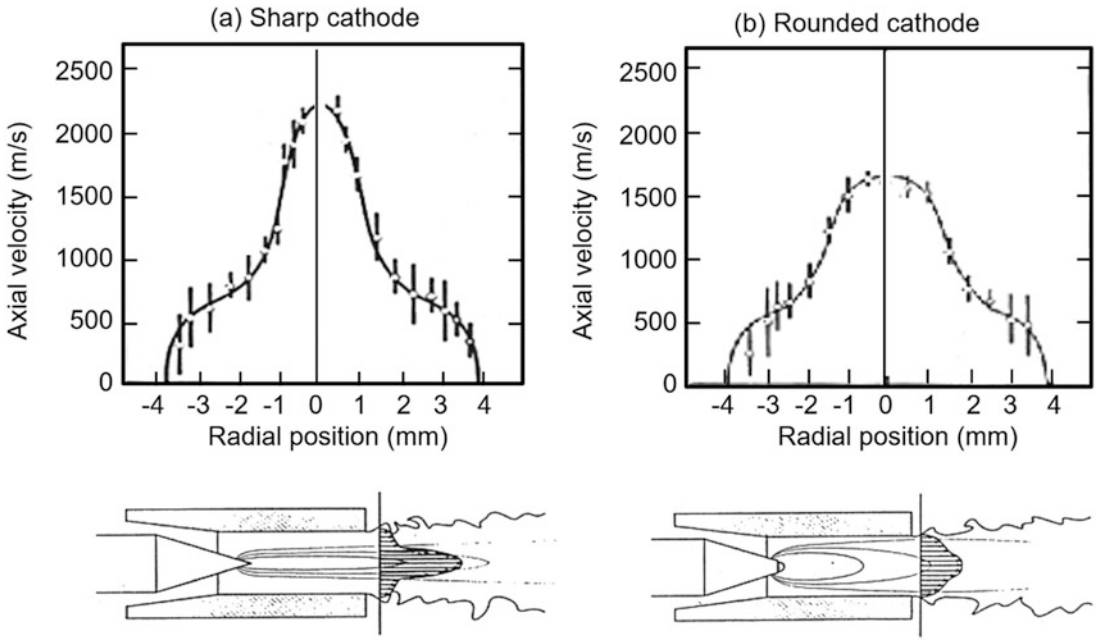

Fig. 8.68 Effect of cathode tip melting and erosion on plasma jet axial velocity profiles, Ar/H_2 plasma (45 slm Ar + 15 slm H_2), 604 A, 7 mm nozzle i.d. [Planche et al. (1995)]. (Reproduced with kind permission of IPCS)

An interesting observation reported by [Planche et al. (1995)] is the dependence of plasma jet characteristics on the state of erosion of the torch electrodes. Fig. 8.68 shows the velocity profiles obtained under essentially the same conditions (d_o = 7 mm, z = 4 mm, Ar/H_2 (25 vol.% H_2) flow rate of 60 slm, and arc current 604 A), with a cathode with a sharp conical tip (Fig. 8.68a) and with one that has a rounded tip due to tip melting and erosion wear (Fig. 8.68b). The higher peak velocities and steeper radial profiles with the sharp-tipped cathode are evident. A narrow conical cathode tip will be molten during operation and therefore eroding quickly due to the ejection of small molten droplets, resulting in a change of cathode shape within the first hour of operation. This change will be accompanied by a change in the plasma jet characteristics, and in the particle heating and acceleration, and consequently in the coating characteristics. From a cathode design point of view, a "burn-in" period will be required before reproducible coatings can be obtained.

Measurements [Hrabovsly et al. (1997)] and modeling studies [Jenista (2017)] were reported of the plasma velocity and temperature fields for a steam plasma torch operating arc currents varying between 300 and 600 A, with corresponding

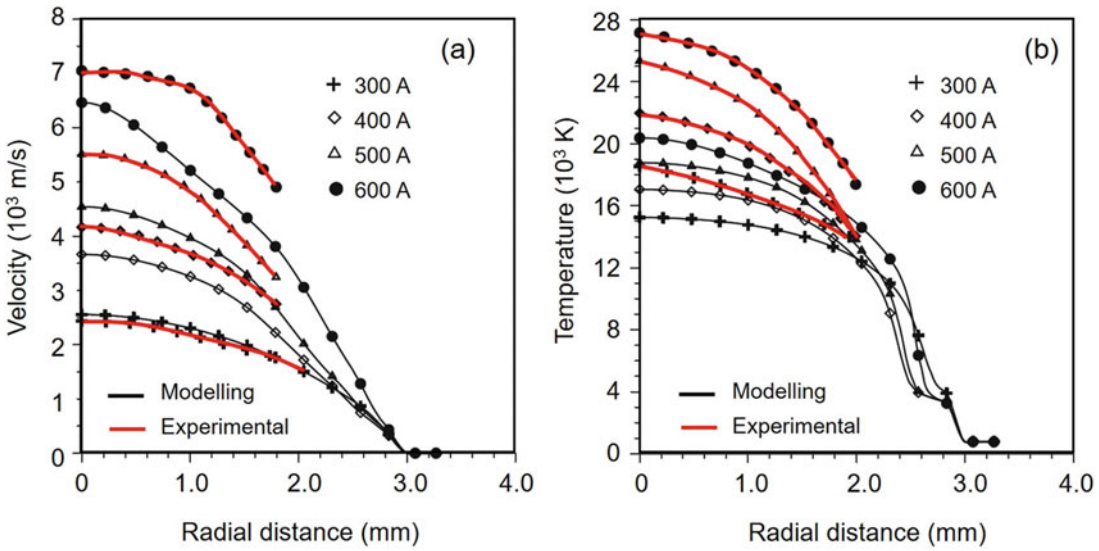

Fig. 8.69 Calculated and experimental radial profiles of the plasma (**a**) velocity and (**b**) temperature for a steam plasma torch as function of the arc current (300–600 A), exit torch nozzle i.d. = 6 mm. [Jenista (2017)]

DC torch power of 55.5 to 123.7 kW; water evaporation rate was estimated to vary between 0.204 and 0.325 g/s (0.734–1.17 kg/h). The torch nozzle diameter was 6.0 mm, with measurement carried out at a distance of 2 mm downstream of the nozzle exit. The results given in Fig. 8.69 show centerline plasma velocity increasing from 2500 to close to 7000 m/s and centerline maximum plasma temperatures of 18,000 to 27,000 K, with an increase in the arc current from 300 to 600 A. While the measured and model-predicted velocity profiles seem to be consistent in reasonable agreement, important differences are observed in terms of the temperature fields, which vary sometimes by a few thousands of degree K. The data provide, however, some indication of upper velocity and temperature limits meet in spray plasma torches which have been successfully used for the spraying of ceramic coatings, such as alumina, on an industrial production level.

8.4.4 Particle Dynamics in Plasma Flows

As mentioned in "Chapter 5 Plasma and particle dynamics in thermal spray," and earlier in this chapter, the injection of the coating precursor, whether it is as a dry powder, solution, or suspension, is the most critical step in the plasma-spraying process, on which depends, to a large extent, the quality of the coating produced. A slight deviation from near-optimal conditions can lead to widely varying changes in the quality of the coating, whether in terms of coating density, adhesion, and microstructure, or the process efficiency in terms of the fraction of the powder deposited on the substrate. The instabilities and continuous oscillation of the generated plasma jet, as described earlier in Sect. "8.2.4 Arc stability," and "8.4.1 Arc and plasma jet dynamics," and demonstrated by the high-speed photographs given in Fig. 8.70, offer a significant challenge that requires a thorough understanding of particle dynamics under plasma conditions for process optimization. In this figure, the spray particles are injected from the top, and the plasma jet exits the nozzle at the right-hand side of the images. It can be seen that the arc fluctuations lead to uneven particle heating and the entrainment of cold surrounding gas into the jet, rapidly reducing its average temperature and velocity. In this section, the focus will be on the feeding of dry powder using pneumatic transport and injection into the plasma stream. Current DC torches used in plasma spray operations, as described in Sect. "8.3 Plasma Torch Design," mostly allow for the radial injection of the powder into the plasma either internally, in the anode nozzle such as in the SG-100 TAFA-Praxair torch, or externally at the exit level of the nozzle, such as in the F4 MB-XL or Triplex torches by Oerlikon-Metco. The Northwest Mettech Axial III is one of the few DC plasma spray torches that allow for axial injection of the powder into the plasma stream. For simplicity, the discussion in this section will be limited to the radial injection of the powder into the plasma stream. A detailed discussion on particle injection in plasma torches, and particle trajectory and temperature history calculations under plasma conditions can be found in "Chapter 5 Plasma and particle dynamics in thermal spray."

In a conventional plasma-spraying torch, the particles are injected into the plasma jet either inside the anode nozzle or right outside of the nozzle exit, with an injector tube of diameter typically between 1.2 and 2 mm. The direction of injection can be perpendicular to the jet axis or at a positive or

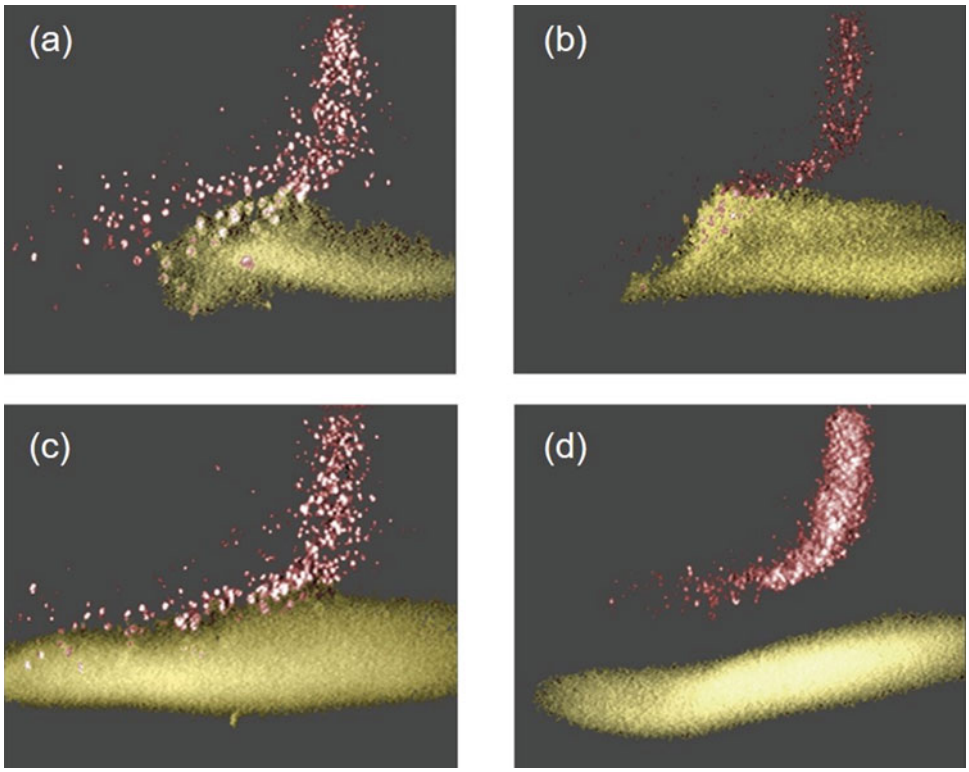

Fig. 8.70 High-speed images showing the fluctuations of the plasma jet and the spray particle fluxes being exposed to varying environments. [Fauchais (2004)]. (Copyright IOP Publishing. Reproduced with permission. All rights reserved)

negative angle with respect to the perpendicular direction. Injection with a negative angle with respect to the injector axis (backward injection) can result in higher particle temperatures but somewhat lower particle velocities [Bisson et al. (2005)]. Internal injection requires careful adjustment of the carrier gas flow; too high flow rates will result in the particles impinging on the opposite side of the anode nozzle. It would also create strong deflection of the plasma jet. As a guideline, the carrier gas mass flow rate should be below 10% of the mass flow rate of the plasma gas.

Among the different independent parameters that control the particle trajectory in a DC plasma jet, the size distribution of the spray powder is one of the most important since the momentum of the particle is proportional to the third power of the particle diameter. For example, if the spray powder has a nominal size distribution of 10–50 μm, the momentum of the particles can vary by a factor of 125 for the same velocity, resulting in vastly different trajectories. In general, small particles remain in the fringes of the jet, never reaching the hot core. However, their residence times in the lower-velocity regions of the jet are longer and the time needed for their melting is shorter because of their lower-mass particles. The large particles will traverse the jet and remain in the fringes on the opposite side, and it is likely that these particles are not fully molten when they hit the substrate. The intermediate-size particles will have the optimal trajectories for particle heating and melting. In general, it is recommended to use powders with a particle size distribution (PSD) as narrow as possible and adjust the carrier gas flow rate such that the mean particle momentum is equal to the plasma jet momentum flux. It is possible also to reduce the carrier gas flow rate to allow a more favorable trajectory of larger particles. There are several instruments that allow online observation of the particle fluxes/trajectories and that can be used to adjust the carrier gas flow rate to an optimal value for a given particle mass flow rate and torch-operating conditions.

A schematic of a typical arrangement for internal powder injection in a DC plasma torch is given in Fig. 8.71a [Vardelle et al. (2001)], together with radial profile powder distribution at a distance of 70 mm from the exit level of the torch nozzle, Fig. 8.71b [Vardelle et al. (2001)]. The plasma jet in this case was an Ar/H_2 plasma (45 slm Ar + 15 slm H_2), an arc current of 600 A, a torch nozzle i.d. of 7 mm, an injector i.d. of 1.75 mm, and the powder injection point = 3 mm upstream of nozzle exit. Injected alumina powder had a particle diameter (−45 + 22 μm). The result shows a gaussian powder distribution, with its maximum further away from the torch axis with increase in the powder carrier gas flow rate.

The dependence of the particle trajectories on their mass and injection velocities is best demonstrated by the experimental and numerical simulation studies reported by

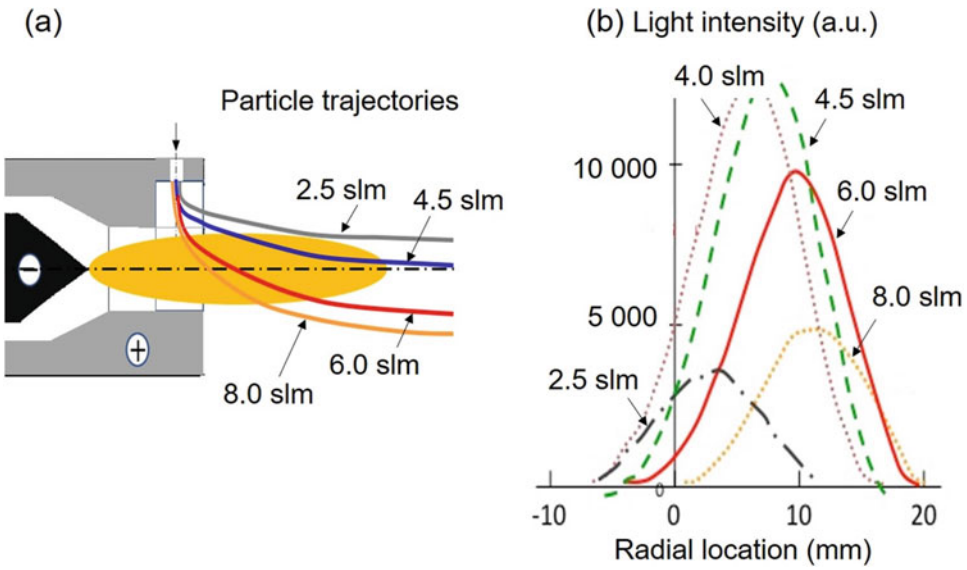

Fig. 8.71 (**a**) schematic of internal powder injection in a DC plasma torch (**b**) Effect of carrier gas flow rate on radial distribution of alumina powder (22 to 45 μm) in an Ar/H_2 plasma jet (45 slm, Ar + 15 slm H_2) P_o = 20 kW, Nozzle i.d. = 7 mm, injector i.d. = 1.8 mm, powder injection = 3 mm upstream of nozzle exit, Measurement = 70 mm downstream of nozzle exit. [Vardelle et al (2001)]

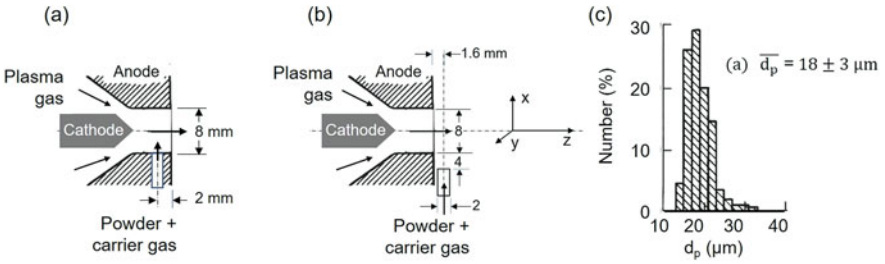

Fig. 8.72 Schematics of the plasma torch nozzle designs used with (**a**) internal powder injection, (**b**) external powder injection, and (**c**) particle size distribution (PSD) of the fine alumina powder used in the study. [Vardelle et al. (1983, 1988)]

[Vardelle et al. (1983, 1988)] for alumina powder injection into Ar/H_2 DC plasma jet generated by a torch of conventional design with both internal and external powder injection configurations. In the first study [Vardelle et al. (1983)], the anode nozzle of the plasma torch had an 8 mm i.d., with an internal powder injection port, as illustrated in Fig. 8.72a, with a diameter of 2 mm and its axis 2.0 mm upstream of the nozzle exit. The torch was operated with a mixture of Ar/H_2 (75 slm Ar + 15 slm H_2), or N_2/H_2 (37 slm N_2 + 11 slm H_2) as plasma gas, arc current of 290 A, and voltage 100 V, giving rise to a DC torch power of 29 kW in both cases, and energy efficiency, η,of 63% for the Ar/H_2 operation and 72% for the N_2/H_2 operation. Where, η is defined as the fraction of the DC power that is coupled into the plasma jet at the exit of the torch. Measurements were made of the temperature field in the jet using a combination of emission spectroscopy and probing using thermocouples. Plasma velocity measurements were carried out using Laser Doppler Anemometry (LDA) after seeding the gas with ultrafine tracer particles. With the injection of course alumina powders into the plasma jet, particle velocities and surface temperature were measured, respectively, using LDA and two-wavelength pyrometry. A summary of the alumina powder characteristics and their corresponding radial injection velocities is given in Table 8.2. Typical results for torch operation with Ar/H_2 mixture are given in Fig. 8.73 in terms of the measured axial particle velocity profiles along the centerline of the torch for different powders. Superposed on the graph is the measured axial velocity of the plasma flow along the centerline of the torch, and the results modeling work, as discussed in "Chapter 5 Plasma and particle dynamics in plasma spraying," of the axial velocity of individual particles with the mean particle diameter of the different powders and their corresponding injection velocities in the jet. As expected, the smaller particles, because of their lower inertia, are accelerated much faster by the flow compared to the heavier

Table 8.2 Summary of alumina powder characteristics and their corresponding injection velocities in the plasma flow

Powder	$\overline{d_p}$ (μm)	σ_g	v_{pi}(m/s) (N_2/H_2) plasma	v_{pi}(m/s) (Ar/H_2) plasma
A	18	1.18	25.0	32.0
B	23	1.19	22.0	29.0
C	39	1.20	18.0	24.0
D	46	1.20	14.0	19.0

[Vardelle et al. (1983)]

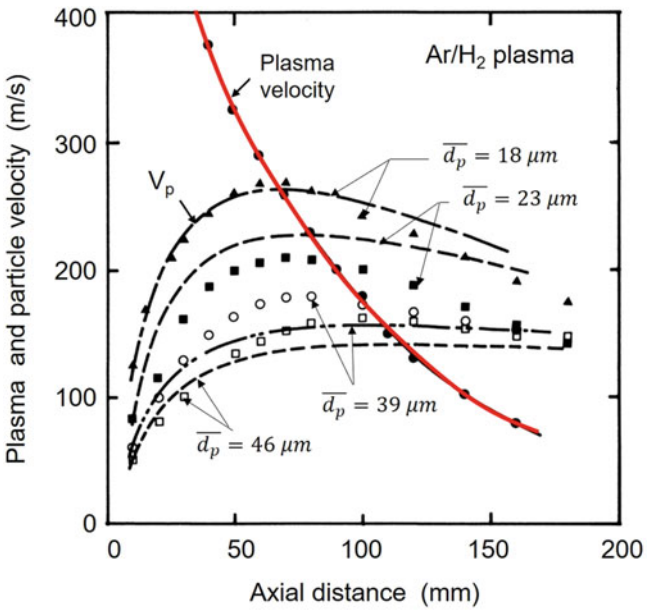

Fig. 8.73 Experimental (symbols) and modeling (solid lines) results of plasma and particle axial velocity along the centerline of Ar/H_2 plasma jet. [Vardelle et al. (1983)]. (With kind permission from Springer Science+Business Media B.V)

particles. The latter, however, once they attain their maximum velocity at a distance of about 60 to 80 mm from the nozzle exit, maintain their momentum and eventually move at a higher velocity than that of the plasma at a distance of 140 to 160 mm from the nozzle. It may also be noted that the measurement particle velocity profiles (symbols) are consistent with the modeling results (solid lines), though at time significant differences in their numerical values can be observed. This could be largely due to the significant simplifying assumptions that have been addressed in subsequent modeling studies.

Subsequent studies [Vardelle et al. (1988)] were carried out for essentially the same type of plasma torch, with the exception of using external powder injection, as shown in Fig. 8.72b, and limiting the work to a single alumina powder with the particle size distribution given in Fig. 8.72c, with a mean particle diameter of 18.0 ± 3 μm. The powder is injected at the base of the plasma jet using a 2.0 mm i.d. injector tube, with its axis at 1.6 mm downstream from the surface of the nozzle and its tip withdrawn by a distance of 4 mm from the edge of the plasma jet to avoid overheating and melting. The plasma gas flow rate was (75 slm Ar + 15 slm H_2) and DC power 29.0 kW. Close-up of the particle trajectories and the number flux powder distribution along two orthogonal axes, at 20 mm from the exit level of the plasma jet, are given in Fig. 8.74. The results given for a carrier gas feed rate of 5.5 slm (Ar) show a skewed distribution in the powder injection plane while a centered symmetrical one in the orthogonal plan. The corresponding values of the distribution of the particle parameters (particle velocity, surface temperature, and number flux density) in the injection plane (x-axis) are given in Fig. 8.75. The measurements carried out using laser anemometry and two-wavelength pyrometry were carried out in a plane at 75 mm downstream from the exit level of the nozzle of the plasma torch for different powder carrier gas flow rates over the range of 5.5 to 8.5 slm (Ar).

Results given in Fig. 8.75a show maximum particle velocities at the centerline of the flow of 210–220 m/s range. The particle velocity drops rapidly with distance from the center to around 180 m/s at ±5 mm. Fig. 8.75b shows the corresponding particle surface temperature distributions, with essentially the same observation of maximum temperature for particles around the axis of the flow, with particle surface temperatures in the 3000–3200 K temperature range, which indicates the alumina particles to be fully molten. The last graph Fig. 8.75c gives the corresponding particle number flux distributions, which shows a strong dependence on the powder injection velocity. Knowing that the injection position is on the negative side of the x-direction, it is consistent to observe the position of maximum flux density shifting in the opposite direction with increase in the powder gas flow rate. While having maximum particle velocities and temperatures seems consistent with the fact that the plasma jet also has its maximum velocity and temperature in the same location, it is disruptive to see that only at a carrier gas flow rate of 5.5 slm that the maximum particle flux density also coincides with the maximum velocity and temperature, meaning that the great majority of the particles would have acquired the necessary energy level for full melting of the particles and their acceleration, which are necessary conditions for obtaining a good-quality coating with a satisfactory deposition efficiency, η_D. The latter is defined as the fraction of the powder feed into the

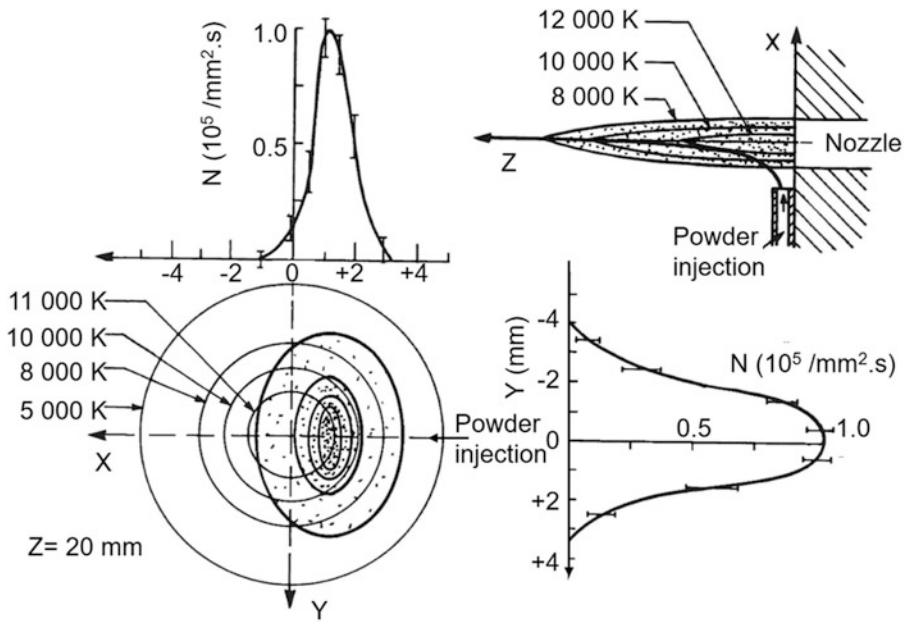

Fig. 8.74 Particle trajectories and number flux density distribution for the injection of the fine powder, 18 ± 3 μm in a 29.2 kW Ar-H_2 plasma, 75 slm (Ar) + 15 slm (H_2), with a carrier gas flow rate of 5.5 slm (Ar). [Vardelle et al. (1988)]

plasma that are deposited on the substrate and contribute to the formation of the coating. For higher carrier gas flow rates, $Q_i = 7$ or 8.5 slm, it is obvious that an increasing fraction of the powder will not acquire the same conditions in terms of particle velocity, temperature, and degree of melting giving rise to a poorer deposition efficiency. Moreover, since non-molten particles tend to be at the source of defects and porosities in the coating, the quality of the coating would also suffer. It is, therefore, important to stress that when measuring parameters such as the velocity or temperature of particles in a spray environment, it is important to integrate the mass flux density in the analysis in order to evaluate the full picture of the spraying operation.

Special attention has also been given to the anode design and its impact on the plasma flow and consequently on the particle trajectories and their temperature history. While as seen earlier, most commercial plasma torches use anodes with cylindrical nozzle bores, Laval-type nozzles with a convergent/divergent profile have also been used. As observed in Fig. 8.62 [Coudert et al. (1995)], a small change in the nozzle design by having a slight divergence of the nozzle downstream of the arc attachment can significantly change the jet temperature distributions. This type of nozzle provides a somewhat more uniform velocity and temperature distribution at the nozzle exit and a reduced turbulent entrainment of cold gas [Henne et al. (2001)], resulting in more uniform particle heating and acceleration [Roumilhac et al. (1990b), Rahmane et al. (1998)]. There are few general rules on how the nozzle influences the jet because the primary through its impact on the location of the arc attachment. A smaller nozzle diameter or a constriction of the nozzle downstream of an arcing chamber will always result in shorter arcs and lower temperatures at the nozzle exit, but higher velocities for the same current and mass flow rate of the plasma-forming gas. The effect of a divergent anode nozzle or a Laval-type anode nozzle has been shown to result in higher deposition efficiencies [Schwenk et al. (2004)].

Figure 8.76 [Coudert et al. (1993)] shows that for Al_2O_3 and YSZ particles, the maximum particle velocity, measured using LDA at a location 100 mm downstream of the nozzle exit, increases linearly with current for a nozzle diameter of 7 mm, with a considerably smaller increase with the current observed for a 10 mm diameter nozzle.

A comparison of plasma jet and particle characteristics obtained with a supersonic nozzle (the authors derived from measurements of the pressure drop across the nozzle a Mach number value of M = 1.6 at the nozzle exit) and a commercial M = 1 nozzle shows that the cold air entrainment is lower by a factor of 2 in the supersonic jet [Fincke et al. (1993a, b)]. At a distance of 100 mm from the torch, WC:Co particle velocities at the axis are 380 m/s for the supersonic nozzle vs. 200 m/s for the sonic nozzle. Particle temperatures are given as 3200 K for the supersonic nozzle vs. 2300 K for the sonic nozzle. It is interesting to note that the plasma temperatures at the nozzle exit are higher with the sonic nozzle, but the stronger entrainment of ambient air leads to a faster decrease in temperatures, and at an axial position 100 mm from the nozzle, the gas temperatures are about 1600 K for the supersonic jet and about 1100 K for the sonic jet.

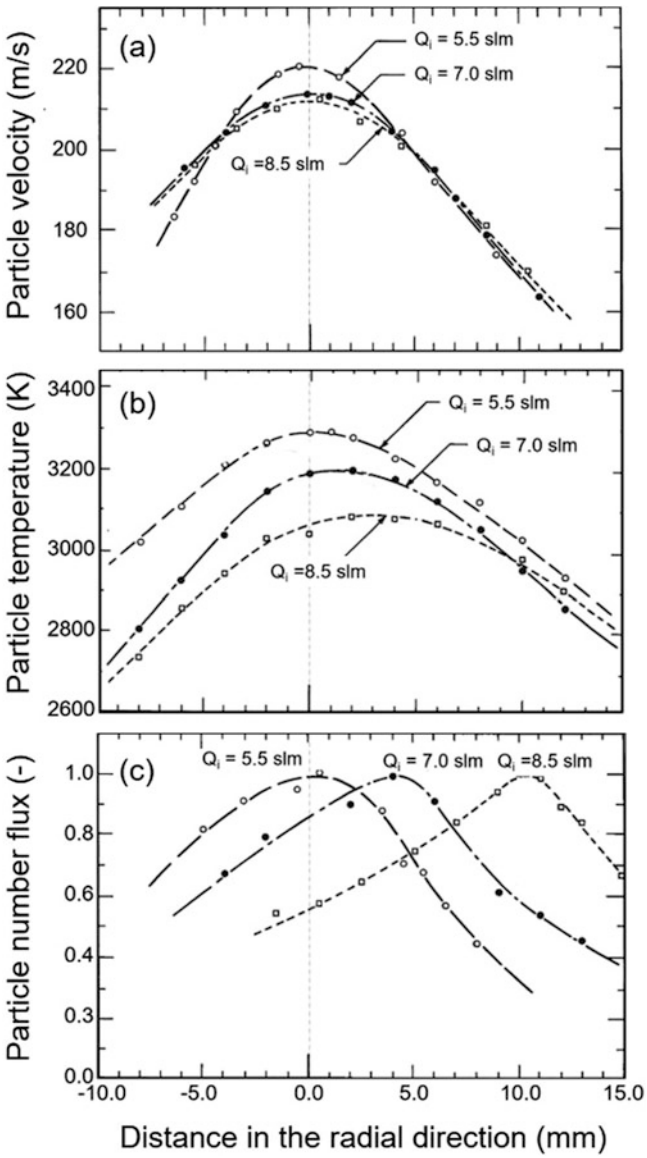

Fig. 8.75 (**a**) Axial velocity, (**b**) Temperature, and (**c**) Number flux density of the particles at 75 mm from the exit of the DC plasma torch operating at atmospheric pressure using 75 slm (Ar) +15 slm (H_2) as plasma gas and power of 29.2 kW. Alumina powder $d_p = 18 \pm 3$ μm injection at different carrier gas flow rate, Q_i (Ar). [Vardelle et al. (1988)]

In Fig. 8.77, two different commercial torch nozzle designs (SG-100/175 and SG-100/324) are shown for the SG-100 torch (Praxair-TAFA). The corresponding particle velocity, temperature, particle diameter, and flux distributions are given in Fig. 8.78. Yttria-stabilized Zirconia (YSZ) (20%) particles are injected from the positive y-direction into the plasma jet. The figure shows the particle characteristics in a plane of particle injection (y-direction) perpendicular to the torch axis, as a function of the distance from the torch axis, at an axial location 80 mm from the nozzle exit. Particle velocities, temperatures, diameters, and fluxes are all averaged values

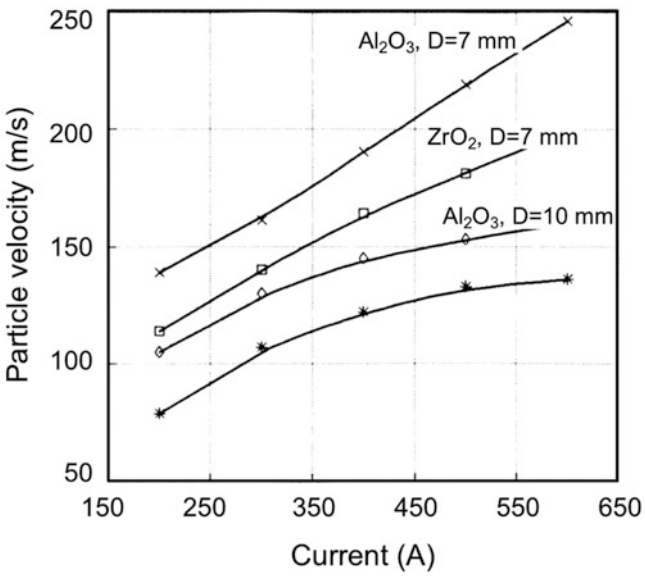

Fig. 8.76 Effect of arc current on particle velocity for two nozzle diameters (7 mm and 10 mm), and two powder materials (Al_2O_3 and YSZ). [Coudert et al. (1993)]. (Reprinted with permission of ASM International. All rights reserved)

over 1000 particles. The normalized flux shown is the ratio of particles detected at a specific y-location in particles per second, divided by the particle flux at all y-locations. All the data have been obtained with the DPV 2000 instrument (Tecnar Automation, Montreal, Canada), at 800 A arc current and plasma gas flow rate of (48 slm Ar +12 slm He). The powder feed rate was 5.8 g/min with a carrier gas of 2.5 slm (Ar). It may be noted that:

(a) the highest velocities and temperatures are for the particles on the axis;
(b) the highest particle fluxes are below the axis for particle injection above the axis;
(c) the largest particles are farthest from the jet axis, and have lower temperatures and velocities;
(d) the supersonic anode provides higher velocities but lower temperatures.

Comparing these results with those presented by [Fincke and Swank (1992)], one must conclude that the specific design of the supersonic nozzle can affect entrainment and the temperature decay, and that the observed results may be different for different materials.

8.4.5 Plasma Torch and Spray Process Modeling

[Watson and Pegot (1962)] have reported one of the earliest models in this field for the entrance, as well as for the

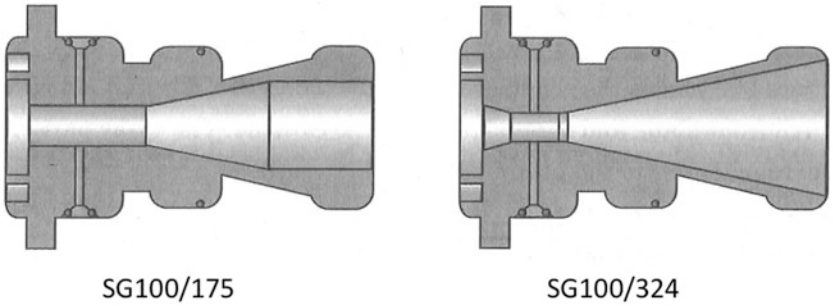

Fig. 8.77 Anode nozzle profiles for the Praxair-TAFA SG 100 torch, No. 175 (left) and No. 324 (right) used in the study. (Reproduced with kind permission of Praxair-TAFA)

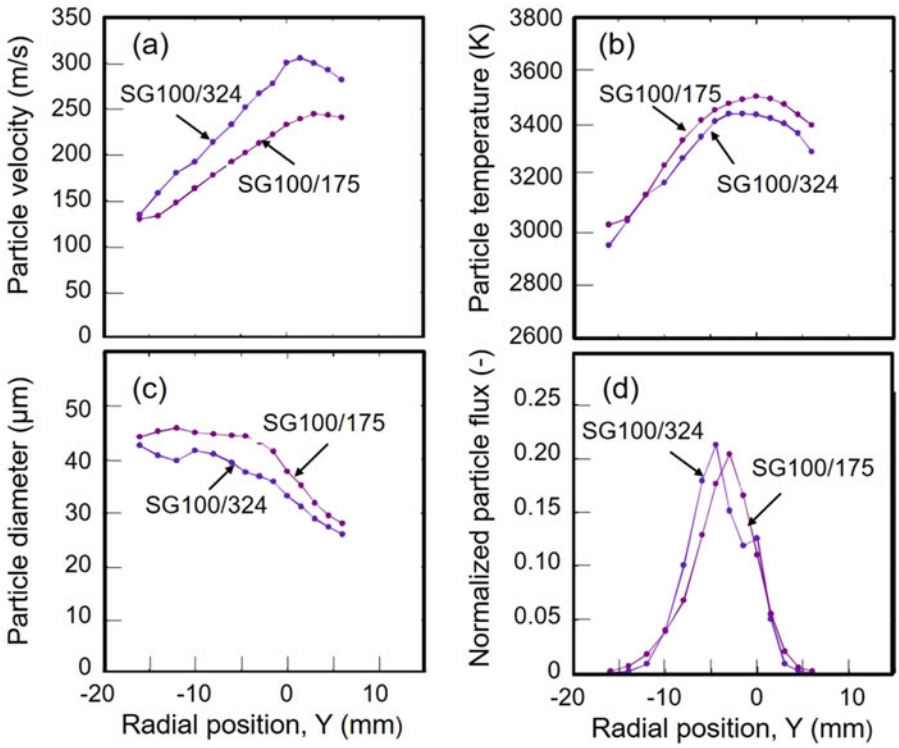

Fig. 8.78 Measurements of the distribution of average values of (**a**) particle velocity, (**b**) particle temperature, (**c**) particle diameter, and (**d**) relative particle flux for two Praxair-TAFA SG-100 anode nozzles. Measurements made at 80 mm from the nozzle exit. 800 A, Ar/He plasma gas (48 slm Ar + 12 slm He), carrier gas flow 2.5 slm (Ar), YSZ powder feed rate 5.8 g/min

asymptotic region of arcs in laminar flow. Fig. 8.79 shows select results for a nitrogen arc, for a current of 580 A, and ambient pressure slightly above atmospheric. The plasma enthalpy (Fig. 8.79a) increases rapidly in the entrance region, reaching a peak before it levels off toward the fully developed (asymptotic) region of the arc. In spite of the high axial velocities (see Fig. 8.79d), the mass flow rate within the constrictor (Fig. 8.79b) is essentially confined to a relatively cold boundary layer close to the wall of the arc confinement tube, especially in the vicinity of the entrance. This effect is due to the low mass density of the plasma in the arc core (see Fig. 8.79c representing l/ρ for N_2), which is a consequence of the high enthalpies (temperatures) in the arc axis. With increasing distance from the entrance, more and more of the cold gas permeates into the arc.

Numerous models exist for both plasma spray torches and plasma spray processes including the particle trajectories [Pfender et al. (1985), Pfender (1989), Chyou et al. (1989a, b), Li and Pfender (2005)]. Only a brief overview will be given here; a more detailed discussion has been presented in "Chapter 4 Plasma-particle momentum and heat transfer" and "Chapter 5 Plasma and particle dynamics in thermal spray." The reader is also encouraged to consult the relevant literature for details.

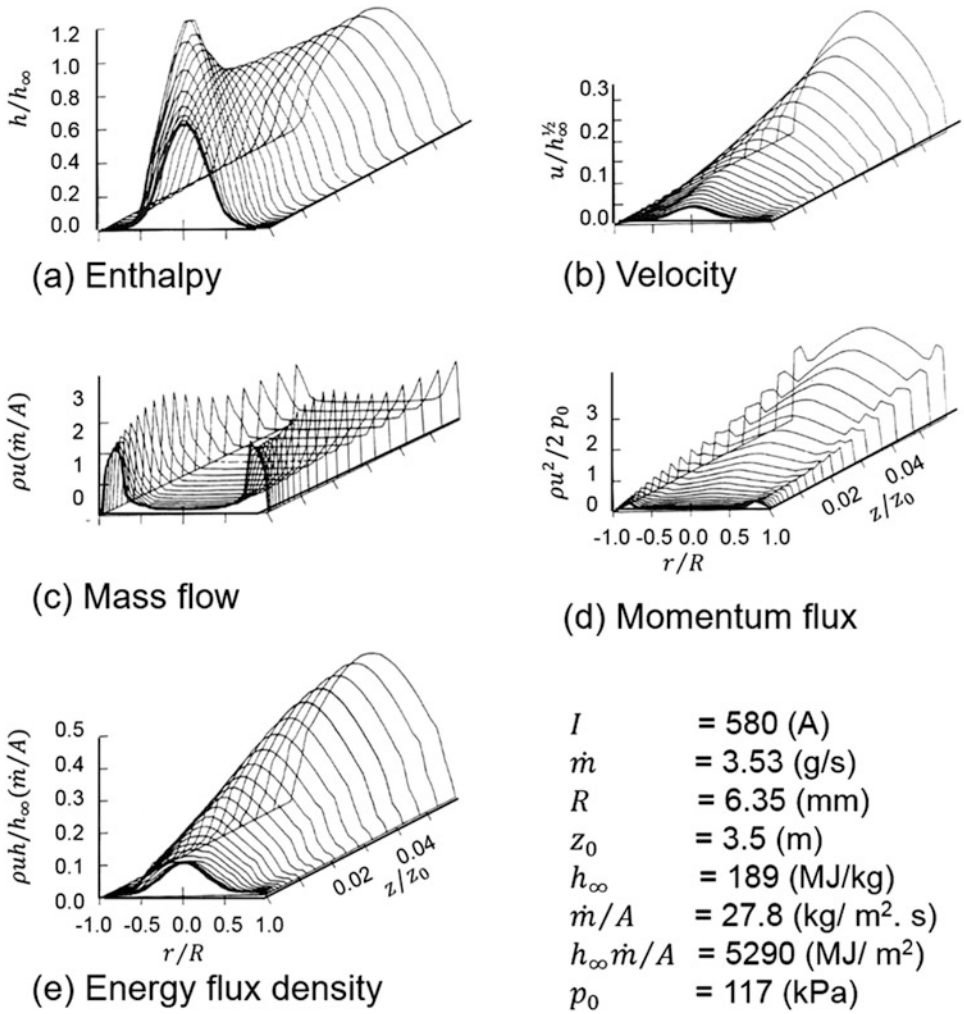

Fig. 8.79 Calculated performance of a wall-stabilized nitrogen arc in axial flow. [Watson and Pegot (1962)]

The traditional models assumed axisymmetric, steady-state plasma flow, allowing a two-dimensional treatment of the torch fluid dynamics. The conservation equations are solved numerically together with the relevant Maxwell equations and thermodynamic equations. Typical boundary conditions are an assumed current density profile at the cathode and an artificially high electrical conductivity in the anode boundary layer to allow current transfer through the low temperature layer while keeping the assumption of LTE. Turbulence is treated using either a K–ε or a Reynolds Stress approach, but usually for low Reynolds numbers. Two-dimensional particle trajectories are calculated in a plane formed by the direction of the particle injection and the torch axis, using the local plasma properties for determining the particle heating and acceleration. Steady-state three-dimensional models have demonstrated the effect of the carrier gas on the temperature and velocity distributions of the plasma jet and the particle trajectories [Li and Pfender (2005)]. The results show good agreement with time-averaged experimental measurements. However, one has to keep in mind that very strong fluctuations exist of the plasma properties, and averages can reproduce only a part of the process. Nevertheless, such models have been used to evaluate operational characteristics of new torch designs, for example, for the Sulzer Metco Triplex torch [Muggli et al. (2007, Molz et al. (2007)], and the potential for expanding their range of operating conditions.

Among the approaches that attempt description of the large-scale turbulence in the jet are the assumption of a time-varying radial profile for the plasma temperatures and velocities at the nozzle exit [Dussoubs et al. (1999), Park et al. (1997, 1999), and the use of a two-fluid model [Huang et al. (1995a, b, c), where one of the fluids is the cold gas moving toward the jet axis, while the other fluid is the hot plasma moving in the outward direction, in addition to the movement in the axial direction (see Fig.8.80) [Huang et al. (1995c]. Calculations have been performed only for argon jets into an argon environment with the assumption of LTE. Both

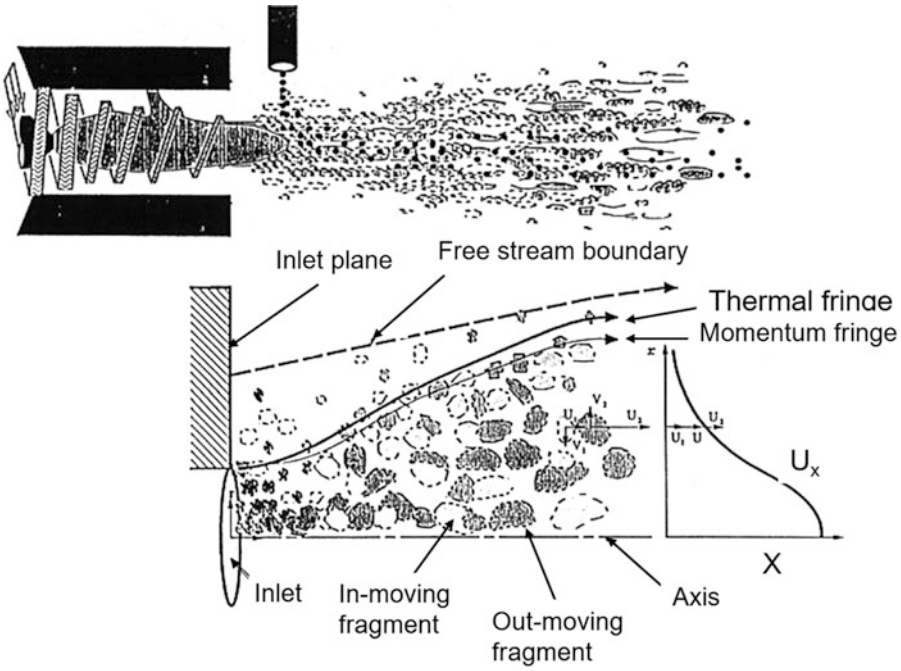

Fig. 8.80 Illustration of two-fluid approach for simulating cold gas entrainment by the plasma jet. [Huang et al. (1995)]. (With kind permission from Springer Science+Business Media B.V)

approaches have demonstrated that particles injected with uniform size and velocity experience different heating and acceleration conditions due to the plasma property fluctuations, resulting in different particle trajectories and temperatures at the substrate location. This is shown in Fig. 8.81 [Huang et al. (1995a), in which the results of the two-fluid model show that because of the different radial velocities in the different gaseous environments, there is a divergence in the particle trajectories (Fig. 8.81a); particles with the same mass and injection velocities can be exposed to plasma velocities of 80 to 400 m/s (Fig. 8.81b) and plasma temperatures of 4000 K to about 11,000 K (Fig. 8.81c) depending on whether the particle sees the hot plasma or the entrained cold gas bubble. This fact leads to a wide range of particle temperatures and velocities at the axial position where the substrate would be located. The two-fluid model has demonstrated further the experimentally confirmed observation that the entrained cold gas bubbles require a significant amount of time to break up and mix with the hot plasma gas, and only at a location typically four to five nozzle diameters from the nozzle exit is the jet composition relatively uniform and less entrainment of larger cold gas bubbles occurs (see Sect. 8.4.2 Ambient gas entrainment by the plasma jet). A simulation of the plasma jet using the LAVA code [Williamson et al. (2003)] showed that even with the assumption of a steady arc and turbulence as modeled using a K–ε approach, a significant amount of entrainment can be predicted being responsible for the rapid axial temperature drop three to four nozzle diameters downstream of the nozzle exit, results corroborated by experiments [Finke et al. (2003)].

8.5 Summary and Conclusions

The increasing demand for combined functional requirements such as high temperature resistance to corrosive atmospheres, in addition to abrasive wear resistance, and the ease of machining to the final form, at competitive costs has led to the ever-increasing demand for coatings. DC plasma spray coating has emerged as one of the leading plasma spray processes that is presently widely used on an industrial scale. According to [Fauchais et al. (2014)], the motivation for coating structural parts can be summarized by the following needs:

(a) improve functional performance by, for example, allowing higher temperature exposure through the use of thermal barrier coatings,
(b) improve component life by reducing wear due to abrasion, erosion, and corrosion,
(c) extend functional use by rebuilding the worn part to its original dimensions, avoiding the need for replacing the entire component, for example, a shaft or an axle, and,
(d) reduce component cost by improving the functionality of a low-cost material with an expensive coating.

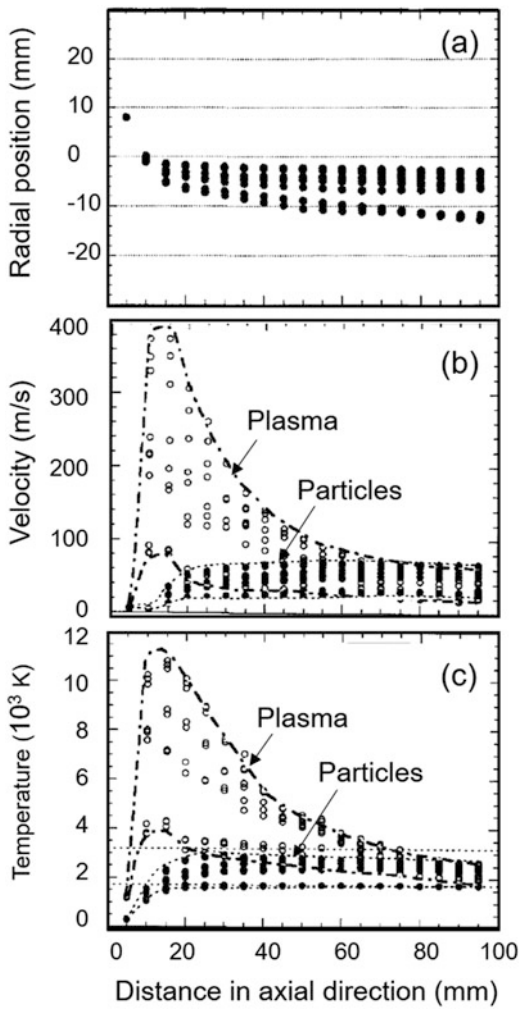

Fig. 8.81 Results of stochastic particle injection model into two-fluid plasma jet; 30 μm diam. Ni particles injected 5 mm downstream of nozzle exit at 5 m/s, anode nozzle i.d. 8.5 mm. Torch operation at 400 A, 23.9 V, thermal efficiency 42.2%, gas flow rate of 35.4 slm (Ar), (**a**) particle trajectories (**b**) axial particle velocities, and (**c**) plasma temperatures; (open symbols) representing plasma values and (closed symbols) representing particle values. [Huang et al. (1995)]. (Reproduced with kind permission of Elsevier)

In each of these uses of coating technologies, there should be no, or minimal, machining required of the coated part.

Because of the intensive R&D efforts in this field over the past few decades, the presentation of this technology has been split into two complementary chapters, with the present chapter dedicated to a discussion on the basic concepts behind the technology, including the properties of electric arcs, arc stability, and electrode erosion. This is followed by a description of the principal design features of DC plasma sources used in plasma spray operations. The important topic of gas and particle dynamics in DC plasma spraying is discussed next, with an emphasis on plasma jet dynamics, ambient gas entrainment mechanism into the plasma jet, and its effect on the flow and temperature fields in the plasma jet. The discussion on particle dynamics presented in this chapter builds on "Chapters 4 Plasma-particle momentum and heat transfer" and "Chapter 5 Gas and Particle Dynamics in Thermal Spray" covering such topics as particle trajectory and thermal history calculations and plasma-particle interactions.

The different DC plasma spray technologies are presented in the following: "Chapter 9 DC plasma Spray Processes," which includes Atmospheric Plasma Spraying (APS), Controlled Atmosphere Plasma Spraying (CAPS), Vacuum Plasma Spraying (VPS), and the relatively novel process of Ultra-Low-Pressure Plasma Spraying (ULPPS). Detailed discussions on substrate preparation, coating formation, and characterization are covered in Part III, while process integration including powder/wire or cord preparation, instrumentation, industrial applications, and process economics are covered in Part IV of this book.

Nomenclature

Units are indicated in parentheses; when no units are indicated, the parameter is dimensionless.

Latin Alphabet

A	empirical constant (6×10^5 A/m^2 K^2)
A	channel cross-sectional area (m^2)
c_p	specific heat at constant pressure (J/kg.K)
d_o	anode nozzle internal diameter (mm)
d'_a	anode boundary layer thickness (m)
d'_c	cathode boundary layer thickness (m)
d_p	particle diameter (μm)
$\overline{d_p}$	mean particle diameter (μm)
e	electric charge (Coulomb)
E	electric field strength (V/m)
E_x	electric field strength normal to the anode surface (V/m)
h	specific enthalpy (J/kg)
h_{av}	average enthalpy (J/kg)
I	arc current (A)
j_e	electrons current density (A/m^2)
j_i	ions current density (A/m^2)
k	Boltzman constant (1.38×10^{-23} J/K)
$\dot{m}_g$	mass flow rate of plasma gas (kg/s)
$\dot{m}_p$	powder mass flowrate (kg/s)
M	Mach number [$M = v/v_c$]
n_e	electron number density (m^{-3})
p	pressure (Pa)
p_e	partial pressure (Pa)
P_{el}	electric power input into the torch [$P_{\text{el}} = \text{I} \times \text{V}$] (W)
Q_{cond}	losses to the torch wall by heat conduction (W)
Q_{rad}	losses to the torch wall by radiation (W)
Q_{loss}	heat lost to the torch cooling water (W)
Q_i	Carrier gas flow rate (slm)
r	distance in the r-direction (m)
r_o	nozzle radius (mm)
Re	Reynolds number $Re = \rho v d/\mu$
$\overline{R_z}$	segment length to diameter ratio, Eq. 8.10 (−)
T_c	cathode temperature (K)

T_h heavy species temperature (K)
T_m Particle melting temperature (K)
T_e electrons temperature (K)
T_{ref} reference temperature (K)
V'_a Anode voltage fall (V)
V'_c Cathode voltage fall (V
v gas velocity (m/s)
v_c Velocity of sound (m/s)
v_p particle velocity (m/s)
v_{pi} particle injection velocity (m/s)
x distance in the x-direction (m)
y distance in the y-direction (m)
z distance in the z-direction (m)

Greek Alphabet

δ_z maximum thickness of a segment (mm)

$\Delta\overline{h}$ increase in enthalpy averaged over the cross section per unit length
Δz distance (m)
η thermal efficiency of the torch (%)
η_D deposition efficiency (%)
κ_e thermal conductivity of electron (W/m.K)
κ_h thermal conductivity of heavy particles (W/m.K)
μ dynamic viscosity
ρ mass density of the gas (kg/m^3)
ρ_p mass density of the particle or droplet (kg/m^3)
σ electrical conductivity (A/V.m)
σ_g geometric standard deviation
σ_p liquid drop surface tension (N/m)
ϕ_w work function (eV)

References

Acurex, Aero Therm. Mountain View, CA, 94043.

Ang, Andrew Siao Ming, Noppakun Sanpo, Mitchell L. Sesso, Sun Yung Kim, and C.C. Berndt. 2013. Thermal spray maps: Material genomics of processing technologies. *Journal of Thermal Spray Technology* 22 (7): 1170–1183.

Asmann, M., A. Wank, H. Kim, J. Heberlein, and E. Pfender. 2001. Characterization of the converging jet region in a triple torch plasma reactor. *Plasma Chemistry Plasma Process* 21: 37–63.

Barbezat, G., and K. Landes. 2000a. Plasma torch system triplex, increased production and a more stable process. *Sulzer-Metco Report.*

———. 2000b. Plasma technology Triplex for the deposition of ceramic coatings in the industry. In *Proc. 1st; ITSC-2000 Montreal, Canada*, ed. C.C. Berndt, 881–885. Materials Park: ASM International.

Barbezat, G. 2001. The internal plasma spraying on powerful technology for the aerospace and automotive industries. In *Proc. ITSC, Singapore, 2001*, ed. C.C. Berndt, K.A. Khor, and E.F. Lugscheider, 135–140. Materials Park: ASM International.

Baudry, C., A. Vardelle, G. Mariaux, M. Abbaoui, and A. Lefort. 2005. Numerical modeling of a D.C. non-transferred plasma torch: movement of the arc anode attachment and resulting anode erosion. *High Temperature Material Processes* 9 (1): 1–18.

Belashchenko, V. 2010. *Multi-electrode plasma system and method for thermal spraying*. US Patent 7 750 265 B2 July 6th. 2010.

Betoule, O. 1994. *Influence of velocity and temperature distributions of D.C. plasma jets and alumina particles in flight onto coating properties*. Limoges: University of Limoges.

Bisson, J.F., and C. Moreau. 2003. Effect of direct current plasma fluctuations on in-flight particle parameters: Part II. *Journal of Thermal Spray Technology* 12 (2): 258–264.

Bisson, J.F., B. Gauthier, and C. Moreau. 2003. Effect of plasma fluctuations on in-flight particle parameters. *Journal of Thermal Spray Technology* 12 (1): 38–43.

Bisson, J.F., C. Moreau, M. Dorfman, C. Dambra, and J. Mailon. 2005. Influence of hydrogen on the microstructure of plasma-sprayed Yttria-stabilized zirconia coatings. *Journal of Thermal Spray Technology* 14 (1): 85–90.

Borisov, Y. 1993. *Structure and parameters of heterogeneous plasma jets shielded by water flow*. Proc. 2nd Plasma Technik Symposium, Wohlen, Switzerland, 1–8.

Boulos, M.I. 1992. Radio-frequency plasma development, scale-up and industrial applications. *Journal of High Temperature Chemical Processes* 1: 141–148.

Boulos, M., P. Fauchais, and E. Pfender. 1994. *Thermal plasma fundamentals and applications*. Vol. 1. New York: Plenum.

Boulos, M. I., P. Fauchais, and E. Pfender (2016) Thermal Arcs, Handbook of Thermal Plasmas, (eds.) M. Boulos et al. (eds.) 1–45.

Burgess, A. 2002. Hastelloy C-276 parameter study using the axial III plasma spray system. In *Proc. ITSC-2002, Essen, Germany*, ed. E. Lugsheider, 516–518. Materials Park: ASM International.

Chen, H.C., Z. Duan, J. Heberlein, and E. Pfender. 1996. Influence of shroud gas flow and swirl magnitude on arc jet stability and coating quality in plasma spray. In *Proc. thermal spray: Particle solutions for engineering problems, Cincinnati, Ohio, 1996*, ed. C.C. Berndt, 533–561. Ohio: AMS International.

Chen, H.C., J. Heberlein, and R. Henne. 2000. Integrated fabrication process for solid oxide fuel cells in a triple torch plasma reactor. *Journal of Thermal Spray Technology* 9 (3): 348–353.

Chraska, P., and M. Hrabovsky. 1992. An overview of water stabilized plasma guns and their applications. In *Proc. ITSC-1992, Orlando, Florida*, ed. C.C. Berndt, 81–85. Materials Park: ASM International.

Chyou, Y.P., and E. Pfender. 1989a. Behavior of particulates in thermal plasma flows. *Plasma Chemistry and Plasma processing* 9 (1): 45–71.

———. 1989b. Modeling of plasma jets with superimposed vortex flow. *Plasma Chemistry and Plasma Process* 9 (2): 291–328.

Coudert, J.-F., M.-P. Planche, and P. Fauchais. 1994. Anode-arc attachment instabilities in a spray plasma torch. *Journal of High Temp. Mater. Process* 3: 639–651.

———. 1995. Characterization of D.C. plasma torch voltage fluctuations. *Plasma Chem Plasma Process* 16 (1): 211S–227S.

Coudert, J.F., M.P. Planche, and P.L. Fauchais. 1966. Characterization of DC plasma torch voltage fluctuations. *Journal Plasma Chemistry Plasma Processing* 16 (1): 211S–227S.

Coudert, J.-F., V. Rat, and D. Rigot. 2007. Influence of Helmholtz oscillations on arc voltage fluctuations in a dc plasma spraying torch. *Journal of Physics D: Applied Physics* 40: 7357–7366.

Coudert, J.-F., and V. Rat. 2008. Influence of configuration and operating conditions on the electric arc instabilities of a plasma spray torch: Role of acoustic resonance. *c* 41: 205–208.

Dinulescu, H.A., and E. Pfender. 1980. Analysis of the anode boundary layer of high intensity arcs. *Journal of Applied Physics* 51 (6): 3149–3157

Dorier, J.L., C. Hollenstein, A. Salito, M. Loch, and G. Barbezat. 2000. Influence of external parameters on arc fluctuations in a F4 DC plasma torch used for thermal spraying. In *Proceedings of the 1st ITSC-2000, Montreal, Quebec, Canada*, ed. C.C. Berndt, 37–43. Materials Park: ASM International.

Dorier, J.L., M. Gindrat, C. Hollenstein, A. Salito, M. Loch, and G. Barbezat. 2001. Time-Resolved imaging of Anodic Arc root behavior during fluctuations of a DC plasma spraying torch. *IEEE Transactions on Plasma Science* 29 (3): 494–501.

Duan, Z., S. Janisson, K. Wittmann, J.-F. Coudert, J. Heberlein, and P. Fauchais. 1999a. Effects of nozzle fluid dynamics on the dynamic characterisitcs of a plasma spray torch. In *Proc. UTSC-(1999), Düsseldorf, Germany*, ed. E. Lugscheider and P.A. Kammer, 247–252. Materials Park: ASM International.

Duan, Z., K. Wittmann, J.-F. Coudert, J. Heberlein, and P. Fauchais. 1999b. Effects of the cold gas boundary layer on arc fluctuations. In *Proc. ISPC-14, Prague, Czech Republic*, ed. M. Hrabovsk'y, M. Konrád, and V. Kopeck'y, 233–238. Prague: Institute of Plasma Physics, CAS.

Duan, Z., L. Beall, M.P. Planche, J. Heberlein, E. Pfender, and M. Stachowicz. 1997. Arc voltage fluctuations as an indication of spray torch anode condition. In *Proceedings of thermal spray: A united forum for scientific and technological advances*, ed. C.C. Berndt, 407. Material Park, ASM International.

Duan, Z., and J. Heberlein. 2000. Anode boundary layer effects in plasma spray torches. In *Proc. 1st ITSC-2000, Montreal, Quebec*, ed. C.C. Berndt, 1–7. Materials Park: ASM International.

Duan, Z., L. Beall, J. Schein, J. Heberlein, and M. Stachowicz. 2000. Diagnostics and modeling of an Argon/Helium plasma spray process. *Journal of Thermal Spray Technology* 9 (2): 225–234.

Duan, Z., and J. Heberlein. 2002. Arc instabilities in a plasma spray torch. *Journal of Thermal Spray Technology* 11 (1): 44–51 ex 32.

Dussoubs, B. 1998 *3D modeling of the plasma spray process*. PhD thesis, University of Limoges, Limoges, France (in French).

Dussoubs, B., A. Vardelle, G. Mariaux, P. Fauchais, and N.J. Themelis. 1999. Modeling of simultaneous plasma spraying of two powders. In *Proceedings united thermal spray society, Düsseldorf, Germany, 1999*, ed. E. Lugsheider and P.A. Kammer, 793–798. Materials Park: ASM International.

Dussoubs, B., A. Vardelle, G. Mariaux, N.J. Themelis, and P. Fauchais. 2001. Modeling of plasma spraying of two powders. *Journal of Thermal Spray Technology* 10 (1): 105–110.

Fauchais, P., and A. Vardelle. 1997. Thermal plasmas. *IEEE Trans. on Plasma Science* 25 (6): 1258–1280.

Fauchais, P. 2004. Understanding plasma spraying. *Journal of Physics D: Applied Physics* 37: 86–108.

Fauchais, P., J. Heberlein, M. Boulos. 2014. Thermal spray fundamentals from powder to part, Chapter 5 Combustion spraying systems.

Fincke, J., and W.D. Swank. 1991. The effect of Plasma jet fluctuations on particle time-temperature histories. *In Proceedings of 4th NTSC, Pittsburgh, Pennsylvania, 1991*, ed. T.F. Bernecki, 193–198. Materials Park: ASM International

Fincke, J.R., D.M. Crawford, S.C. Snyder, W.D. Swank, D.C. Haggard, and R.L. Williamson. 2003. Entrainment in high-velocity, high temperature plasma jets, Part I: Experimental results. *International Journal of Heat Mass Transfer* 46: 4201–4213.

Fukanuma, H. 1988. Japanese Patent 230300 JP. 04/24/1988,

Fukumoto, M., I. Ohgitani, H. Nagai, and T. Yasni. 2005. Effect of substrate surface change by heating on flattening behavior of thermal sprayed particles. In *ITSC-2005*, ed. E. Lugscheider. Düsseldorf: DVS. e-proceedings.

Fukumoto, M., H. Nagui, and T. Yasui. 2006. Influence of surface character change of substrate due to heating on flattening behavior of thermal sprayed particles. In *ITSC-2006*, ed. B. Marple et al. Materials Park: ASM International.

Fukumoto, M., T. Yamaguchi, M. Yamada, and T. Yasui. 2007. Splash splat to disk splat transition behavior in plasma-sprayed metallic materials. *Journal of Thermal Spray Technology* 16 (5–6): 905–912.

Fukumoto, M., K. Yang, K. Tanaka, T. Usami, T. Yasui, and M. Yamada. 2011. Effect of substrate temperature and ambient pressure on heat transfer at interface between molten droplet and substrate surface. *Journal of Thermal Spray Technology* 20 (1–2): 48–58.

Gerdien, H., and A. Lotz. 1922. Wiss. Veröff. Siemens-Konz. 489–4.

Gregori, G., U. Kortshagen, E. Pfender, and J. Heberlein. 2003. Time-resolved temperature measurements in a turbulent argon plasma jet. In *Proc. 16th Intern. Symp. Plasma Chemistry, Taormina, Italy, 2003*, ed. R. d'Agostino, P. Favia, F. Fracassi, and F. Palumbo. University of Bari. unpaginated CD.

Guest, C.J.S., and K.G. Ford. 1975. US Patent 3892882,

Huang, P.C., J. Heberlein, and E. Pfender. 1995. Particle behavior in a two-fluid turbulent plasma jet. *Surface and Coatings Technology* 73 (3): 142–151.

Hardwicke, C.U., and Y.-C. Lau. 2013. Advances in thermal spray coatings for gas turbines and energy generation: A review. *Journal of Thermal Spray Technology* 22 (5): 564–576.

Harry, J.E., and L. Hobson. 1979. Production of a large discharge using a multiple arc system. *IEEE Transactions on Plasma Science* 7: 157–162.

Harry, J.E., and R. Knight. 1981. Simultaneous operation of electric arcs from the same supply. *IEEE Transactions on Plasma Science* 9: 248–254.

Haure T., *Multifunctional layers obtained by a multi-technique process*. Ph.D University of Limoges, France, Nov. 2003 (In French).

Henne, R., E. Bouyer, V. Borck, and G. Schiller. 2001. Influence of anode nozzle and external torch contour on teh quality of the atmospheric DC plasma spray process. In *Proceedings of the ITSC-2001, Singapore*, ed. C.C. Berndt, K.A. Khor, and E. Lugsheider, 471–478. Materials Park: ASM International.

Hrabovsky, M. 1992. Plasma generator with water stabilized DC arc. In *Proc. industrial applications of plasma physics, Varenna, Italy, 1992*, ed. W. Hooke and E. Sindoni, 557–562. Italian Physical Society.

Hrabovsky, M., V. Kopecky, and V. Sember. 1995. Water stabilized arc as a source of thermal plasma. In *Proc. Intern. Symp. Heat and Mass Transfer under Plasma Conditions, Cesme, Turkey, 1995*, ed. P. Fauchais, 91–98. New York: Begell House, Inc.

Hrabovsky, M., M. Konrad, V. Kopecky, and V. Sember. 1997. Processes and properties of electric arc stabilized by water vortex. *IEEE Transactions on Plasma Science* 25: 833–839.

Jenista, J. 2017. Steam torch plasma modelling. *Plasma Chemistry Plasma Process* 37: 653–687.

Jenista, J., J. Heberlein, and E. Pfender. 1997a. Model for anode heat transfer from an electric arc. In *Proc. fourth international thermal plasma processes conference, Athens, Greece*, ed. P. Fauchais, 805–815. New York: Begell House, Inc.

———. 1997b. Numerical model of the anode region of high-current electric arcs. *IEEE Transactions on Plasma Science* 25 (5): 883–890.

Leblanc, L., and C. Moreau. 2002. The long-term stability of plasma spraying. *Journal of Thermal Spray Technolgoy* 11 (3): 380–386.

Leveroni, E., A.M. Rahal, and E. Pfender. 1987. Electron temperature measurements in the near-wall region of wall-stabilized arcs. In *Proc. ISPC-8, Tokyo, Japan, 1987*, ed. K. Akashi and A. Kinbara, 346–351. Tokyo: University of Tokyo.

Li, H.P., and E. Pfender. 2005. Three-dimensional effects inside a dc arc plasma torch. *IEEE Transactions on Plasma Science* 33 (2): 400–401.

Liu, S.-H., C.-X. Li, L. Li, J.-H. Huang, P. Xu, Y.-Z. Hu, G.-J. Yang, and C.-J. Li. 2018. Development of long laminar plasma jet on thermal spraying process: Microstructures of zirconia coatings. *Surface & Coatings Technology* 337: 241–249.

Liu, S.-H., S.-L. Zhang, C.-X. Li, L. Li, J.-H. Huang, J.P. Trelles, A.B. Murphy, and C.-J. Li. 2019. Generation of long laminar plasma jets: Experimental and numerical analyses. *Plasma Chemistry and Plasma Processing* 39: 377–394.

Lu, Z.P., and E. Pfender. 1989. Synthesis of AIN powder in a triple torch plasma reactor. In *Proc. ISPC-9, Pugnochiuso, Italy*, ed. R. d'Agostino, 675–680. Bari: University of Bari.

Malmberg, S., K. Leung, J. Heberlein, and E. Pfender. 1995. Particle Trajectory Control for DC Plasma Spraying. In *ITSC-1995 - Current*

status and future trends, Kobe, Japan, ed. A. Ohmori, 371–375. High Temperature Society of Japan.

Huang, P.C., J. Heberlein, and E. Pfender. 1995. Particle behavior in a two-fluid turbulent plasma jet. *Surface and Coatings Technology* 73 (3): 142–151.

Marantz, D.R., and H. Herman. 1991. Plasma generating apparatus and method, US Patent 4982067.

———. 1992. Plasma spray gun and method of use, US Patent 5144110.

Mariaux, G., P. Fauchais, A. Vardelle, and B. Pateyron. 2001. Modeling of the plasma spray process: From powder injection to coating formation. *Jouurnal of High Temperature Materials and Processes* 5: 61–85.

Mariaux, G., and A. Vardelle. 2005. 3-D time-dependent modelling of the plasma spray process. Part 1: flow modelling. *International Journal of Thermal Sciences* 44: 357–366.

Marqués, J.-L., G. Forster, and J. Schein. 2009. Multi-electrode plasma torches: Motivation for development and current state-of-the-art. *The Open Plasma Physics Journal* 2: 89–98.

Mauer, G., R. Vaßen, D. Stöver, S. Kirner, J.L. Marque´s, S. Zimmermann, G. Forster, and J. Schein. 2011a. Improving power injection in plasma spraying by optical diagnostics of the plasma and particle characterization. *Journal of Spray Technology* 20 (1–2): 3–11.

Mauer, G., R. Vaßen, and D. Stöver. 2011b. Plasma and particle temperature measurements. *Journal of Thermal Spray Technology* 20 (3): 391–406.

Mohanty, M., R.W. Smith, R. Knight, W.L.T. Chen, and J. Heberlein. 1996. Shrouded air plasma processing of lightweight coatings. In *Proceedings of 9th NTSC, Cincinnati, OH, 1996*, ed. C.C. Berndt. Materials Park: ASM International.

Molz, R., R. McCullough, D. Hawley, and F. Muggli. 2007. Improvement of plasma gun performance using comprehensive fluid element modeling II. *Journal of Thermal Spray Technology* 16 (5−6): 684–689.

Moreau, C., P. Gougeon, A. Burgess, and D. Ross. 1995. Characterization of particle flows in an axial injection plasma torch. In *Proc. NTSC-1995, Houston, Texas*, ed. C.C. Berndt and S. Sampath, 141–147. Materials Park: ASM International.

Moreau, E., C. Chazelas, G. Mariaux, and A. Vardelle. 2006. Modeling the restrike mode operation of a DC plasma spray torch. *Journal of Thermal Spray Technology* 15 (4): 524–530.

Muehlberger, E., S.E. Muehlberger, and A. Sickinger. *Modular segmented cathode plasma generator*. US Patent 5298835, 1994.

Muggli, F., R. Molz, R. McCullough, and D. Hawley. 2007. Improvement of plasma gun performance using comprehensive fluid element modeling: Part I. *Journal of Thermal Spray Technology* 16 (5−6): 677–683.

Murphy, A.B. 1996. The influence of demixing on the properties of a free-burning arc. *Applied Physics Letters* 69: 328–330.

Outcalt, D., M. Hallberg, G. Yang, J. Heberlein, P. Strykowski, and E. Pfender. 2007. Diagnostics and control of instabilities in a plasma spray torch. In *Proc. ITSC-18, Kyoto, Japan, 2007*, ed. K. Tachibana. Kyoto University. p unpaginated CD.

Paik, S., P.C. Huang, J. Heberlein, and E. Pfender. 1993. Determination of the arc-root position in a DC plasma torch. *Plasma Chemistry and Plasma Processing* 13 (3): 379–397.

Pan, W., W. Zhang, W. Zhang, and C. Wu. 2001. Generation of long, laminar plasma jets at atmospheric pressure and effects of flow turbulence. *Plasma Chemistry and Plasma Processing* 21 (1): 23–35.

Park, J.H., Z. Duan, J. Heberlein, E. Pfender, Y.C. Lau, and H.P. Wang. 1997. Modeling of fluctuations experienced in N2 and N2H2 plasma jets issuing into atmospheric air. In *Proceedings of 13th international symposium on plasma chemistry, Beijing, P.R. China, 1997*, ed. C.K. Wu, 326–331. International Union of Pure and Applied Chemistry.

Park, J.H., J. Heberlein, E. Pfender, Y.C. Lan, J. Rund, and H.P. Wang. 1999. Particle behavior in a fluctuating plasma jet. In *Proceedings of 2nd international symposium on heat and mass transfer under plasma conditions, Antalya, Turkey, 1999*, ed. P. Fauchais, J. Van der Mullen, and J. Heberlein, 417–424. New York: Academy of Sciences.

Peters, J., F. Yin, C. Borges, J. Heberlein, and C. Hackett. 2005. Erosion mechanisms of hafnium cathodes at high current. *Journal of Physics D: Applied Physics* 38: 1781–1794.

Pfender, E., and Y.C. Lee. 1985. Particle dynamics and particle heat and mass transfer in thermal plasmas. Part I. The motion of a single particle without thermal effects. *Journal of Plasma Chemistry Plasma Processing* 5 (3): 211–237.

Pfender, E. 1989. Multiple arc plasma device with continuous gas jet. US patent 4818837, 1989.

Pfender, E. 1978. Electric arcs and arc gas heaters. In *Gaseous electronics: Electrical discharges*, ed. M.N. Hirsh and H.J. Oskam, vol. 1, 291–398. Academic Press, Inc.

———. 1998. *Multiple arc plasma device with continuous gas jet*. US patent 4818837.

Pfender, E., W.L.T. Chen, and R. Spores. 1990. A new look at the thermal and gas dynamic characteristics of a plasma jet. In *Proc. NTSC-1990, Long Beach, California*, ed. C.C. Berndt, 1–10. Materials Park: ASM International.

Pfender, E., J. Fincke, and R. Spores. 1991. Entrainment of cold gas into thermal plasma jets. *Plasma Chemistry and Plasma Processing* 11 (4): 529–543.

Pfender, E. 1994. Thermal plasma-wall boundary layers. In *Proc. international symposium on heat and mass transfer under plasma conditions, Cesme, Turkey*, ed. P. Fauchais, 223–235. New York: Begell House.

———. 1999. Thermal plasma technology: Where Do we stand and where are we going? *Plasma Chemistry and Plasma Processing* 19 (1): 1–31.

Planche, M.-P., J.-F. Coudert, and P. Fauchais. 1995. Evolution of the plasma flow characteristics, during the first hours, after replacing the set of electrodes. In *ISPC-12, Minneapolis, MN*, ed. J.V. Heberlein, D.W. Ernie, and J.T. Roberts, 1475–1480. Minneapolis: University of Minnesota.

Planche, M.-P., Z. Duan, O. Lagnox, J. Heberlein, J.-F. Coudert, and E. Pfender. 1997. Study of arc fluctuations with different plasma spray torch configurations. In *ISPC-13, Beijing, P.R. China*, ed. C.K. Wu, 1460–1465. International Union of Pure and Applied Chemistry.

Planche, M.P., J.F. Coudert, and P. Fauchais. 1998. Velocity measurements for arc jets produced by a DC plasma spray torch. *Plasma Chemistry and Plasma Processing* 18 (2): 263–283.

Prystay, M., P. Gougeon, and C. Moreau. 1996. Correlation between particle temperature and velocity and the structure of plasma sprayed zirconia coatings. In *Proc. NTSC-1996, Cincinnati, Ohio*, ed. C.C. Berndt, 511–516. Materials Park: ASM International.

Rahmane, M., G. Soucy, M. Boulos, and R. Henne. 1998. Fluid dynamic study of direct current plasma jets for plasma spraying applications. *Journal of Thermal Spray Technology* 7 (3): 349–356.

Ramesh, C.S., D.S. Devaraja, R. Keshavamurthya, and B.R. Sridharb. 2011. Slurry erosive wear behavior of thermally sprayed Inconel-718 coatings by APS process. *Wear* 271 (9–10): 1365–1371.

Rat, V., and J.-F. Coudert. 2011. Improvement of plasma spray torch stability by controlling pressure and voltage dynamic coupling. *Journal of Thermal Spray Technology* 20 (1-2): 28–38

Rat, V., F. Mavier, and J.F. Coudert. 2017. Electric arc fluctuations in DC plasma spray torch. *Plasma Chemistry Plasma Process* 37: 549–580.

Rigot, D., G. Delluc, B. Pateyron, J. Coudert, P. Fauchais, and J. Wigren. 2003. Transient evolution and shift of signals emitted by a DC plasma gun (type PTF4). *Journal of High Temperature Material Processes* 7: 175–186.

Roumilhac, P., J.-F. Coudert, and P. Fauchais. 1990b. Influence of the arc chamber design and the surrounding atmosphere on the characteristics and temperature distribution of Ar-H2 and Ar-He spraying plasma jets. In *Plasma processing and synthesis of materials*, ed. D. Apelian and J. Szekely, vol. 190, 227–333. Pittsburgh: MRS.

Roumilhac, P., J.-F. Coudert, and P. Fauchais. 1990a. Designing parameters of spraying plasma torches. In *Proc. NTSC-1990., Long Beach, CA*, ed. T. Bernecki, 11–19. Materials Park: ASM International.

———. 1990b. Influence of the arc chamber design and the surrounding atmosphere on the characteristics and temperature distribution of Ar-H_2 and Ar-He spraying plasma jets. In *Plasma processing and synthesis of materials*, ed. D. Apelian and J. Szekely, vol. 190, 227–333. Pittsburgh: MRS.

Roumilhac, P. 1990. *Contribution to the metrology and understanding of the DC plasma spray torches and transferred arcs for reclamation at atmospheric pressure*. PhD thesis, University of Limoges, Limoges, France (in French).

Santen, S., L. Bentell, B. Johansson, and P. Westerland. 1986. Chapter 9: Applications of plasma technology in ironmaking. In *Plasma technology in metallurgical processing*, ed. J. Feinmann. Warrendale: AIME Iron and Steel Soc.

Schmidt, T., H. Assadi, F. Gärtner, H. Richter, H. Kreye, and T. Klassen. 2009. From particle acceleration to impact and bonding in cold spraying. *Journal of Thermal Spray Technology* 18 (5–6): 794–808.

Schwenk, A., H. Gruner, X. Zimmermann, K. Landes, and G. Nutsch. 2004. Improved Nozzle Design of de-Laval-type Nozzles of the Atmospheric Plamsa Spraying. In *Proc. Proceedings of the International Thermal Spray Conference, Osaka, Japan, 2004*, ed. A. Ohmori, 600–605. Materials Park: ASM International.

Snyder, S.C., A.B. Murphy, D.L. Hofeldt, and L.D. Reynolds. 1995. Diffusion of atomic hydrogen in an atmospheric pressure free-burning arc discharge. *Physical Review E* 52: 2999–3009.

Spores, R., and E. Pfender. 1989. Flow structure of a turbulent thermal plasma jet. *Surface and Coatings Technology* 37 (3): 251–270.

Spores, R., E. Pfender, and J. Heberlein. 1990. Fluid-dynamic characteristics of a plasma spray jet. In *Proc. plasma jets in the development of new material technology, Frunze, USSR*, ed. O.P. Solonenko and A.I. Fedorchenko, 699–716. Utrecht: V.S.P.

Sun, X., and J. Heberlein. 2005. Fluid dynamic effects on plasma torch anode erosion. *Journal of Thermal Spray Technology* 14 (1): 39–44.

Thörnblom, J. 1989. Industrial plasma applications. In *Proc. ISPC-9, workshop on industrial applications*, 25. University of Bari, Department of Di Chemica, Italy.

Trelles, J.P., E. Pfender, and J.V.R. Heberlein. 2006. Multiscale finite element modeling of arc dynamics in a DC plasma torch. *Journal of Plasma Chemistry Plasma Processing* 26: 557–575.

Trelles, J.P., and J.V.R. Heberlein. 2006b. Simulation results of arc behavior in different plasma spray torches. *Journal of Thermal Spray Technology* 15 (4): 563–569.

Trelles, J.P., and J. Heberlein. 2006c. Simulation results of arc behavior in different plasma spray torches. *Journal of Thermal Spray Technology* 15 (4): 563–569.

Trelles, J.P. 2007. *Finite element modeling of flow instabilities in arc plasma torches*. Ph.D. Thesis, University of Minnesota, Minneapolis.

Trelles, J.P., E. Pfender, and J.V.R. Heberlein. 2007a. Modelling of the arc reattachment process in plasma torches. *Journal of Physics D: Applied Physics* 40: 5635–5648.

Trelles, J.P., J. Heberlein, and E. Pfender. 2007b. Non-equilibrium modeling of arc plasma torches. *Journal of Physics D: Applied Physics* 40: 5937–5952.

Trelles, J.P., J. Heberlein, and E. Pfender. 2008. The reattachment process in nonequilibrium arc simulation. *IEEE Transactions on Plasma Science* 36 (4): 1024–1025.

Trelles, J.P., E. Pfender, and J. Heberlein. 2007c. Thermal nonequilibrium simulation of an arc plasma jet. *IEEE Transactions on Plasma Science* 36 (4): 1026–1027.

Trelles, J.P., C. Chazelas, A. Vardelle, and J.V.R. Heberlein. 2009. Arc plasma torch modeling. *Journal of Thermal Spray Technology* 18 (5−6): 728–751.

Trelles, J.P. 2011. Nonequilibrium thermal plasma jet impinging on a substrate. *IEEE Transactions on Plasma Science* 39 (11): 2870–2871.

———. 2013. Computational study of flow dynamics from a dc arc plasma jet. *Journal of Physics D: Applied Physics* 46: 255201. (17pp).

Tucker, R.C., Jr., ed. 2013. *Thermal spray technology Vol. 5A, ASM handbook*. Materials Park: ASM International.

Van den Brook, J., M. Labrot, and D. Pineau. 1987. *Revue Générale de Thermique* 310: 527–541. (in French).

Vardelle, A., M. Vardelle, and P. Fauchais. 1982. Influence of velocity and surface temperature of alumina particles on the properties of plasma sprayed coatings. *Journal of Plasma Chemistry Plasma Processing* 2 (3): 255–291.

Vardelle, M., A. Vardelle, P. Fauchais, and M.I. Boulos. 1983. Plasma-particle momentum and heat transfer: Modelling and measurements. *AIChE Journal* 29 (2): 236–243.

———. 1988. Particle dynamics and heat transfer under plasma conditions. *AIChE Journal* 34 (4): 568–573.

Vardelle, M., A. Vardelle, P. Fauchais, K.-I. Li, B. Dussoubs, and N.J. Themelis. 2001. Controlling particle injection in plasma spraying. *Journal of Thermal Spray Technology* 10 (2): 267–284.

Vardelle A., C. Moreau, J. Akedo, H. Ashrafizadeh, C. C. Berndt, J. Oberste Berghaus, M. Boulos, J. Brogan, A. C. Bourtsalas, A. Dolatabadi, M.l Dorfman, T. J. Eden, P. Fauchais, G. Fisher, F. Gaertner, M. Gindrat, R. Henne, M. Hyland, E. Irissou, E. H. Jordan, K. A. Khor, A. Killinger, Y.-C. Lau, C.-J. Li, Li Li, J. Longtin, N. Markocsan, P. J. Masset, J. Matejicek, G. Mauer, A. McDonald, J. Mostaghimi, S. Sampath, G. Schiller, K. Shinoda, M. F. Smith, A. A. Syed, N. J. Themelis, F.-L. Toma, J. P. Trelles, R. Vassen, and P. Vuoristo. 2016. The 2016 thermal spray roadmap. *Journal of Thermal Spray Technology* 25(8): 1376–1440.

Watson V.R., and E.B. Pegot. 1967. *Numerical calculation for the characteristics of a gas flowing axially through a constricted arc*, NASA, TD, D-4042.

Wigren, J., and K. Täng. 2007. Quality considerations for the evaluation of thermal spray coatings. *Journal of Thermal Spray Technology* 16 (4): 533–540.

Williamson, R.L., J.R. Finke, D.M. Crawford, S.C. Snyder, W.D. Swank, and D.C. Haggard. 2003. Entrainment in high-velocity, high temperature plasma jets, Part II: computational results and comparison to experiment. *International Journal Heat and Mass Transfer* 46: 4215–4228.

Wutzke, S.A., E. Pfender, and E.R.G. Eckert. 1968. Symptomatic behavior of an electric arc with a superimposed flow. *AIAA Journal* 6 (8): 1474–1482.

Yang, G., and J. Heberlein. 2007. The anode region of high intensity arcs with cold cross flows. *Journal of Physics D: Applied Physics* 40: 5649–5662.

Yang, E.-J., G.-J. Yang, X.-T. Luo, C.-J. Li, and M. Takahashi. 2012. Epitaxial grain growth during splat cooling of alumina droplets produced by atmospheric plasma spraying. In *ITSC-2012*. Materials Park: ASM International. e-proc.

Young, R.M., and E. Pfender. 1989. A novel approach for introducing particulate matter into thermal plasmas: The triple-cathode arc. *Plasma Chemistry and Plasma Processing* 9 (4): 465–481.

Zhukov M.F. 1989. *Electric arc generators of low temperature plasma*. High Temperature Dust Laden Jets. VPS, NL.

Zhukov, M.F. 1989a. *Electric arc generators of low temperature plasma. High temperature dust laden jets*. Utrecht: VPS.

———. 1998. Linear direct current plasma torches. In *Proc. thermal plasma and new materials technology*, ed. O.P. Solonenko and M.F. Zhukov, 9–21. Cambridge, UK: Cambridge Interscience.

Zhukov, M.F. 1994. Linear direct current plasma torches. In *Proceedings of thermal plasma and new materials technology*, ed. O.P. Solonenko and M.F. Zhukov, 9–21. Cambridge: Cambridge Interscience.

Zierhut, J., P. Haslbeck, K.D. Landes, B. G, M. Muller, and M. Schutz. 1998. TRIPLEX - an innovative three-cathode plasma torch. In *Proceeding of the international thermal thermal spray conference, Nice, France, 1998*, ed. C. Coddet, 1374–1380. Materials Park: ASM International.

Zhukov, M.F., ed. 1977. *Electric arc plasmatrons*. The USSR Academy of Science, Siberian Chapter, Institute of Thermal Physics, Novosibirsk/USSR.

———. 1989b. *Electric arc generators of low temperature plasma. High temperature dust laden jets*. Utrecht: VPS.

Zhou, X., and J. Heberlein. 1998. An experimental investigation of factors affecting arc-cathode erosion. *Journal of Physics D: Applied Physics* 31 (19): 2577–2590.

Zhukov, M.F. 1994. Linear direct current plasma torches. In *Proc. thermal plasma and new materials technology*, ed. O.P. Solonenko and M.F. Zhukov, 9–21. Cambridge, UK: Cambridge Interscience.

Zhukov, M.F., and I.M. Zasypkin, 2007. *Thermal plasma torches: Design, characteristics, applications*, 596 pages. Cambridge Int Science.